THESIS FOR THE DEGREE OF LICENTIATE OF ENGINEERING

Poly(*N*-Isopropylacrylamide) Polymer Brush Functionalized Nanostructures as Thermo-Responsive Gating Systems for Protein Transportation

JUSTAS SVIRELIS

Department of Chemistry and Chemical Engineering
CHALMERS UNIVERSITY OF TECHNOLOGY
Gothenburg, Sweden 2021

Poly(*N*-Isopropylacrylamide) Polymer Brush Functionalized Nanostructures as Thermo-Responsive Gating Systems for Protein Transportation

Justas Svirelis

© Justas Svirelis, 2021.

Licentiatuppsatser vid Institutionen för kemi och kemiteknik

Chalmers tekniska högskola

Nr 2021:01

Department of Chemistry and Chemical Engineering
Chalmers University of Technology
SE-412 96 Gothenburg
Telephone +46 31 772 1000

Printed by Chalmers Reproservice
Gothenburg, Sweden 2021

Poly(*N*-Isopropylacrylamide) Polymer Brush Functionalized Nanostructures as Thermo-Responsive Gating Systems for Protein Transportation
JUSTAS SVIRELIS
Chemistry and Chemical Engineering
Chalmers University of Technology

Abstract

Controlling molecule translocation through nanosized gaps is of great interest in novel systems for single molecule analysis and biomolecular membranes. The molecular gating property of thermo-responsive end-grafted poly(*N*-isopropylacrylamide) (PNIPAM) polymer brushes on well-shaped gold-silica nanostructures is intended to be investigated for controlled protein transportation via extinction spectroscopy and fluorescence microscopy methods below and above PNIPAM lower critical solution temperature (LCST; 32 °C in water). Polymer brushes are prepared via Activators Regenerated by Electron Transfer Atom Transfer Radical Polymerization (ARGET-ATRP) by employing Bis[2-(2-bromoisobutyryloxy)undecyl] disulfide (DTBU) and its thiol (TBU) equivalent as initiators for the reaction. Variation of PNIPAM reaction time/solvent constituency during the polymerization, results in different swollen/collapsed polymer brush thicknesses, indicated by the plasmonic shifts in extinction spectroscopy and surface plasmon resonance experiments. By having sufficient polymer thickness and grafting density for, e.g. 80-90 nm, nanowells, polymer conformational change below and above LCST, allows controlled gating of these nanostructures. This feature was employed for protein transportation through the polymer brush interface in and out of the fabricated nanowell according to its plasmonic activity. In addition, we investigated molecular gating of fluorescently labelled protein transportation by complimentary fluorescence microscopy measurements.

Keywords: Poly(*N*-Isopropylacrylamide), polymer brushes, surface plasmon resonance, fluorescence microscopy, biomolecule transportation, thermo-responsive polymers

Contents

List of Figures

List of Tables

Introduction 1

Single molecule entrapment and subsequent analysis of their structure, function and binding events is of high interest not only by the fundamental research scientists, but also by biomedical and pharmaceutical industries. This is due to the fact, that biomolecules, such as proteins, may exist in various conformations in same [1, 2] and different environments [3], thus their individual structure and function are not possible to distinguish from the group of the same kind of molecules [3–6]. By not being able to do this, we limit our understanding of fundamental blocks (proteins) of biological events, e.g. enzyme activity [5], messaging (protein-protein interaction) [7], protein oligomerization [8, 9] and other processes. This can be seen as follow-up studies upon single cell research, which has enabled understanding of the heterogeneities between cells [10]. In addition, currently existing systems, which allow to study individual molecules lack means to avoid unwanted forces acting on the molecules in their local environment during the analysis and include immobilization of molecules on the surface.

One of the main reasons why scientists struggle to study single biomolecules is due to the fact that they should be in conditions, that would replicate their native environment as much as possible (e.g. physiological conditions). Also, it is difficult to entrap biomolecules in such a manner, that they would not diffuse away when the experiment is performed [6]. In addition, most of the known trapping tools mainly work for bigger objects (e.g. biological cells) [11], exclude the needed aqueous environment, pH and salt concentration for proteins [12]. Even though it would be possible to covalently link a protein in question on a surface, this would restrict their degree of freedom and conformational states, which could impale their function [5]. Nevertheless, nanoscale capsules, known as liposomes, which could be used in physiological conditions, have been previously reported [13] as a possible solution to the mentioned problems. However, the number of encapsulated biomolecules compared to the liposome total volume is small in practice, the surrounding liquid around the proteins inside the liposomes is difficult to exchange and small molecule loading inside these vesicles is still challenging, therefore reducing the wide applicability of such systems for biomolecule study.

To begin with, in order to tackle some of the previously mentioned limitations, we suggest trapping proteins in nanoscale chambers [14], e.g. ***nanowells*** (Figure 1.1 (a, b, c top layer and d, left)) or

nanocaves (Figure 1.1 (c bottom layer and d, right)), in a non-invasive manner and without immobilizing them.

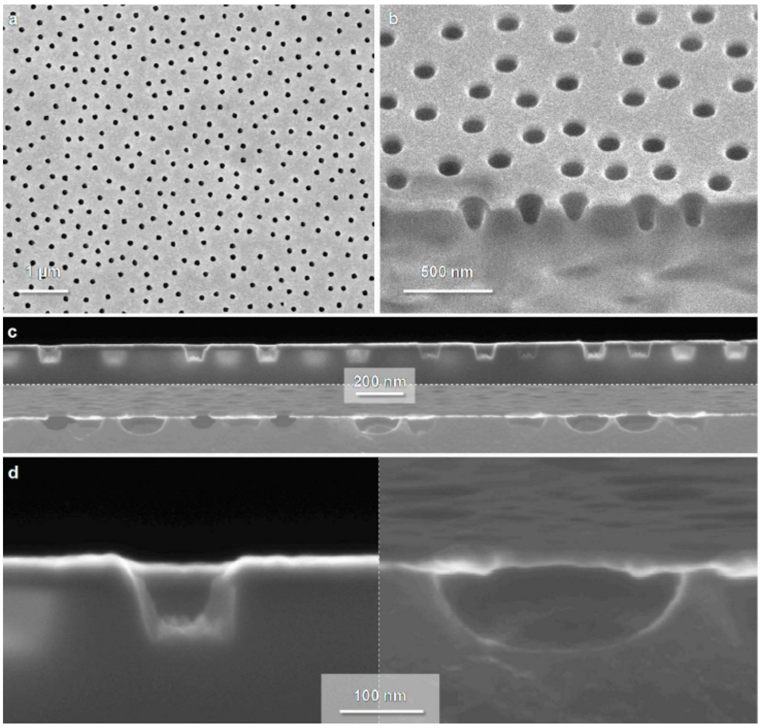

Figure 1.1: Scanning electron microscope images with cross-sections of the nanoscale chambers, nanowells ((a), (b), (c, top), (d, left)) and nanocaves ((c, bottom), (d, right); cut with focused ion beam (FIB)). [14]

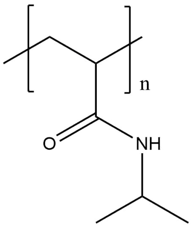

Figure 1.2: Temperature responsive PNIPAM polymer used as an entropic barrier after being grafted on nanochambers.

These nanocontainers are functionalized with thermo-responsive polymer brushes of poly(*N*-Isopropylacrylamide) (PNIPAM; fig. 1.2) via Activators Regenerated by Electron Transfer Surface Initiated Atom Transfer Radical Polymerization (ARGET-SI-ATRP), acting as a gate for biomolecule translocation due to conformational change induced by controlled temperature variation (fig. 1.3). When the polymer is in the swollen state, it acts as an impenetrable entropic barrier (such as poly(ethylene glycol)(PEG) polymer brushes [15]) and when the temperature reaches PNIPAM's lower critical solution temperature (LCST; ≈32 °C in aqueous solutions [16]), the polymer brushes collapse into compact globule states, thus opening the nanochamber and letting biomolecules translocate. By doing this, it could be possible to mimic the biomolecule native environment by keeping them trapped in fixed volume containers for further analysis similarly to a technique proposed previously [17].

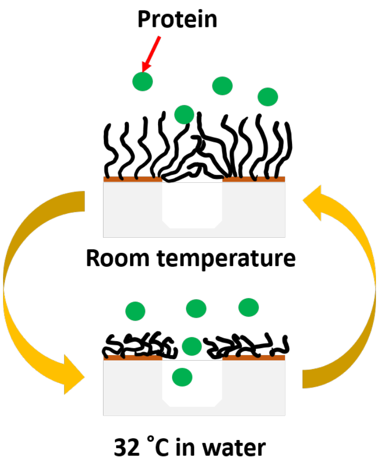

Figure 1.3: PNIPAM polymer brush functionalized nanostructure gating mechanism for proteins.

The goal of this thesis is mainly focused on optimizing the polymerization conditions to achieve the needed PNIPAM polymer brush thickness in order to control the translocation of bovine serum albumin (BSA) through the polymer brush functionalized nanopores and trapping them in a non-invasive way. The translocation and trapping are monitored with extinction spectroscopy and fluorescence microscopy. In addition, complimentary experiments in order to detect possible protein-polymer interactions, which could impede the gating through the nanopores, with Surface Plasmon Resonance (SPR) and Quartz Crystal Microbalance with Dissipation Monitoring (QCM-D) will be discussed. Due to to the fact, that the molecular weight and, thus, grafting density of the polymer brush layer cannot be characterized straightforwardly [18], we only determined the dry, swollen and collapsed brush heights (non-interactive probe method [19]). This was needed in order to optimize polymer brush height upon varying solvent composition and time during the polymerization and achieve switchable barriers for protein gating through 80-90 nm diameter nanoscale pores.

Theory

2

2.1 Surface plasmon resonance (SPR)

The excitation of surface plasma waves was first described over a century ago by Wood [20]. Consequently, Kretschmann [21] and Otto [22] showed that the surface plasmons (SPs) can be optically excited by attenuated total reflection in late sixties. After that, SPs gained great importance and have been extensively researched [23, 24]. Nowadays, the significant variety of applications of the surface plasmon effect has risen over the decades and only keeps on growing. Consequently, the surface plasmon resonance effect was employed to study changes of the bulk and local surface refractive indexes.

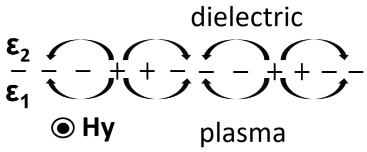

Figure 2.1: The charges of the surface plasmons, which propagate on a surface, in the direction of k_x vector. H_y depicts the direction of the magnetic field (p-polarized wave) on the y axis.

To begin with, fundamental properties of SPs will be overviewed. An important feature of dielectric/metal interfaces, called surface plasma oscillations, appear when the electron charges, localized on a metal boundary, carry out coherent motion (fig. 2.1). These waves were first described by Ritchie [25] and proven experimentally by Powell and Swan [26]. A dispersion relation $\omega(k_x)$ describes these longitudinal oscillations, where it takes into account their frequency ω and the wave vector k_x. In addition, charge fluctuations together with transversal and longitudinal electromagnetic field are localized in the z direction up to around 1 angstrom (Thomas-Fermi screening length) on the metal boundary. As it has been known for surface waves, the electromagnetic field (depicted by equation 2.1) is at its peak when z is zero and disappears when $|z|$ is approaching infinity (see fig. 2.2). This phenomenon clarifies why the charge fluctuations together with the electromagnetic field E (consists of two components - transversal and longitudinal) are especially sensitive to changes happening on the surface. [24]

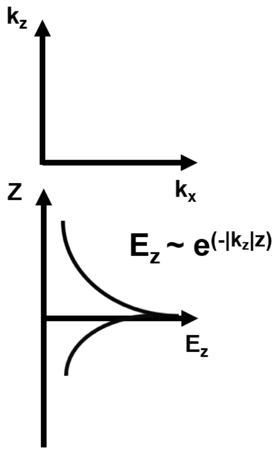

Figure 2.2: Eletrical field exponential decay of SPs in the direction of z.

$$E = E_0^{\pm} \exp[+i(k_x x \pm k_z z - \omega t)] \tag{2.1}$$

In eq. 2.1, "+" and "-" signs are when $z \geq 0$ and $z \leq 0$, accordingly, and the transversal and longitudinal electromagnetic field vector k_z describes the exponential decay of the field E_z. The wave vector k_x coincides with the direction of the x axis and is equal to $2\pi/\lambda_p$, where λ_p is the wavelength of the plasmon oscillations. It can also be expressed with respect to a certain medium of choice through the refractive index, e.g. $k = \omega n/c$. In addition, k has to have imaginary and real parts, where $k = Re(k) + iIm(k)$, otherwise the wave would propagate indefinitely. From Maxwell's equations, one may derive simplified dispersion relations (eq. 2.3 and 2.4) in the case of a planar surface (e.g. semi-infinite metal), having the dielectric function ($\epsilon_1 = \epsilon_1^{'} + i\epsilon_1^{''}$), and placed in parallel to a medium (given by ϵ_2, which is either in air or vacuum, in this case):

$$k_x = \frac{\omega}{c}\left(\frac{\epsilon_1\epsilon_2}{\epsilon_1+\epsilon_2}\right)^{1/2} \tag{2.2}$$

$$\frac{k_{z1}}{\epsilon_1} + \frac{k_{z2}}{\epsilon_2} = 0 \tag{2.3}$$

$$\epsilon_i\left(\frac{\omega}{c}\right)^2 = k_x^2 + k_{zi}^2 \tag{2.4}$$

Where eq. 2.2 is known as the dispersion relation. It is important to mention, that because of the differences in energy and momentum of incident light and the SPs, even if the dispersion relation arrives close to the light line $\sqrt{\epsilon_2}\omega/c$ at small k_z, the SPs cannot be excited and turned into "radiative". [24, 27] Or in other words, at a give photon energy $\hbar\omega$, for the photons to be "converted" into SPs, the wave vector $\hbar\omega/c$ has to be elevated by a value of Δk_{x} [24]. This can be done practically by introducing a coupler material with a higher dielectric constant (e.g., prism or waveguide) [28]). Then, if $\epsilon' \longrightarrow$ - ϵ_2) or k_z is large, ω becomes:

$$\omega_{sp} = \frac{\omega_p}{\sqrt{1+\epsilon_2}} \tag{2.5}$$

Due to the fact that the SPR system with the prism coupler is employed, in the next section coupling with the ATR (attenuated total reflection) coupler, will be overviewed.

2.1.1 Excitation of Surface Plasmons by Attenuated Total Reflection (ATR) coupling

When light is reflected from the metal surface, which has an adjacent dielectric layer (ϵ_0>1; e.g., quartz half cylinder or prism), the momentum of the light turns out to be $\hbar\omega/c\sqrt{\epsilon_0}$ instead of $\hbar\omega/c$. Then its projection on the interface is:

$$k_x = \sqrt{\epsilon_0}\frac{\omega}{c}\sin(\theta_0) \tag{2.6}$$

Where ϵ_0 is the permitivity of the dielectric medium (not of vacuum, in this case) and θ_0 is the incident angle of incoming light. Then

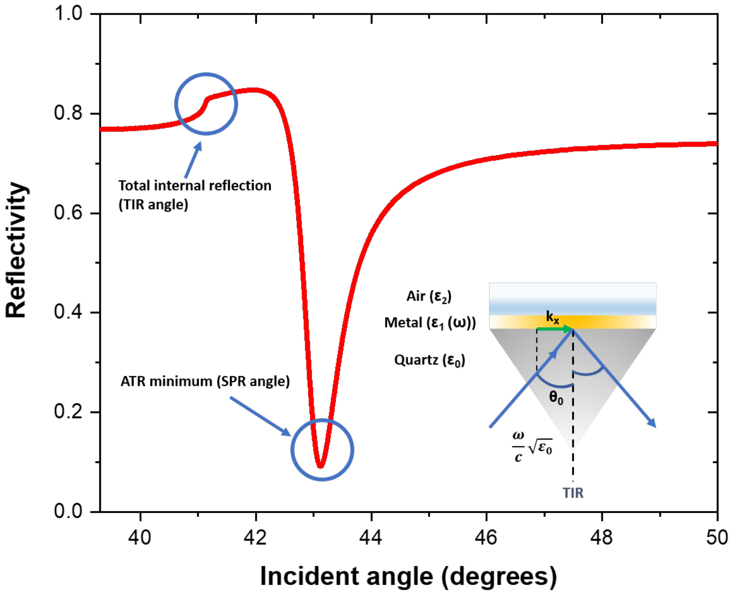

Figure 2.3: An angular SPR spectrum is presented, where the incident light coupling with the SPs is shown as the minimum in the spectrum at 43 degrees and denoted as the SPR (surface plasmon resonance) angle. Total internal reflection angle (TIR) is such, at which the light with a momentum $\omega/c\sqrt{\epsilon_0}$ is fully reflected from the metal surface at the same angle of incidence.

the dispersion relation meets its requirements in order to match the energy and momentum of the incident light (prism/metal interface) and the SPs (air/metal interface). The excitation of the SPs is then observed as the reflectivity minimum in fig. 2.3. This system is known as the Kretschmann-Raether configuration [21] and is commonly depicted in nowadays Surface Plasmon Resonance software as the angular scan. In the Figure, we observe the total internal reflection angle (TIR), which happens when light travels through one medium with a refractive index n_1, which is bigger than n_2. It is then fully reflected when the angle of incidence is higher than the critical angle θ_c [29]. Also, in this context, it is important to mention Snell's law, which describes how light is transmitted through an interface of two media:

$$n_1 \sin(\theta_i) = n_2 \sin(\theta_t) \tag{2.7}$$

And from this equation, the critical angle of incidence, at which TIR occurs, is known to be:

$$\theta_c = \arcsin\left(\frac{n_2}{n_1}\right) \tag{2.8}$$

Therefore by employing TIR and SPR angle shifts from the angular spectrum (fig. 2.3) we can determine, whether the refractive index changes are evident locally on the metal surface (from SPR angle shifts) or in the bulk (from TIR angle shifts).

Moreover, one may try to look at the generation of SPs in this way also: because the SPs are excited at the interface of prism/metal (in the vicinity of the total reflection), the evanescent light wave, having the phase velocity $\nu = \omega/k_\mathrm{x} = c/(\sqrt{\epsilon_0}\ \sin\theta_0\ (>1))$ will propagate in the interface with the phase velocity, which is equal or smaller than the speed of light. Also, note that the light's intensity decreases exponentially going along the metal layer if the excitation is done not on the whole film at once. [21, 24] Nevertheless, the SP resonance condition is accomplished, because the evanescent wave and the SP wave is equivalent:

$$\omega/k_x^0 = c/(\sqrt{\epsilon_0}\sin(\theta_0) \tag{2.9}$$

Where k_x^0 indicates the wave vector in the interface between the metal and dielectric.

Lastly, the ATR minimum, as observed in Figure 2.3, may be quantitatively described by the Fresnel's equations for the three medium system - dielectric medium (e.g. quartz), metal layer with a certain thickness d and the second dielectric (e.g. vacuum) and will be reviewed in the next section.

2.1.2 Fresnel coefficients and modelling

Generally, in surface plasmon resonance experiments, it is possible use the equation 2.10 [30] in order to determine, whether a binding event occurs on or within the layer of interest:

$$R = S(n_f - n_b)(1 - \exp(-2d/\delta)) \tag{2.10}$$

where R is the angular response, S is the sensitivity of the SPR response, n_f and n_b are refractive indexes of the surface adsorbed film and the bulk solution, d is the thickness of the film (in nanometers) and δ is the length of the evanescent field. The equation 2.10 may be applied only when the refractive index of the film of interest is not very different from the refractive index of the bulk solution. [31, 32]

However, it suffers from the limitation of not being able to determine the decay length of the evanescent wave theoretically. In contrast, Fresnel coefficients may be applied to model single interface as well as multilayer systems in terms of how much transmitted light goes through or is reflected from the modelled system.

Fresnel coefficients range in values between zero and unity and depict how much light is either transmitted or reflected (in relative intensities). There is one coefficient each for s or p polarizations and transmitted and reflected light (four in total in terms of Fresnel coefficients). We are only concerned about Fresnel coefficient for p-polarization (default in the used SPR instruments), which has its electric field exponential decay component perpendicular to the surface (z axis, fig. 2.2. Coefficients for the reflected and transmitted p-polarized light can be expressed through Snell's law mentioned beforehand (eq. 2.7) with equations 2.11 and 2.12 in the case of a single interface system [29]:

$$F_{rp} = \frac{n_1\sqrt{1-\left[\frac{n_1}{n_2}\sin(\theta_i)\right]^2} - n_2\cos(\theta_i)}{n_1\sqrt{1-\left[\frac{n_1}{n_2}\sin(\theta_i)\right]^2} + n_2\cos(\theta_i)} \tag{2.11}$$

$$F_{tp} = \frac{2n_1\cos(\theta_i)}{n_2\cos(\theta_i) + n_1\sqrt{1-\left[\frac{n_1}{n_2}\sin(\theta_i)\right]^2}} \tag{2.12}$$

Moreover, it is important to have a look at a 3 material system (e.g., 2 interfaces; single layer), where the thickness of the metal is smaller than the width of light and the coherence length. This results in the encounter with the reflected wave, carrying a phase shift, from the interface of metal and air (denoted as 2 and 3) and the incident wave when it reflects at the interface of the dielectric and metal (1 and 2, respectively) as seen in fig. 2.4. In this case the Fresnel coefficients include light interference, because the light is perfectly coherent (d is way smaller than the coherence length) and are expressed as follows:

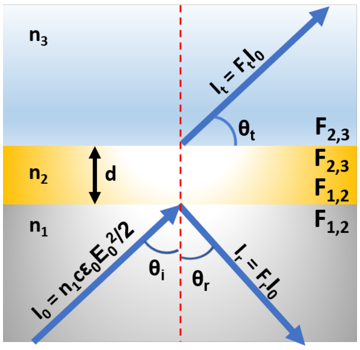

Figure 2.4: Illustration of transmitted and reflected light beams, when the distance d is smaller than the coherence length of the incident light.

$$F_r = \frac{F_{r,12} + F_{r,23}e^{i2k_0dn_2\cos(\theta_2)}}{1 + F_{r,12}F_{r,23}e^{i2k_0dn_2\cos(\theta_2)}} \tag{2.13}$$

$$F_t = \frac{F_{t,12} + F_{t,23}e^{ik_0dn_2\cos(\theta_2)}}{1 + F_{r,12}F_{r,23}e^{i2k_0dn_2\cos(\theta_2)}} \tag{2.14}$$

where k_0 is the free wave vector and is used to correlate the distance d and the wavelength λ_0 due to evident light interference. However, in order to determine the new transmitted angle (further expression of eq. 2.7) we employ the following equation (from Snell's law):

$$\begin{aligned} \theta_{j+1} = \operatorname{Re}&\left(\arcsin\left(\frac{n_j}{n_{j+1}}\sin(\theta_j)\right)\right) \\ &- i\left|\operatorname{Im}\left(\arcsin\left(\frac{n_j}{n_{j+1}}\sin(\theta_j)\right)\right)\right| \end{aligned} \tag{2.15}$$

Where j is just a counter (e.g. for the number of terms). Equation 2.15 may be used in order to describe systems with several layers, but gives an imaginary part that is negative (necessary in order to implement into computer software).

Lastly, due to the fact, that SPR sensors contain more than one layer the so-called *matrix transfer* method has to be applied in order to model the typical SPR spectrum, which includes the TIR and SPR angles (fig. 2.3):

$$\begin{aligned}\Phi = \prod_{j=2}^{m-1} \Bigg(\frac{1}{F_{t,[j-1]j}} \begin{bmatrix} 1 & F_{r,[j-1]j} \\ F_{r,[j-1]j} & 1 \end{bmatrix} \\ \times \begin{bmatrix} e^{-ik_0 d_j n_j \cos(\theta_j)} & 0 \\ 0 & e^{-ik_0 d_j n_j \cos(\theta_j)} \end{bmatrix} \Bigg) \\ \times \frac{1}{F_{t,[m-1]m}} \begin{bmatrix} 1 & F_{r,[m-1]m} \\ F_{r,[m-1]m} & 1 \end{bmatrix}\end{aligned} \tag{2.16}$$

Where m is a medium. It takes into account intensities, that are transmitted or reflected through/from individual boundaries, because they are the final products of the measurement. Also, in, e.g. semi-infinite medium m, there is no inclusion of the light wave reflected backwards (no light interference accounted for). [29] In order to understand how much light has been reflected or transmitted, the matrices have to be multiplied together and the final Fresnel coefficients for transmission and reflection will be achieved:

$$F_{Rp} = \frac{\Phi(2,1)}{\Phi(1,1)} \tag{2.17}$$

$$F_{Tp} = \frac{1}{\Phi(1,1)} \tag{2.18}$$

2.1.3 Non-interacting molecules method for polymer brush height determination

In this subsection, the non-interacting molecules method will be briefly discussed as it was employed to determine the dry, swollen and collapsed PNIPAM polymer brush heights with the help of Fresnel coefficient modelling. The method was first proposed by Schoch and Lim [32], and further extended by our group [19]. Its importance has risen due to the issue of modelling a hydrated film, where, because of the convoluted refractive index (e.g. due to solvent interactions influencing polymer swelling), the thickness cannot be determined anymore. For example, the solvent molecules

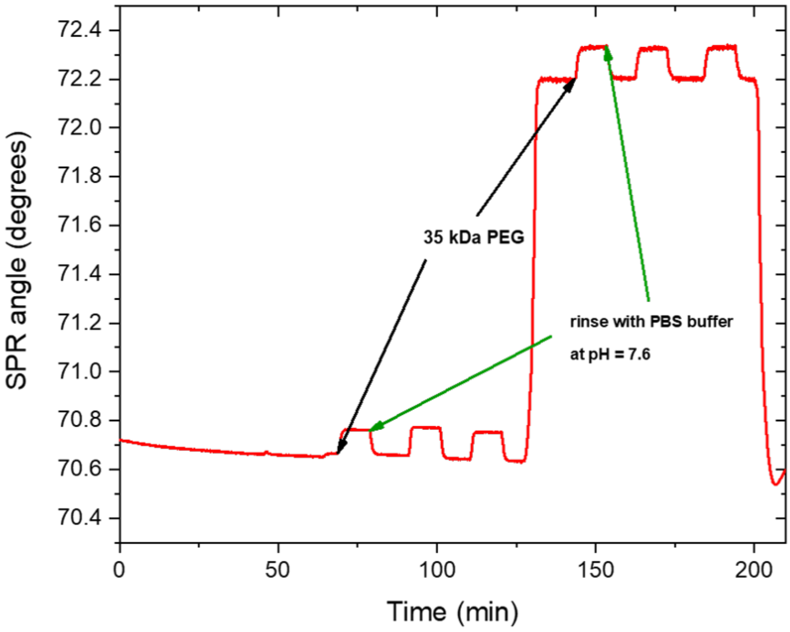

Figure 2.5: In the Figure, the SPR angle change as a function of time is illustrated. The non-interacting molecules of 35 kDa PEG are injected over a hydrated polymer brush film and above the LCST of PNIPAM and rinsed off completely with the running phosphate buffer (PBS).

could penetrate the film and then the film's refractive index is something in between the solvent's and pure film's. Consequently, either the solvated film's thickness or its refractive index have to be determined separately in order to determine the other according to eq. 2.10.

The principle of the non-interactive probe method is to inject a certain type of molecules over the film of interest (fig. 2.5), retrieve the changes in bulk refractive index (with and without the probe; from the TIR angle) and model the films in solution spectrum with Fresnel coefficients. The injected molecules (probes), in this case poly(ethylene glycol)(PEG), should not interact with the layer (e.g., polymer brushes; no irreversible interaction observed after injection and rinse steps in fig. 2.5) and the event of reversible adsorption (or even lack of) can be observed when plotting SPR angle changes as a function of TIR angle changes (fig. 2.6).

If the SPR angle changes as a function of TIR angle changes plot gives linear correlation, it means the chosen molecules are indeed not interacting with the film. However, if the plot gives a wide hysteresis, then the probes are not suitable, because they are interacting with the film.

When the refractive index and the thickness of the film of interest are unknown, the non-interactive molecules method may be applied. Schoch and Lim [32] suggest the usage of lower molecular weight PEG molecules as a reference in order to deduce the difference in sensitivity (perpendicular to the sample surface), which is

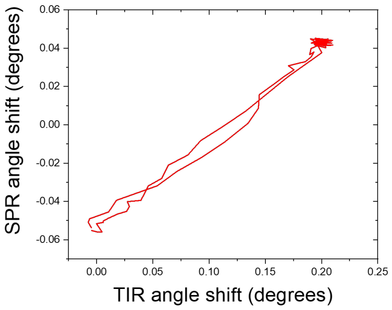

Figure 2.6: SPR and TIR angle changes plotted against each other upon injecting 35 kDa PEG over PNIPAM polymer brushes at room temperature.

presented as the decay length δ (for the dielectric medium (ϵ_0)):

$$\delta \approx \frac{\lambda_p}{2\pi}\sqrt{\frac{-\epsilon_0^2}{\mathrm{Re}(\epsilon_1)+\epsilon_0}} \tag{2.19}$$

where λ_p is the plasmon wavelength, ϵ_1 and ϵ_0 are the dielectric constants of the metal and the dielectric, respectively. The way this equation (2.19) was derived can be found in previously mentioned authors work [31, 32]. However, it is significant to know that this way of determining the wetted film thickness is rather limited, because it may be used for such film refractive indexes, that are close to the refractive indexes of bulk solution (between 1.33-1.4). Therefore, in order to use it in the case of polymer films, where the refractive indexes may not be similar to the bulk, it is necessary to do a full Fresnel coefficient modelling over a variety of refractive indexes described by Emilsson et al. [19]. This approach is based upon using the acquired angular spectrum of the film of interest in aqueous medium and considering several different thicknesses and varying refractive indexes in order to fit the spectrum with Fresnel modelling. Afterwards, the spectrum, where the non-interactive probe was injected over the film has to be fitted (bulk refractive index change is known from the TIR angle) the same way. Lastly, the refractive index and thickness of the film pair, intersecting with a certain pair fitted for the non-interacting probe angular spectrum, results in the wet thickness of the film at a particular refractive index (e.g., fig. 2.7; n is denoted as the refractive index and d is the thickness of the PNIPAM polymer brushes).

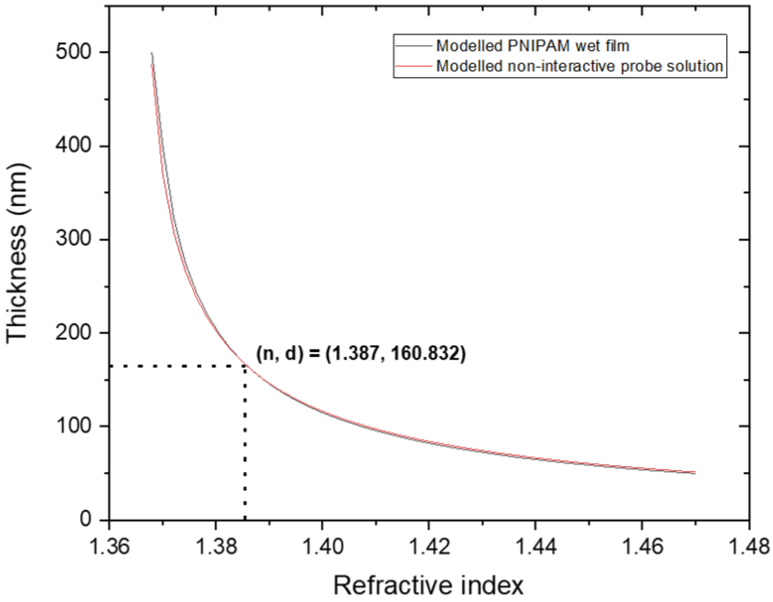

Figure 2.7: Modelled angular spectra of reference (PNIPAM polymer brush film without the probe) and brush surface with non-interactive probe 35 kDa PEG in PBS solution at pH = 7.6 intersecting at a singular n and d pair.

2.1.4 Plasmonic nanostructured surfaces

Plasmonic nanostructured surfaces are used as substrates, from which the PNIPAM polymer brushes are grown by ARGET-ATRP. In conjunction, they result in a biosensing platform, which relies on the SP grating coupling mechanism as described by Raether [24, 33]. Nevertheless, it is important to mention two resonance modes, which determine the SPR effect in arrays of nanoholes - localized (from individual holes in an array) and one resulting from the periodicity of the holes.[34–36]. It is enough to have distances between nanostructures, which range up to ~300 nm (in our case) in order to result in the SPR effect [35, 36]. Therefore the excitation of SP condition can be expressed in:

$$\frac{2\pi}{\mathrm{Re}(k_x)} j = P \tag{2.20}$$

where P is the periodicity of the nanostructures in the array and the left side of the equation is denoted as the surface plasmon wavelength multiple. In the case of short-range ordered arrays, P is described as characteristic spacing between the nanopores. Due to the fact that the surface plasmons are excited on a surface containing periodic holes in these kind of arrays, characteristic asymmetric resonance denoted as "Peak" and "Dip" in typical extinction spectrum may be observed (will be discussed more in section 2.3) [37].

2.2 Polymers

Polymers are chains of covalently interconnected molecules, monomers, as suggested by Staudinger in 1920 [38], however, they primarily differ from other molecular chains by being large in size. Even though polymers have been around in nature throughout history, people knew nothing about their structure, but have been utilizing these macromolecular chains on day-to-day basis. One of many biopolymeric examples found in nature is the natural rubber known as *caoutchouc* and before anybody realized it was a polymer, it was utilized in making water proof roofs, containers and even balls for the Mesoamerican ball game at least 3670 years ago [39, 40]. Moreover, in the middle of 1900s, chemists have been synthesizing polymeric chains without knowing they were really large molecules, but around that time most of the fundamental concepts have already been noted. Therefore, fundamental concepts, which will be talked about in this chapter, will mainly include work from the middle 1900s as well as some newer macromolecular properties of polymeric brush materials.

2.2.1 Polymer chains

As mentioned beforehand, polymeric chains consist of smaller repeating units called monomers. The process of polymerization describes linking these smaller blocks covalently and the assembly into a polymer. By estimating the **degree of polymerization** N it is possible to know how many monomeric units are comprising the macromolecule of interest. Then the total molar mass of the polymer can be determined by:

$$M = NM_{monomer} \tag{2.21}$$

where $\mathrm{M}_{\mathrm{monomer}}$ is the molar mass of one monomeric unit in the chain. An example drawn structure of polymers can be seen in Figure 2.8, where the polymerization of vinyl monomers took place (R is any kind of chosen chemical moiety). The polymerization degree N can be shown after the brackets or in order to denote the number of specific monomers in the polymer and avoid the possible complexity when polymers consist of different types of monomers, small letters are used instead. For example, if there are two types of monomers in the polymer chain, then N will be equal to the sum of n and p (indicates another type of monomer than n), etc. monomers.

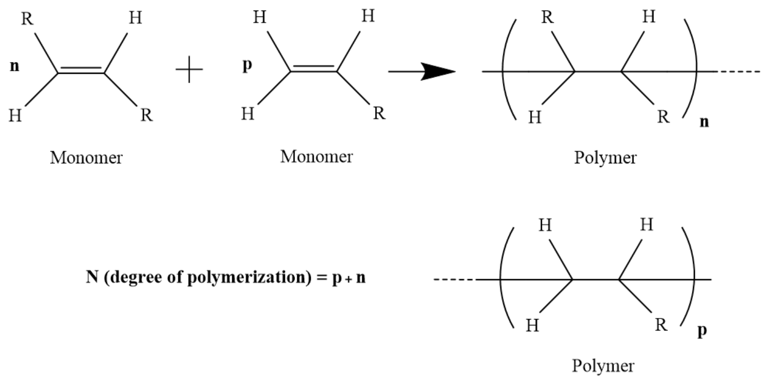

Figure 2.8: An example of a chemical structure of a polymer.

Polymer chains, that only contain one type of monomer are known as **homopolymers**. Linear polymers may have billions of monomers, therefore when they are connected with so many others, their physical characteristics are not the same anymore. For example, the boiling point rises with the number of backbone monomeric units and consequently results in varying utilization.[41] In addition, macromolecules can have different shapes (e.g., dendrimer, linear, ring, etc.) or types of monomers, which result in **heteropolymers** (e.g., deoxyribonucleic acid (DNA), which may contain 20 billion monomers).

While the degree of polymerization is one of the more important parameters in regard of polymer chains, radius of gyration R_g, Kuhn's length b and polydispersity I have to be mentioned as well (in the scope of a *freely jointed chain model*). The radius of gyration, which characterizes size of any polymer chains, can be expressed as [41]:

$$R_g^2 = \frac{1}{N}\sum_{i=1}^{N}(R_i - R_{cm})^2 \tag{2.22}$$

It defines the average squared distance $\mathrm{R_i}$ between each monomer in a given environment and the chain's center of mass $\mathrm{R_{cm}}$. The following two equations describe Kuhn's length and polydispersity index of the polymeric chains (equations 2.23 and 2.24, respectively):

$$b = \frac{\langle R^2 \rangle}{R_{max}} \tag{2.23}$$

$$I = M_w/M_n \tag{2.24}$$

In eq. 2.23 $\langle R^2 \rangle$ is mean-square end-to-end distance ($\langle R^2 \rangle$ equal to nb^2), which are number of monomers and bond length (the bond vectors are not correlated), R_{max} - the length of a rod-like polymer, and b is the Kuhn's length (within the random-walk model), also known as a stiffness parameter.

Polymer solutions are found with a distribution of different lengths of chains or molecular weight, which may result from many factors such as chain termination. Therefore, an estimate, representing this distribution, called the polydispersity index, can be estimated with eq. 2.24. M_w and M_n are weight-average and number-average molar masses (the larger the ratio is, the broader distribution of polymer chain molar masses in the sample). M_n takes into account a fraction of molecules with a specific N, whereas M_w considers the weight fraction of individual chains to contribute to a certain molecular weight [41].

Because significant parameters in the framework of polymer chains have been introduced, it is important to understand how the free energy of the chain relates the *chain conformational entropy*, *excluded volume entropy* and interaction with the solvent surrounding the chain. The reason for this is because together these terms may give clues how the chain behaves in a certain medium. Firstly, the excluded volume entropy includes a certain volume of, e.g. one polymer segment, that cannot be occupied by another, giving an increase in free energy (expressed by eq. 2.25). Secondly, by still assuming the freely joint chain and random walk model for a polymer chain, the conformational entropy is taken in regard of end to end distance (eq. 2.26).

$$\Delta S_{seg} = -\frac{k_B N \nu}{r^3} \tag{2.25}$$

$$S = constant - \frac{3k_B r^2 \nu}{2abN} \tag{2.26}$$

where k_B is Boltzmann's constant, r is the polymer chain end to end distance, ν - the excluded volume of one monomeric unit, a is the monomer size (e.g. length of a step in a random walk model) and b is the Kuhn's length, which, in opposite to a, is dependent of the previous taken steps of the Kuhn segment chain. By knowing these components, we can derive an expression of total free energy of a polymer chain:

$$G(r) = \frac{3k_B T r^2}{2abN} + \frac{k_B T \nu N^2}{r^3} - \frac{k_B T \nu \chi N^2}{r^3} + constant \tag{2.27}$$

This equation can further be simplified:

$$G(r) = \frac{3k_B T r^2}{2abN} + \frac{k_B T \nu N^2}{r^3}[1 - \chi] + constant \tag{2.28}$$

The interaction term contains a dimensionless factor χ, which includes polymer-polymer, polymer-solvent and solvent-solvent interaction energies [42]. If χ is taken to be unity, the so-called *theta solvent condition* will be reached. This means that the solvent interaction energies are completely counteracted by the excluded volume effect. If the factor χ is below unity, then the polymer chain is in a coil shape, but when χ is above unity, the polymer is considered to be in a globule state. By having polymer chains in different media, it is possible to assess different scaling laws in terms of the chain end to end distance R and the degree of polymerization N as seen in fig. 2.9.

Figure 2.9: Different scaling factors of polymer chains according to the dominating interactions (e.g. polymer-polymer or polymer-solvent) resulting in varying shapes of polymer chains in solution.

In the next section, polymer chains tethered by one end on a solid surface and free on the other will be overviewed.

2.2.2 Polymer brushes

Polymer brushes are known to be tightly packed polymer chains, which are tethered by one end to the surface or an interface (e.g., solid-air, solid-liquid, liquid-liquid) and free in with the other end

[43–45] and have first been studied as possible anti-flocculants for colloidal particles in the 1950s [46]. It was realized back then, that the repulsion between polymer brush functionalized particles come from the significant hydration of the brushes, which results in high osmotic pressure [45].

Consider the formation of the polymer brush layer. Upon the attachment of the polymer chains, a packed layer of polymer chains is achieved, consequently, leading to the stretching of the chains from the surface into the medium of interest. On the other hand, compared to polymer brushes, free polymer chains in solution tend to adapt a random-walk conformation [45]. This conformational difference gives polymer brushes different properties over the typical polymer chains in solution and result in a variety of applications such as anti-fouling surfaces [47], adhesive materials [48], model systems of surfactants [43], etc.

There are many variations of polymer brushes ranging from micelles, grafted polymers (also copolymers) on solid substrate and others. The shared characteristic among these different configurations is that polymer chains are elongated (fig. 2.10). Due to available vast literature about different types of polymer brushes, only homopolymer end-grafted polymer brushes will be discussed in this thesis.

2.2.3 Polymer brushes in a solvent

Alexander [49], de Gennes [50] and Cantor [51] were the first researchers, who explicitly remarked unique properties of tethered polymer chains in the late 1970s - early 1980s. Primarily numerical and analytical Self-Consistent Field (SCF) estimations described the structure of end-attached polymer chains.

In order to get a better view of how end-attached polymer chains behave in a certain medium, one has to consider several factors. To begin with, polymer brush configurational free states are limited due to the fact that polymer brushes are located at an interface. Because there are other densely packed chains around on the interface as well, the monomer-monomer interaction is enforced by increasing the number of contact points in the event of overlapping of the chains. Consequently, the polymer chains are stretched away perpendicular to their grafting points, reducing the local monomer concentration in the film and increasing its thickness, L. In addition, because the polymer brushes are now stretched, the interaction energy G_{int} per coil is lowered by increasing the elastic free energy G_{el} and then the overall free energy between two segments (eq. 2.29; notation of F, according to cited literature, was changed to G in order to make it more clear) is minimized by Alexander's model

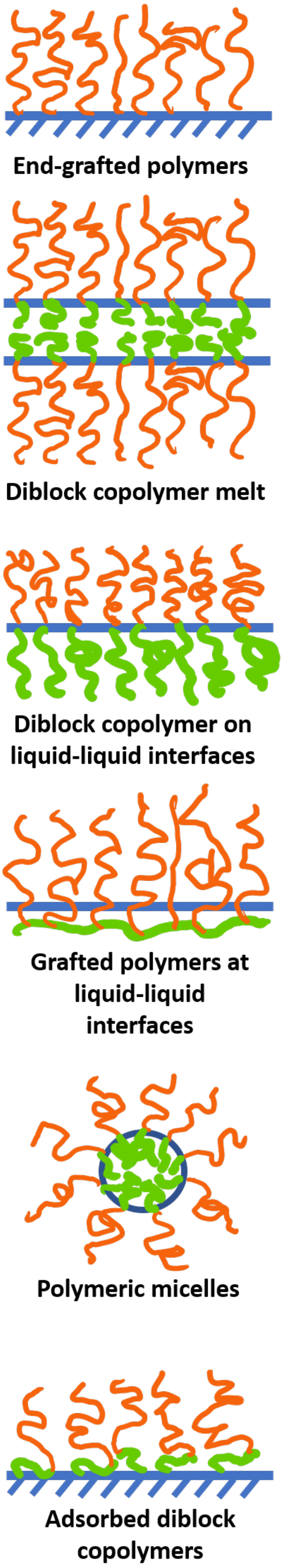

Figure 2.10: Polymer brushes in different configurations.

[49]. With it, it is possible to describe a non-adsorbing, even surface, where the monodisperse polymer chains are end-attached. The brushes contain N statistical segments (e.g. monomeric units) with a certain diameter a, where the average length between the grafting points is d (significantly smaller than the radius of gyration of a free polymer chain).

$$G = G_{int} + G_{el} \tag{2.29}$$

Therefore the equilibrium thickness of the brush layer is governed by these two factors (additional one - the solvent contribution was discussed in section 2.2.1). However, in order to make these terms valid, one has to assume that the depth profile of the statistical segments are considered in a step-like fashion, resulting in a constant segment concentration throughout the brush layer (e.g. $\phi = Na^3/d^2L$). In this case, all of the end-grafted polymer brush free ends are located at a spaced distance L perpendicular to the interface. [45]

One of the solutions for the free energy, which takes into account the reduction in configurational entropy from the ideal polymer random walk chain, is known as the *Flory approximation*. The free energy per unit chain is shown to be [45]:

$$G/kT = \frac{\nu\phi^2 d^2 L}{a^3} + \frac{L^2}{R_0^2} \tag{2.30}$$

where R_0 is the radius of an ideal, unperturbed polymer chain (e.g. proportional to $\mathrm{N}^{1/2}$ for linear chains). In addition, then the equilibrium thickness of the polymer brush film is achieved by minimizing the free energy G with respect to L and is presented by:

$$L/a = N\left(\frac{a}{d}\right)^{\frac{2}{3}} \tag{2.31}$$

This estimation describes how polymer brush equilibrium thickness scales with the degree of polymerization in a good solvent. However, depending on the medium the end-grafted (on a planar surface) chains are exposed to, the scaling relationship can be different (table 2.1) and, in fact, compared to free polymer chains, not similar at all [45, 52, 53].

Solvent	Polymer brush	Free polymer
Good solvent	$\mathrm{L/a} \sim N(a/d)^{2/3}$	$R \sim N^{3/5}$
Theta solvent	$\mathrm{L/a} \sim N(a/d)$	$R \sim N^{1/2}$
Poor solvent	$\mathrm{L/a} \sim N(a/d)^2$	$R \sim N^{1/3}$
Bulk state (or melt brush)	$\mathrm{L} \sim N^{2/3}$	$R \sim N^{1/2}$

Table 2.1: Polymer chain equilibrium thickness scaling in different media.

Alexander's method is a simple enough assumption for minimizing the free energy of polymer coils, because it depends on shifting the equilibrium between polymer chain-chain repulsion and stretching. Overall, it can be used further to describe hydrodynamic properties of the end-grafted brushes such as - hydrodynamic thickness, compressibility and permeability of the brush [45]. However, its limitation lies in not including where the chain ends are located at any time point, how the polymer chains separate or intermix with each other (when polymer brushes are of different length or comprise of different monomers) or the fundamental distribution of the chain unit density. [45] Nevertheless, the resulting parabolic polymer brush density profile then is:

$$\phi(x) \propto [L^2 - x^2] \tag{2.32}$$

where L is the height of the brush (denoted as "h" in the cited literature [49]) and x is the distance from the surface of interest. This estimation describes polymer brush layer density in a way, that at the points, where the chains are grafted, the function results in maximum value and at the outer edge of the film, in zero. However, in contrast to Alexander's [49] model, it does not assume that the brushes have their free ends of the chains at the same limited height. [54]

2.2.4 Polymer grafting techniques

Even though there are two most commonly applied methods (fig. 2.11) - grafting-to and grafting-from [55], through which polymer chains can be attached to a surface of interest, only grafting-from approach will be described more in detail in this section.

Nevertheless, in brief, grafting-to approach consists mainly of one step for attaching polymer chains on a surface and it is by having a certain functional end-moiety on a monomer (e.g., thiol or disulfide moieties), which binds to the substrate [56]. In this case, the polymers usually have a known molecular weight predetermined, therefore having an advantage over grafting-from approach, where the molecular weight is difficult to estimate,

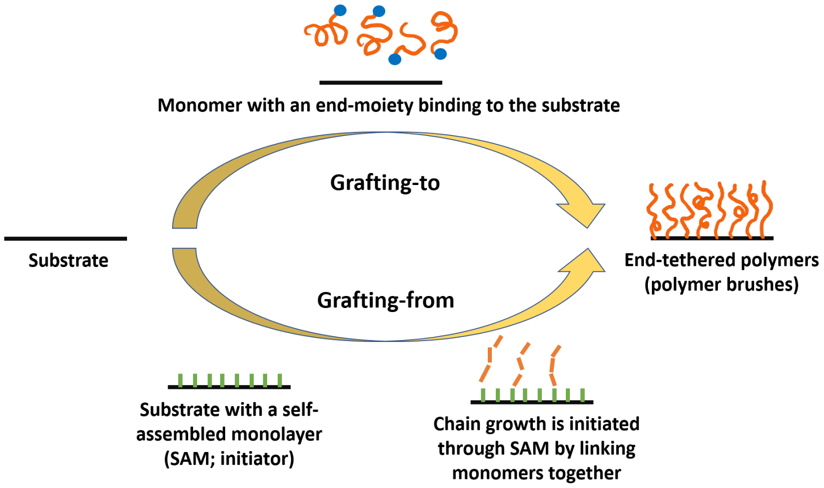

Figure 2.11: Two most commonly employed polymer chain tethering strategies.

because of low polymer concentration after cleaving them from the surface [57]. The main disadvantage of grafting-to approach is that it usually has lower grafting densities (for large polymers) compared to grafting-from method, which may result in different surface properties. For example, if grafting density is too low, in the event of protein adsorption, the penetration into the brush or even adsorbing onto the surface where it is not wanted to [58]. Therefore the grafting density Γ (chains/nm^2) is a highly significant parameter when trying to realize polymer brushes for a possible application and can be determined with the following equation if the polymer molecular weight is known [59]:

$$\Gamma = \frac{h\rho N_A}{M_n} \tag{2.33}$$

where, h is the dry thickness of the polymer film, ρ is polymer brush density, N_A is Avogadro's number and M_n is the number-average molecular weight as explained beforehand. If the polymer brush film thickness is not determined, then one may use an alternative approach including the surface area of the substrate and the cleaved weight of the polymer [60]. The grafting density can be related to the monomer volume fraction Φ inside the brush through Alexander-de Gennes solvated brush model as seen in the relation 2.34 [61]:

$$\Phi \sim g_D(a/D)^3 \sim \Gamma^{2/3} \tag{2.34}$$

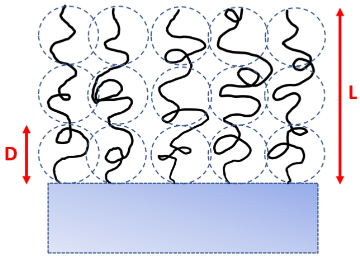

Figure 2.12: Alexander-de Gennes polymer brushes.

Where g_D is the number of monomers and D is the size of the blob as seen in Figure 2.12. A blob is a hypothetical region in a polymer chain, where a segment of the chain may occupy a certain volume in a particular conformation. The blob may contain several monomers and its size D is equal to $ag_D^{3/5}$. The volume per grafted chain is then equal to LD^2.

Moreover, when the distance between the polymer chains x is smaller than R_g, then the conformation of the brush results in a polymer chain assembly with a high grafting density (fig. 2.13; [56, 57, 62]). Controversially, if the distance between the polymer chains is higher than R_g, the polymers will occupy a mushroom-like state. In addition, grafting-from approach is not limited in terms of the polymer film thickness, which can be tuned by terminating and re-initiating the reaction, unlike the grafting-to method.

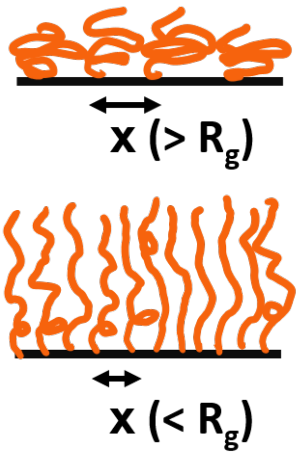

Figure 2.13: Polymers end-grafted to a planar surface in two different conformations due to varying distance between the chains.

Surface Initiated - Atom Transfer Radical Polymerization, or SI-ATRP, is one of the most popular grafting-from polymerization routes [62–65] for polymer chain tethering on a planar or a curved surface and was independently discovered by two groups led by Mitsuo Sawamoto [66] and Krzysztof Matyjaszewski [67] in 1995. Even though there are more than one mode of SI-ATRP, including, electrochemically [68] and light mediated [69] SI-ATRP, Activator Regenerated by Electron Transfer (ARGET) approach will be explained more in detail. The general mechanism for the reaction can be seen in Figure 2.14 [55, 56].

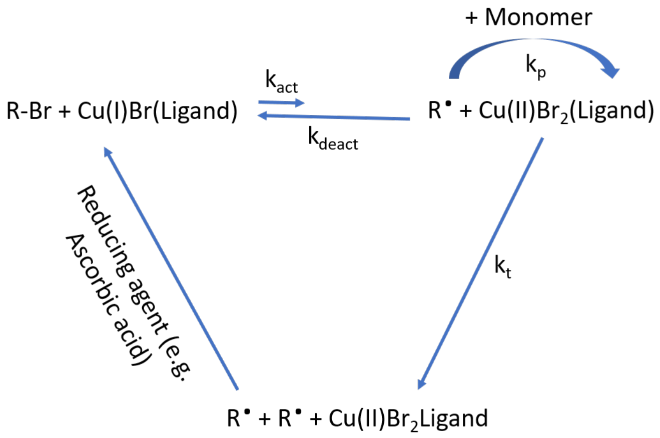

Figure 2.14: The mechanism of ARGET-ATRP.

The *R-Br* species is the self-assembled monolayer on a metal substrate, which has a bromide moiety. Consequently, it can be turned into a radical and initiate the polymer chain growth once the Cu(II) $Br_2(Ligand)$ is reduced to Cu(I) $Br(Ligand)$ by an appropriate reducing agent such as ascorbic acid (not denoted in the general ARGET-ATRP scheme in fig. 2.14). Cu(I) complex acts as a catalyst for the reaction due to Cu(I) complex oxidation, which, in turn, produces radical species $R\cdot$. The rate, at which the reaction activates, is denoted as k_{act} and, in contrast, the deactivation as k_{deact}. Therefore, the kinetics of the reaction is governed by the ratio between k_{act} and k_{deact}. Because in the equilibrium the deactivated species *R-Br* is preferred, the radical amount is limited. Moreover, once the chain propagation has started at a rate k_{p}, the resulting Cu(II) in the second step is being converted into Cu(I) by the reducing agent (e.g. ascorbic acid), which keeps continuing the reaction. The chain may be terminated at any point by introducing oxygen species (e.g. introducing ambient oxygen by opening the lid of the reaction vessel), which turns Cu(I) into Cu(II), or it naturally will terminate at a rate k_t or once the monomer is depleted.

ARGET-ATRP approach is preferred to other known ATRP methods due to the fact, that it most commonly may be applied in limited amounts of oxygen [70], which may otherwise result in a terminated polymer chain growth by oxidation of Cu(I) complex or the R· itself. In general, it is difficult to acquire optimized conditions for SI-ATRP reactions due to the fact that factors such as the type of catalyst [71], monomer and ligand [72], and their concentration [73], type of solvent mixture [74], temperature [75] and pressure [76] may influence the kinetics of the polymer brush growth.

The conditions from Emilsson et al. [19] have been adapted and further optimized in order to achieve more reproducible reaction in terms of homogeneity of the film and thickness.

2.2.5 Thermo-responsive polymer poly(*N*-isopropylacrylamide) (PNIPAM)

Stimuli-responsive polymers have become an exceptionally popular research are in the last decades. This is due to the fact, that by controlling their local environment, it is possible to change the polymer physical and chemical properties [77, 78]. Polymers are classified as stimuli-responsive, because they respond to certain external stimulation, which might be pH [79], temperature [80], mechanical force [81], electric/magnetic fields [82, 83], etc. These so-called smart materials have been applied as biosensors [84], in drug delivery [85], as coatings with self-healing capability [86, 87], for cell culturing [88] and other applications.

The stimuli-responsive polymer of interest is poly(*N*-isopropylacrylamide)(PNIPAM; fig. 1.2), which has been widely studied since it was first synthesized by Specht et al. in the 1950s [89]. The stimulus, which changes polymer's physical properties, is change in temperature. It is known that when the local polymer temperature has become 32 °C (in water), the chains undergo a coil-to-globule transition, because the lower critical temperature (LCST) of the polymer is reached, expelling up to 80% of its water content [90, 91]. This is due to the fact that polymer chains start favoring polymer-polymer interaction (e.g. hydrophobic interaction between methyl moieties in polymer chains) instead of polymer-solvent. This live-cell friendly transition temperature opens a pathway to use PNIPAM for possible biotechnological applications involving cells [92, 93] and biomolecules such as proteins [58, 90].

There are known 3 modes of protein adsorption to consider - primary, ternary and secondary adsorption as seen in fig. 2.15. The adsorption of proteins on PNIPAM brushes highly depend on the hydration of the brushes and their grafting density sites x ($\Gamma = 1/x^2$) [58, 94]. The former correlates to the fact that the water amount contained by the polymer brush film translates to high osmotic pressure, therefore, preventing protein adsorption within the brush [94]. However, the osmotic pressure will depend on how closely packed the polymer chains are, e.g., the higher the surface grafting density Γ the higher the osmotic pressure. Nevertheless, the osmotic pressure penalty, if needed, may be overcome by reducing the quality of the solvent for the polymer in question [58, 95].

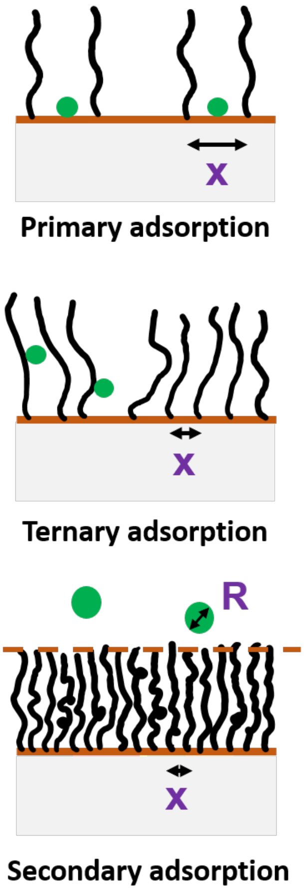

Figure 2.15: Different types of protein adsorption on polymer brushes depending on their grafting density sites x.

When the $R \ll x$, the adsorption can be primary or ternary [58]. In this case, the protein diffuses through the polymer brush layer and adsorbs on the substrate, on which the polymer is grafted. The adsorbed quantity of the protein is influenced by the attraction force between the protein and the substrate, and the polymer brush characteristics. When $R \gg x$, proteins could adsorb on the outer plane of the polymer brushes (e.g. the limit, where the proteins cannot penetrate in to the film anymore) through interaction with the polymer chains or long-distance attraction force with the substrate. In addition, if R is in the intermediate range between the primary and secondary modes, the protein of interest could penetrate into the brush film, but not as far as to reach the substrate (e.g. ternary adsorption) [96, 97]. These explanations give a clear view for further directions in order to optimize grafting conditions for polymer brushes in order to avoid possible protein adsorption. However, the fundamental reasons, describing the reversible protein adsorption, for example, on PNIPAM functionalized surfaces, are still not established [58]. Lastly, it is important to mention, that more complex protein adsorption over long periods of time (e.g. 6-72 hours) have been observed before [90] and can be influenced by protein-polymer hydrogen bonding (e.g. for PNIPAM polymers), steric exclusion [98], surface disorder [99] or protein denaturation [100].

2.2.6 The co-nonsolvency effect

When PNIPAM polymer brushes are in good solvent (e.g. water or methanol) conditions, the chains occupy extended conformation [101] and the polymer solution is transparent. However, if a certain volume of another good solvent for PNIPAM is incorporated, the polymer solution might become visibly turbid [102]. This effect was first described within the standard Flory-Huggins theory and called the co-nonsolvency effect [103]. It takes place when two, otherwise good solvents, e.g. water and methanol, for PNIPAM, are mixed together in the presence of the polymer chains and become a poor solvent. This type of polymer - 2 solvent component mixture often leaves some polymer chains in collapsed, partly collapsed or partly extended conformation [101, 102, 104]. The possible explanations for this effect have been addressed: the hydrophobic parts of PNIPAM hydration is modified by methanol [105], cooperative binding of water and methanol to PNIPAM polymer chains in segments [106–108] and bridge formation between PNIPAM chains induced by methanol [109].

As mentioned in the previous section (section 2.2.4), during ATRP polymerization the solvent composition is crucial in order to optimize the polymer brush homogeneity as well as thickness. Some studies revealed that in order to achieve relatively fast and controlled polymerization conditions for PNIPAM polymer brushes, one has to find a rather fixed range of molar fraction χ for one solvent component in comparison with the other [110]. Another study showed, that rather linear polymer chain growth kinetics may be achieved when employing 50/50 (v/v) Milli-Q (MQ) water-/MeOH solvent mixture [19]. In the case of methanol/water solvent mixture, it has been reported that molar fraction of methanol for fast and controlled growth should be kept between 0.16 and 0.31 [110]. However, some studies show uneven water/methanol distribution around the PNIPAM polymer brushes compared to the bulk solution when $\chi_{Methanol}$ is between 0.17 and 0.5 due to complexation between water and methanol through hydrogen bonds [111–113]. Others say that PNIPAM chains become soluble only when $\chi_{Methanol}$ is below 0.13 or above 0.4 [105]. Therefore, it seems, optimizing the polymerization of PNIPAM polymer brushes in mixed solvents remains a challenging task even though it could prove worthwhile in terms of reaction kinetics and film uniformity. Nevertheless, the co-nonsolvency effect has been exploited for several applications so far including tunable friction of PNIPAM coatings [101], adhesion of nanoparticles [114] and determining the enantiomeric excess of some chiral molecules [115].

2.3 Extinction Spectroscopy

Extinction, or the sum of absorption and scattering of incident light, refers to the asymmetric resonance, which is typical for small periodic apertures in thin gold layers [37]. These have been mentioned beforehand and will be referred to as nanowells (the fabrication of these will be briefly discussed in the method section). Nevertheless, the plasmonic resonance results in "Peak" and "Dip" in the extinction spectra as seen in Figure 2.16.

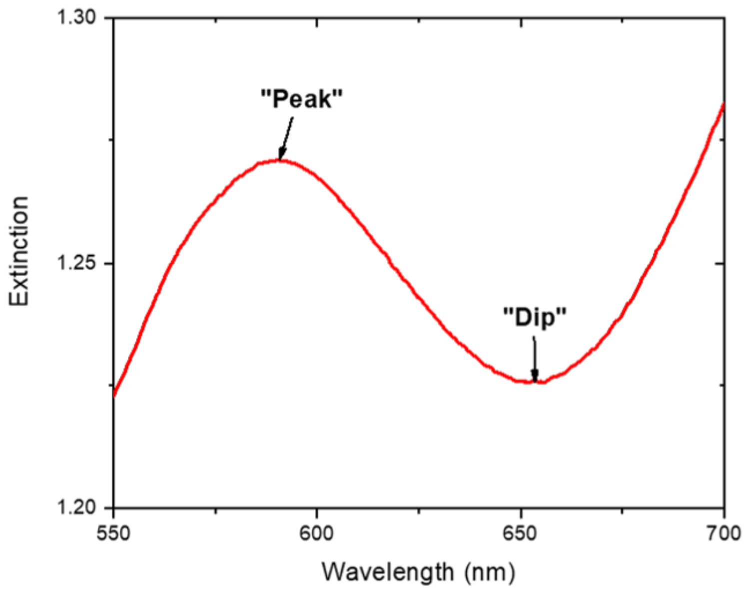

Figure 2.16: Asymmetric resonance modes of adsorption and scattering denoted as "Peak" and "Dip".

Our group has discussed different plasmon modes for these nanoscale apertures in previous work, including their refractive index sensitivity and sensing capability [33, 34, 36]. In addition, such holes in the gold film adapt similar properties to long ranged periodic holes. Therefore, the characteristic "Peak" (fig. 2.16) shows Bloch wave coupling to surface plasmons, which obtain symmetrically distributed charge densities on both sides of the gold layer. The wavelength of "Peak" will depend on the periodicity of nanopertures and the thickness of the gold film, but not the diameter of the pores, because it does not relate with the grating-mode coupling of the surface plasmons [116].

The characteristic "Dip", also known as the maximum of the transmission of incident light or the extinction minimum, is observed at longer wavelengths (fig. 2.16). This sensing mode is more focused towards the interior of the nanohole than "Peak", therefore changes in its wavelength, for example, can be attributed to molecule adsorption inside the nanoaperture. It is important to mention, that "Peak" is also sensitive to molecule binding inside the nanoholes, but to a lesser extent. The certain position, that the "Dip" occupies in the extinction spectrum, depends on the shape of the nanohole, whereas for "Peak", the periodicity of the nanopores is relevant [34, 116].

The sensitivity for local refractive index in these "Peak" and "Dip" modes depends on the volume of the nanowells, because when more liquid volume is present in the sensing field, the higher the change in the refractive index (if there is a change in liquid's refractive index) [14]. However, this is only relevant up to a certain distance from the metal, which spans roughly up to the thickness of the gold layer (~30 nm) [34, 116]. Also, even though it is known that the "Dip" has a higher sensitivity than "Peak", it shows a bigger noise level as well [34, 116]. The "Peak" sensitivity is estimated to be ~147 nm/RI unit and has a plasmonic field extension of ~50 nm [117], whereas the "Dip" sensitivity is ~278 nm/RI unit and its field extension mainly lies in the interior of the nanowell [14].

2.3.1 Real-time plasmon resonance shift monitoring

The real-time plasmon resonance shift monitoring may be viewed as the centroid position shift in "Peak" and "Dip" [118]. Then, the experiment-specific molecular binding is tracked by employing these shifts in "Peak" and "Dip". For example, in fig. 2.17 the binding of 2 kDa methoxy poly(ehytlene glycol) thiol (mPEG-SH) chains and bovine serum albumin (BSA) to the nanowells may be observed.

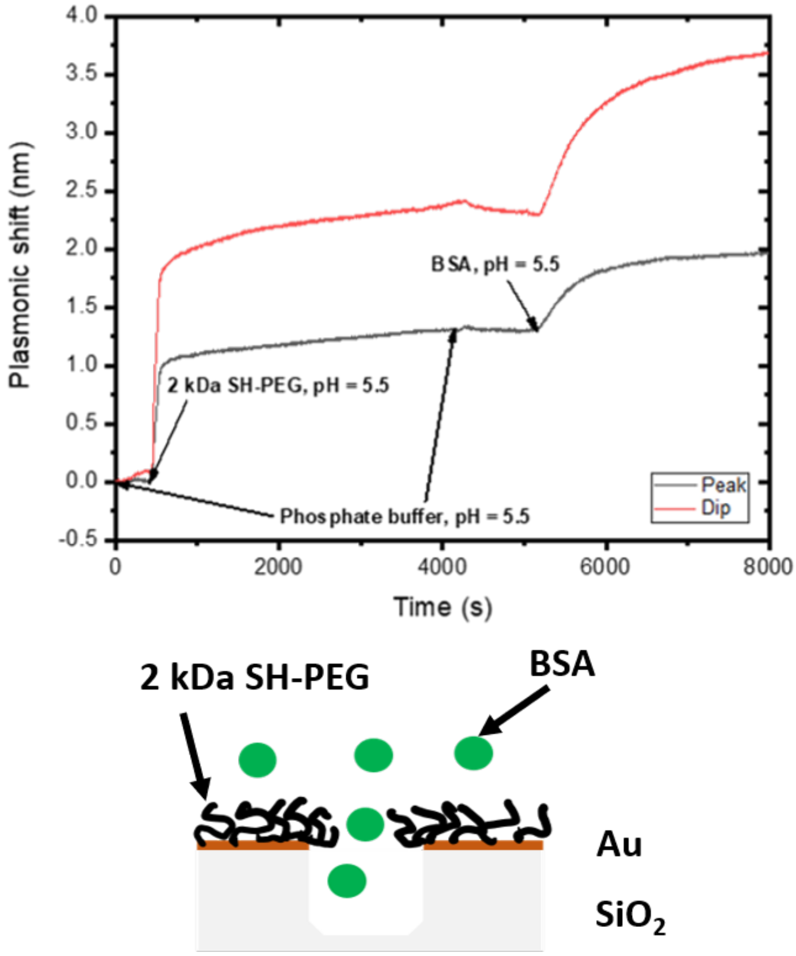

Figure 2.17: Real-time plasmonic shift of "Peak" and "Dip" upon binding of 2 kDa SH-PEG and BSA. The difference in shifts between "Peak" and "Dip" are due to discrepancies in plasmonic field extensions and their sensitivities.

Because the nanowells are fabricated in such a way to have two possible surfaces for the molecules to bind to (gold and fused silicon dioxide - the deeper interior of the nanowells), different plasmonic shifts in "Peak" and "Dip" may be observed due to their characteristic plasmon confinements. The "Dip" shift is higher than the "Peak", because, as it was mentioned beforehand and it is known, that for higher wavelengths the sensitivity is higher [118] (fig. 2.18). However, the "Dip" has more noise than the "Peak", because the uncertainty of tracking the "Peak" resonance wavelength is 0.01 nm, whereas for "Dip" it is 0.02 nm (for temporal resolution 200 ms), but also the "Dip" is a broader resonance [14]. Nevertheless, one can apply the discrepancies of sensitivities between "Peak" and "Dip" in order to determine if certain molecules have bound to the interior of the nanowell. This feature will be utilized to track molecular gating through the nanopores and discussed later on.

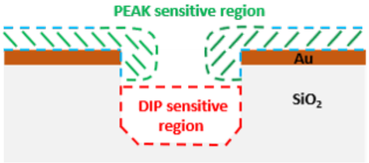

Figure 2.18: A representation of relative "Peak" and "Dip" mode plasmonic field sensitivity regions for nanowell structures. "Dip" sensitivity region is not as strictly pronounced as for the "Peak", therefore it might span over some of the gold film as well.

A parameter ζ may be defined as a measure for the degree of molecular localization in the interior of the nanowells:

$$\zeta = 1 - \frac{\Delta\lambda_{peak}}{\Delta\lambda_{dip}} \tag{2.35}$$

When ζ is ~0, mainly binding on the planar surface occurs, when it is 0.5, then no location is preferred and the binding inside the nanowells is indicated when the numerical value is close to unity [118].

In the case represented in fig. 2.17, ζ is 0.547 for BSA binding event, which indicates biomolecular binding preference inside the nanowells rather than on the surface [118]. However, this parameter should be utilized with caution, because the plasmonic shifts may change from batch to batch of nanostructure production due to the fact that the manufacturing process does not reproduce exactly the same structures (e.g. their depth might be slightly different, thus change the plasmonic shifts in "Peak" and "Dip").

2.4 Quartz Crystal Microbalance with Dissipation Monitoring (QCM-D)

An alternative choice to refractometric sensing methods mentioned before in sections 2.1 and 2.3 is an acoustic technique known as Quartz Crystal Microbalance with Dissipation Monitoring (QCM-D) [119–122]. This method's working principle is to measure adsorbed mass by generating acoustic waves with a piezoelectric crystal oscillation [120]. Sometimes it is referred to as a balance for the nanoscale objects. Piezoelectricity is described as an effect, when certain pressure is applied, which induces crystal lattice deformation, a voltage is generated by the piezoelectric material (e.g. quartz crystal; fig. 2.19) and vice versa [119].

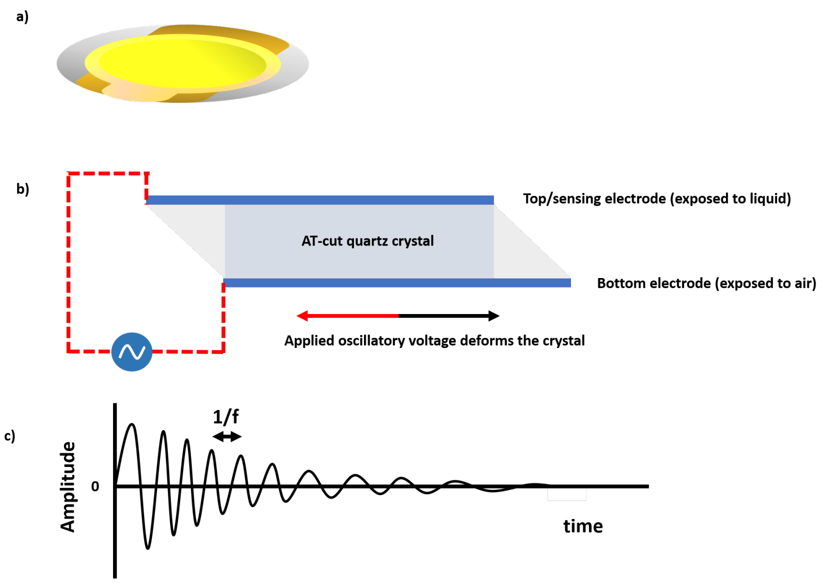

Figure 2.19: a) A QCM-D sensor can be seen with a gold layer deposited on top of the quartz crystal. b) When matching AC voltage is applied, the crystal starts oscillating laterally. c) The frequency is translated via Fourier Transform into time domain once the applied voltage is shut off and the crystal oscillates for some time at its resonance frequency.

In fig. 2.19 c) the oscillation of the quartz crystal has a certain amplitude, which is expressed by eq. 2.36) and decreases in time once the applied voltage is stopped.

$$A(t) = A_0 \sin(2\pi f_n t) exp(-D_n f_n t) \tag{2.36}$$

In eq. 2.36 f_n is the acoustic resonant frequency and D_n is the dissipation constant, which is dimensionless, because it describes energy loss per cycle of oscillation [29, 123].

The more in depth explanation for the working principle of QCM-D is such that when an AC voltage is applied, which is close to the quartz crystal's resonant frequency (or multiplied numbers, known as overtones (depicted as n)), the piezoelectric material will start oscillating. The oscillations of the crystal drags the gold electrodes on top and below the crystal leading to generation of acoustic waves (fig. 2.19 a) and b). Their resonant frequency is described by the equation:

$$f_n = n\frac{v}{\lambda} = n\frac{\nu}{2d_0} \tag{2.37}$$

where, ν is the speed of sound in quartz, n is an integer (odd number), d_0 is the thickness of the quartz crystal, λ is the wavelength of the standing wave between two gold electrodes and is equal to $2d_0/\mathrm{n}$. For example, if a 300 μm thick crystal is taken, the resonant frequency will be 5.57 MHz. The piezoelectric, used in a QCM-D experiment, is AT-cut quartz, which means that it produces shear type of oscillations [121].

Moreover, when molecules adsorb on, the gold layer, which is deposited on quartz, and form an adlayer, they will be included in the collective oscillation. Then the acoustic wave, produced by the quartz crystal, will be attenuated and the resonance frequency will be proportional to the mass of the adsorbed layer according to Sauerbrey's relation [120, 121]:

$$\Delta f_n = -\frac{n}{C} m_f = -\frac{n}{C} \rho_f h_f \tag{2.38}$$

where C is the so-called Sauerbrey's constant and is specific to the material characteristics of the quartz and its fundamental resonance frequency (e.g. for a quartz crystal with a density of 2.65 g/cm^3 this frequency is ~5MHz (corresponds to a crystal thickness of 330 μm)), ρ_f is adsorbed layer's density, m_f is the mass of the adsorbed film and h_f is its height.

In liquids, the shift in resonance frequency depends on the relationship between resonance frequency and liquid's density ρ_1 and viscosity η_1 [120]:

$$\Delta f_n = -\frac{1}{C} \sqrt{\frac{n \rho_1 \eta_1}{2 \omega_F}} \tag{2.39}$$

where ω_F is known as the angular fundamental resonance frequency. In short, equation 2.39 means that when there is a shift in resonance frequency, it is related to the viscosity and density of the liquid of interest. Therefore, in order to achieve quantitative information about the film properties, one always has to take a reference measurement of the liquid without the film in order to discern its coupled contribution [120]. However, Sauerbrey's equation only applies for rather rigid films. If the adsorbed layer, such as polymer brushes, has viscoelastic properties, more extensive modelling of the layer has to be performed (e.g. Voigt model [120, 124, 125]).

The Voigt model is relating the frequency (Δf) and dissipation (ΔD) changes to the viscoelastic properties of the adsorbed layer through the β parameter (equations 2.40, 2.41 and 2.42) [123, 124].

$$\beta = (1-i)\eta_f \delta^{-1} tan[(1-i)d_f/\delta] \tag{2.40}$$

$$\Delta f = Im\left(\frac{\beta}{2\pi d_0 \rho_q}\right) \tag{2.41}$$

$$\Delta D = -Re\left(\frac{\beta}{\pi f d_0 \rho_q}\right) \tag{2.42}$$

Where d_0 and ρ_q are thickness and density of the quartz crystal, d_f and ρ_f are thickness and density of the film and $\delta = (2\eta_f/\omega\rho_f)^{1/2}$. Parameter β is an equivalent variable to the generalized impedance Z^* (a complex number) as in the approach described by Johannsmann [124, 126]. Also, all the viscoelastic information about the adsorbed film is included in it.

In principle, the model takes into account the sum of the stresses acting on the material of interest due to viscous and elastic parts of the film, which will not be explained in detail here. However, in the framework of the model, the general expression for the adsorbed layer with thickness d_f and density ρ_f can be described by the complex shear modulus μ^*:

$$\mu^* = \mu' + i\mu'' = \mu_f + i2\pi f\eta_f = \mu_f(1 + i2\pi f\tau_f) \tag{2.43}$$

Where μ_f and η_f are known as the elastic shear modulus and shear viscosity, respectively, τ_f is the specific relaxation time of the adsorbed layer ($\tau_f = \eta_f/\mu_f$) and f is the oscillation frequency . Then β is achieved by working out the wave equation described by the Voigt model. Consequently, the final expressions of frequency and viscosity changes for a viscoelastic ultrathin film under a Newtonian liquid such as water is [124, 125, 127]:

$$\Delta f = -\frac{1}{2\pi\rho_q t_q}\left(d_f\rho_f\omega - 2d_f\frac{\eta_f\omega^2}{\mu_f + \omega^2\eta_f^2}\left(\frac{\eta_b}{\delta}\right)^2\right) \tag{2.44}$$

$$\Delta D = \frac{1}{2f\pi\rho_q t_q}\left(2d_f\frac{\mu_f\omega}{\mu_f^2 + \omega^2\eta_f^2}\left(\frac{\eta_b}{\delta}\right)^2\right) \tag{2.45}$$

The Sauerbrey equation 2.38 is a lesser version of equation 2.44 in the case of films, which have no viscous contribution.

Overall, QCM-D is known as a powerful tool to study solvated interfaces by helping to determine some of the adsorbed film's structure, thickness and also may give information about the solvent, which is coupled to the film. Also, it is able to measure physical and chemical changes in real-time and may give quantitative descriptions for the studied layers [120]. Some of this technique's applications include food processing, marine technologies and biosensors.

3 Materials and Methods

3.1 Materials

All relevant materials and chemicals may be found in Appendix A (table A.1). Furthermore, in this section, the applied methods in this thesis will be summarized and described. More detailed subsection information is indicated in the content table.

3.2 Methods

3.2.1 Nanostructure fabrication

The production of nanostructures has been done by another person of the group according to the process described in detail by Malekian et. al [14] (fig. 3.1).

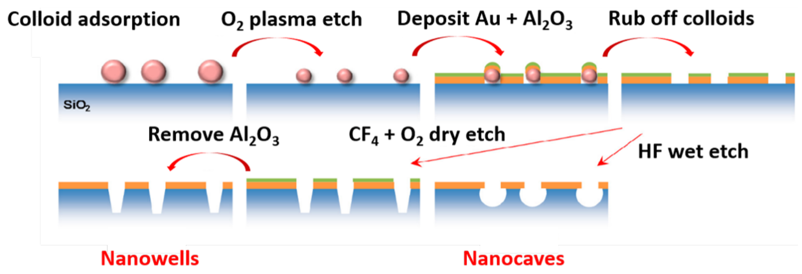

Figure 3.1: Step-wise preparation of nanowells and nanocaves. Taken from Malekian et al. [14].

However, in short, one has to utilize clean, fused and amorphous silica (SiO_2) as a support to begin with. Then, colloidal litography is utilized in order to structure a pattern for future nanowells or nanocaves. Consequently, oxygen plasma etching is employed in order to tune the diameter of the annealed colloids (e.g. polystyrene) to the wanted values. Gold (30 nm in thickness) and alumina (20 nm) films are deposited on the support together with the colloids by physical vapor deposition (PVD). A chromium layer (~ 1-2 nm) is used as an adherent for gold on silica support. The alumina layer serves as a protective film for gold in order to keep it uncontaminated and undamaged during the reactive ion etching (RIE) process. After the colloids are rubbed off softly, either "dry" or "wet" etching of the metal films is applied in order to produce the desired structure. In the case of "wet" etching (by hydrogen fluoride (HF)), the Al_2O_3 layer is removed with HF without damaging the gold. However, in the "dry" etching (by oxygen and carbon tetrafluoride mixture (1:4 ratio)) the alumina layer has to be removed afterwards, for example, with a weak base such as sodium hydroxide (NaOH) diluted solution. Finally, samples may be annealed in order to increase their stability by recrystalizing the gold at 250 °C for ∼ 1 hour or by employing the RCA-1 cleaning protocol described in 3.2.2.

3.2.2 Sample cleaning with Piranha and RCA-1 solutions

RCA-1 sample cleaning protocol - a newly produced or acquired sample surface is placed into a mixture of milliQ water, ammonium hydroxide (NH_4OH) and hydrogen peroxide (H_2O_2) solution in a volumetric ratio of 5:1:1 for 30 minutes and heated to 75 °C. After RCA-1, samples are rinsed with MQ water and sonicated for 5 minutes in ethanol (99.5%) if self-assembled monolayers are to be assembled afterwards.

Piranha sample cleaning protocol - only SPR sample surfaces are cleaned with this method due to the fact that the chromium adherent layer for nanowells dissolves in this leaving the gold film and silica detached from one another. Nevertheless, the solution of sulfuric acid (H_2SO_4) and H_2O_2 is mixed in ratio of 3:1 and sample is placed inside for 30 minutes. **Take note!** Piranha solution is foaming vigorously when in contact with organic material, therefore the solution should be handled with extra care.

Alumina layer removal - Newly produced nanowell surfaces are placed in 10 mM NaOH solution for 1 hour and rinsed with MQ water before cleaning with RCA-1 method.

3.2.3 Molecular sieve drying

Molecular sieves have been used in order to keep methanol for ARGET-ATRP reaction dry.

1. Vacuum (at ∼100-200 mBar) dry the 3A molecular sieves overnight at 300 °C.
2. Place dried molecular sieves in a vacuumed desicator until further use.

3.2.4 Self-assembled monolayer (SAM) assembly

1. Place samples in 1.5 mM TBU or DTBU in ethanol (99.7%) solutions overnight.
2. Sonicate the samples, which are put in a beaker with 99.5% ethanol, in a sonication bath (35 kHz) for 1 minute after self-assembling the monolayers.

3.2.5 ARGET-ATRP polymerization of PNIPAM polymer brushes

ATRP polymerization of PNIPAM polymer brushes was followed according to the ARGET-ATRP schematic described in section 2.2.4. The final reagent concentrations are as listed below:

Table 3.1: Chemicals utilized in ARGET-ATRP reaction and their molar concentrations.

Chemical	Molar concentration, M
N-isopropylacrylamide	0.48
N, N, N′, N″, N″-Pentamethyldiethylenetriamine	0.0064
Ascorbic acid	0.010
$CuBr_2$	0.0006

The solvent mixtures of Methanol and MQ water were varied. However, the final reaction mixture volume is always kept at 49 milliliters.

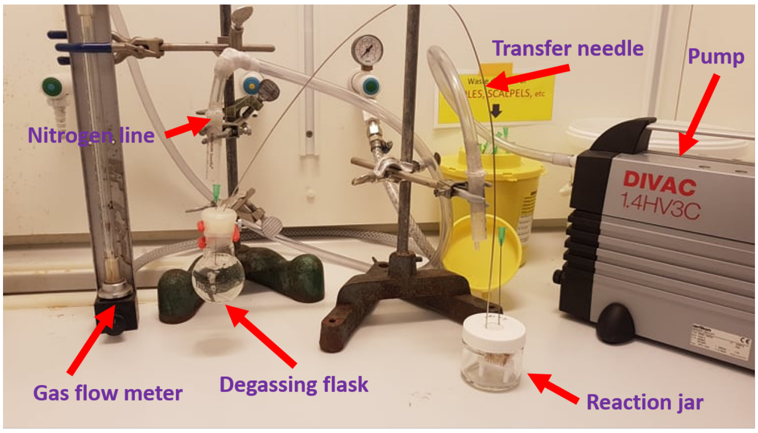

Figure 3.2: Setup for ARGET-ATRP polymerization of PNIPAM under non-glove box conditions.

In addition, the reaction is run in a common laboratory fume hood and not in the glove box, as usually employed, therefore extra care in order to avoid oxygen during the reaction is needed (to avoid possible chain termination). The whole setup may be seen in figure 3.2.

The reaction procedure is as follows:

1. Weigh the chemicals to the exact amounts either straight into the degassing flasks or, in the case of $CuBr_2$, on the anti-electrostatic weighing paper.
2. When appropriate dried and filtered through 0.2 μm syringe filter methanol, and water volume mixtures are selected, transfer them into the flask, containing $CuBr_2$, N-isopropylacrylamide (NIPAM) and N, N, N′, N″, N″-Pentamethyldiethylenetriamine (PMDETA). A rubber septum is put on top of this flask in order to prevent ambient oxygen from coming in during the degassing procedure.

3. Degas with nitrogen gas for 30 minutes at a flow rate of 560 mL/min (at height of ~3 cm; gas flow meter calibrated with Agilent ADM flow meter; see fig.3.3) by piercing the rubber septum with a needle attached to the nitrogen gas line.
4. 10 minutes before finishing degassing, attach a metal transfer needle between the flask containing the chemical mixture and a reaction jar with sample surfaces placed on a teflon holder inside the jar.
5. 5 minutes before degassing procedure is finished and transferring of the solution is started, inject 1 mL of ascorbic acid, dissolved in milliQ water in order to mix it with the rest of the solution and degas it as well. Also, attach a membrane pump and start it without transferring the solution (up to date protocol includes non-degassed ascorbic acid solution being injected straight into the polymerization solution with the sample surfaces).
6. When degassing is done, lift up the nitrogen degassing needle and lower down the metal transfer needle into the solution in order to transfer the solution into the reaction jar and initiate the reaction. (Note! The jar is sealed not only by a cap, but also with additional parafilm layer around the cap)
7. Run the reaction for the desired amount of time and finish it by opening up the jar and placing the samples into 99.7% ethanol.

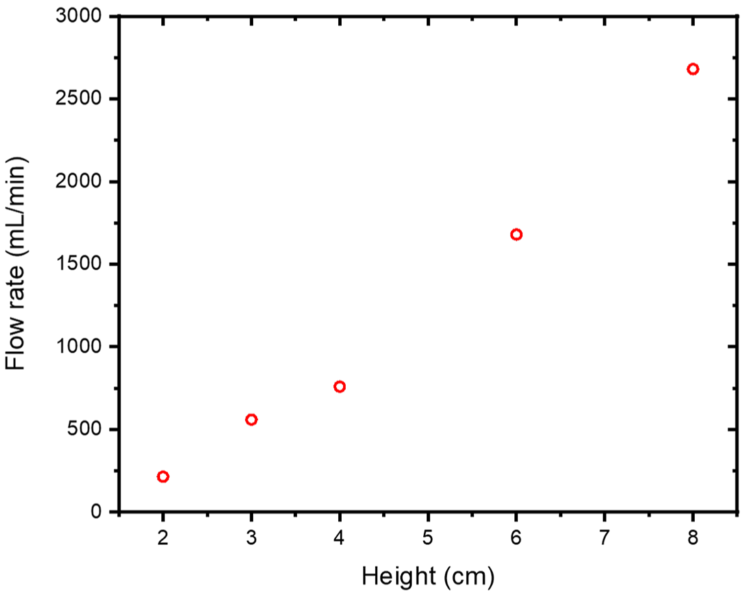

Figure 3.3: The utilized gas flow meter during the reaction process has "height levels", which corresponds to a certain nitrogen flow rate according to the calibration curve.

After the reaction, samples are placed in covered sample holders for further experiments.

3.2.6 Fluorescence microscopy experiments

Fluorescence experiments have been performed by using the flow cell (see fig. 3.9; see Appendix C) and an optical Axio Observer microscope equipped with Andor IXon Life and Axiocam cameras. Protein used for gating experiment was FITC-BSA, therefore the illumination was achieved by using 90-HE LED filter set with an excitation beam splitter (reflects and transmits light with 452 - 486 nm and 500 - 528 nm wavelengths, accordingly) and emission filter (501-527 nm) as seen in figure 3.4, where 475 nm LED light is transmitted through.

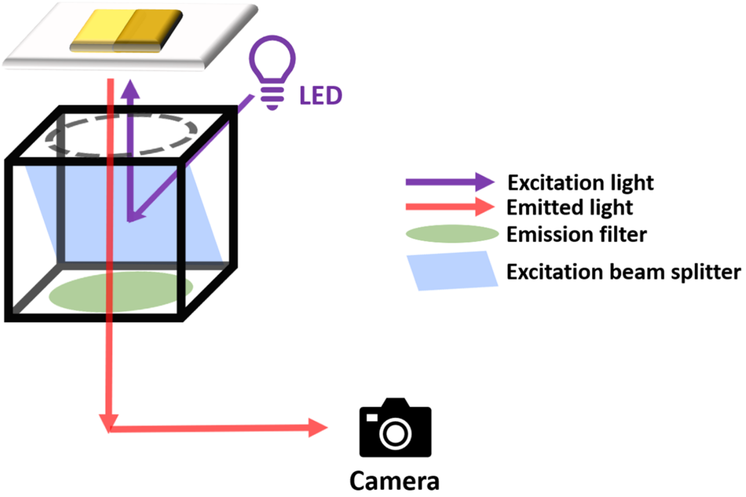

Figure 3.4: Sample illumination pathway during fluorescence microscopy measurements.

The excitation and emission peak maximums of FITC are at wavelengths of 495 and 519 nm [128] (fig. 3.5), accordingly. The dye is excited with 475 nm wavelength LED light, which is reflected from the beamsplitter onto the sample surface and the emitted light is detected with an appropriate camera as seen in fig. 3.4.

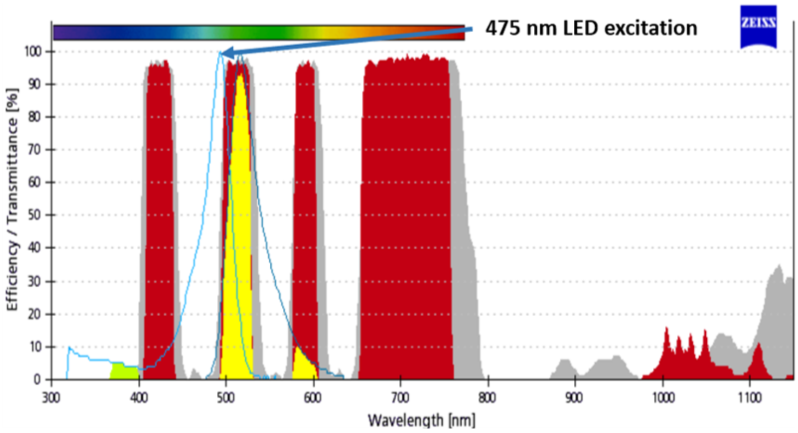

Figure 3.5: Illumination efficiency parameters for FITC-BSA as taken from Zeiss website [129].

Functionalized sample surfaces have been manufactured in such a way that half of the sample would be plain gold and the other side would contain nanowells as seen in fig. 3.6. All of the pictures have been taken with 50 x air objective even though the nanowell/gold side of the surface is still exposed to a solution.

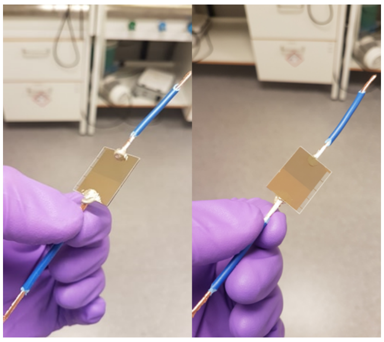

Figure 3.6: Sample surface having bare plain gold (reference; bottom) and nanowell sides (top; darker color) with copper wires glued on in order to initiate local surface heating on demand. Nanowell/gold side can be seen in the right side of the figure and silica side is on the left.

The fluorescence intensity ratio between gold and nanowell sides (fluorescence intensity data is gathered from gold and nanowell side separately as demonstrated in fig. 3.7) with subtracted background light is presented in data figures according to this equation:

$$\frac{I_{(NWs)} - I_{(Back.)}}{I_{(Gold)} - I_{(Back.)}} \tag{3.1}$$

Where $I_{(NWs)}$, $I_{(Gold)}$ and $I_{(Back.)}$ are fluorescence intensities of nanowell and gold region, and background light. The reason why such an expression is used instead of just subtracting the $I_{(Gold)}$ from $I_{(NWs)}$ straightforwardly, is because the transmission through nanowells should be higher than through gold surface without holes at and below 500 nm wavelength [116]. The background fluorescence intensity is subtracted by taking an image with the Andor camera with the same camera parameters (e.g. exposure time) as used in the experiments, just without LED illumination. Then a matlab program is run (can be found in https://pastebin.com/MvDPnvr4, password: 0NN4E1xPPG). Data files extracted from the zen software (ZVI types) are converted to time stack image files (TIFF) and processed with the matlab code.

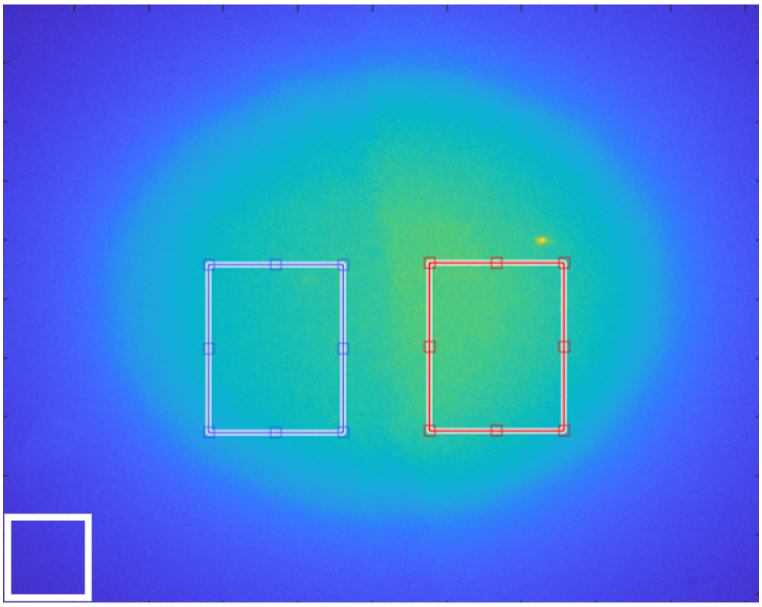

Figure 3.7: 45v%MQPNIPAM polymer brush (reaction time: 30 minutes) functionalized half-half sample surface. Two spots are selected - on gold (blue square) and nanowell (red square) side, and fluorescence intensity is extracted with matlab code. The white hollow square indicates a region, where the background intensity data is collected from.

3.2.7 Extinction spectroscopy experiments

Extinction spectroscopy include running buffers, which are the same as in other experiments : 1x phosphate buffered saline (PBS;

10 mM phosphate, 137 mM NaCl and 2.7 mM KCl) and 1x borate buffered saline (BBS; 10 mM borate and 150 mM NaCl) with varying pH values depending on the experiment.

The lamp a and spectrometer for visible/near-infrared light employed for the spectroscopic real-time measurements are B&WTek BPS2.0 and Cypher^{TM} H (B&WTek), respectively. Extinction spectroscopy experiments included a flow cell (XNano) manufactured by Insplorion, otherwise, custom made flow cells were utilized (fig. 3.8 and 3.9; blueprints for the flow cell made for microscopy experiments can be found in Appendix C). Insplorion setup also includes its own temperature control unit, where the desired temperature may bet set. In other optical setups, in order to generate local temperature increase by resistive heating, Gamry potentiostat interface 1000 was employed by applying voltage on the isolated copper wires, which are glued to the sample surface with conductive glue.

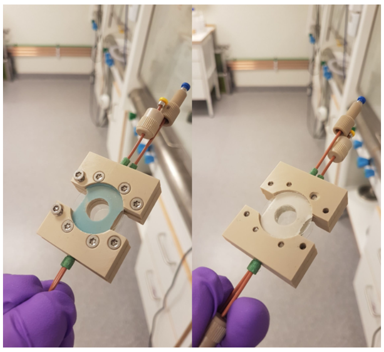

Figure 3.8: A flow cell, which was utilized for plasmonic shift measurements before developing a flow cell, which fits the microscope optical measurements as well.

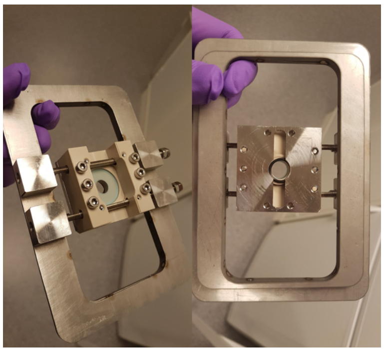

Figure 3.9: A flow cell, which is utilized in plasmonic shift and fluorescence measurements.

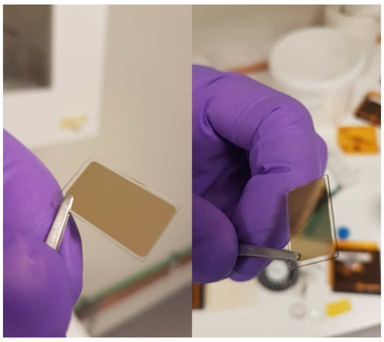

Figure 3.10: Three layered SPR sensor chip, used in SPR experiments. Gold side up (top), silica side at the bottom (bottom).

3.2.8 Surface plasmon resonance experiments

SPR experiments were conducted by utilizing planar SPR sensor chips, having gold (50 nm in thickness), chromium (the adhesion layer between gold and silicon dioxide layers) and silicon dioxide (as a support layers) (fig. 3.10).

SPR Navi^{TM} 220A instrument (BioNavis) is equipped with three lasers (785 nm, 670 nm and 980 nm), which induce different decay lengths of sensing fields. The SPR spectra scans are taken on 2 flow channels, which are exposed to the same chip, but different spots. Consequently, giving the possibility to estimate how homogenous the film of interest is.

For experiments, which include flow through the channels, a stable baseline is established with a buffer of interest (e.g. 1x PBS). The film thickness measurements using 35 kDa PEG (20 g/L) are conducted at 50 μL/min flow rate unless the temperature increase is necessary. In this case, the flow rate is reduced to 10 μL/min. In parallel (e.g. 35 kDa PEG is injected in both flow channels at the same time) mode injections were made for 10 minutes, with a 10 minute rinse with the running buffer in between each injection. An injection profile of bulk liquid SPR response, showing that 35 kDa PEG does not irreversibly adsorb onto, e.g. PNIPAM polymer brushes, was verified (the TIR and SPR angles after the injection of 35 kDa PEG probe have returned to the baseline values) after before applying the data to calculate brush height.

The height determination follows a procedure, which employs Fresnel coefficients in order to fit SPR spectra and retrieve possible film heights, which correspond to respective refractive indexes. This method has been described previously [33] and a MATLAB script has been developed in order to facilitate the calculations (**Can be found via weblink:** https://pastebin.com/M0Sw3QE3; Password: QfdZrft836)

3.2.9 Quartz Crystal Microbalance with Dissipation Monitoring experiments

Measurements were performed using a Q-Sense E4 instrument (Biolin Scientific) equipped with a peristaltic pump (Ismatec). Gold or silica sensors (fig. 3.11; bare or functionalized with PNIPAM polymer brushes) were mounted into one of the 4 available flow cells and rinsed with running buffer (e.g. 1x PBS) until a stable baseline is achieved. The setup can be seen in figure 3.12. QCM-D experiment data is collected over 6 overtones (e.g. 1st, 3d, 5th, etc.), but commonly, only the 3d and the 5th overtones are extracted for further processing. Cleaning procedure of QCM-D flow cells: run at least 10 mL of 2w%SDS and 25 mL of MQ water once the experiment is finished. Dry the flow cell with nitrogen afterwards.

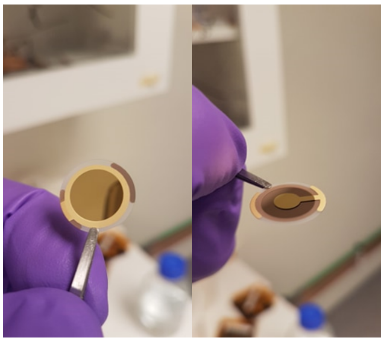

Figure 3.11: QCM-D crystal sensor with deposited gold electrodes on one side (left) and gold layer on the sensing side (right).

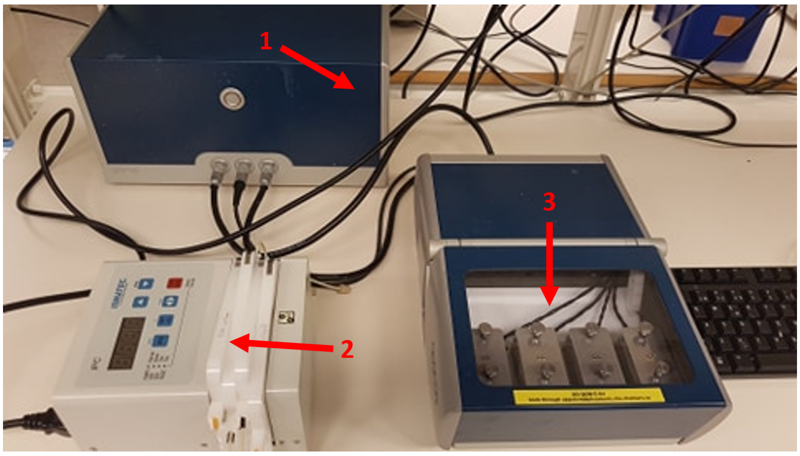

Figure 3.12: Common QCM-D setup. 1 - q-sense analyzer, 2 - peristaltic pump, 3 - a sensing chamber with 4 flow cells.

Results and discussion 4

4.1 DTBU SAM and PNIPAM polymer brush molecular footprints

Before functionalizing nanowell structures with PNIPAM polymer brushes for protein non-covalent entrapment and release application, the initial phase of surface self-assembled monolayer (SAM) had to be shown. Therefore, Fourier-Transform Infrared Spectroscopy in reflection mode (FTIR-RAS; the *T* in *y axis* in fig. 4.1 is reflection, but taken as transmission from the software) was employed (fig. 4.1 a)) in order to indicate the molecular footprint of C-Br (expected at 515 - 690 cm^{-1}) for two simultaneously functionalized SPR sample surfaces. The strong Peak at 668 cm^{-1} indicates C-Br bond stretching.

Also, a QCM-D experiment was performed, where the SAM was prepared in absolute ethanol (99.7%). After re-introducing ethanol at ~10000 s the frequency shift decreased roughly by 0.5 Hz and then continued to decrease over the rest of the experiment, which could mean that the SAM has not reached an equilibrium state yet or the shift is just due to drifting baseline over time. Nevertheless, it seems that the assembly takes much longer than the experimented time to fully assemble (the frequency shift was still decreasing after ∼ 4000 s; fig. 4.1 b)), therefore at least 18 hours have been chosen in order to obtain the needed SAM layer as previously reported [19].

FTIR-RAS spectra were taken also for PNIPAM polymer brush functionalized SPR surfaces (fig. 4.2). Polymerization times vary from 5 to 15 minutes and spectra were taken of two SPR sample surfaces belonging to the same polymerization batch. In addition, the polymerization was performed with 50/50v% MQ water/-methanol in the solvent mixture also as suggested by Emilsson et al. [19].

The spectra indicate the amide C=O stretch (1659 cm^{-1}), N-H bend (1553 cm^{-1}) and also the CH-stretching region 2800-3000 cm^{-1}. The doublet at 1368 and 1388 cm^{-1} is attributed to isopropyl moiety. The 3300 cm^{-1} peak is attributed to N-H stretch. The identified peaks (same positions as Beattie et al. have also seen [130]) confirm the presence of PNIPAM on the SPR sample surfaces and the peak area increases (indicating thicker polymer brushes) with polymerization

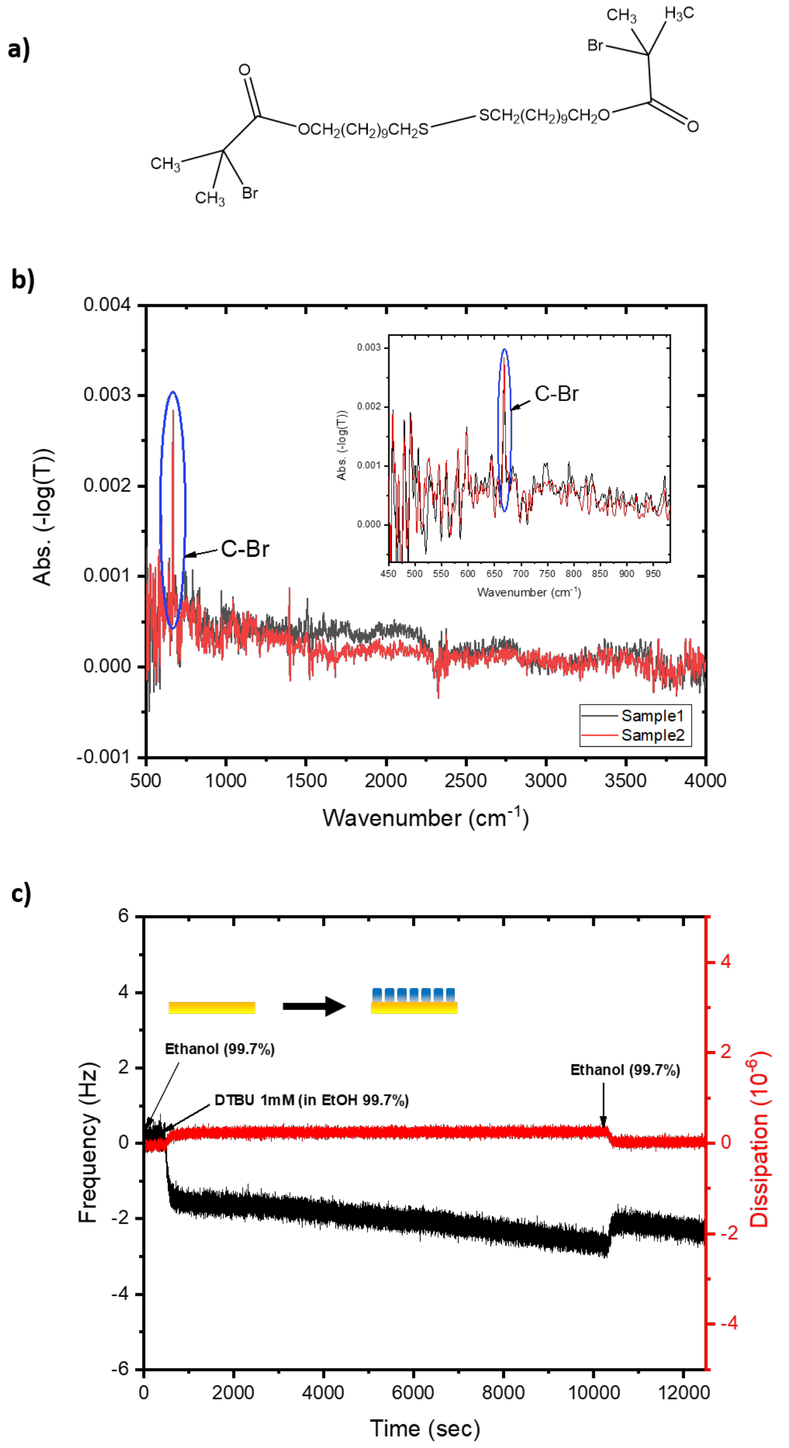

Figure 4.1: a) Molecule of Bis[2-(2-bromoisobutyryloxy)undecyl] disulfide (DTBU) b) FTIR-RAS spectrum of two simultaneously prepared SPR sample surfaces, which are functionalized with DTBU SAMs. The strong Peak at 668 cm^{-1} indicates C-Br bond stretching. Received reflection data (shown as *"T"* in the figures as taken from the software) has been converted into absorption according to the formula in the *y axis*. c) DTBU SAM being functionalized on a gold coated QCM-D chip in real-time. The spectra were offset at 2700 cm^{-1} to have 0 absorbance.

time. More FTIR-RAS spectra for different polymerization times and v% MQ/MeOH solvent mixtures may be found in Appendix B.

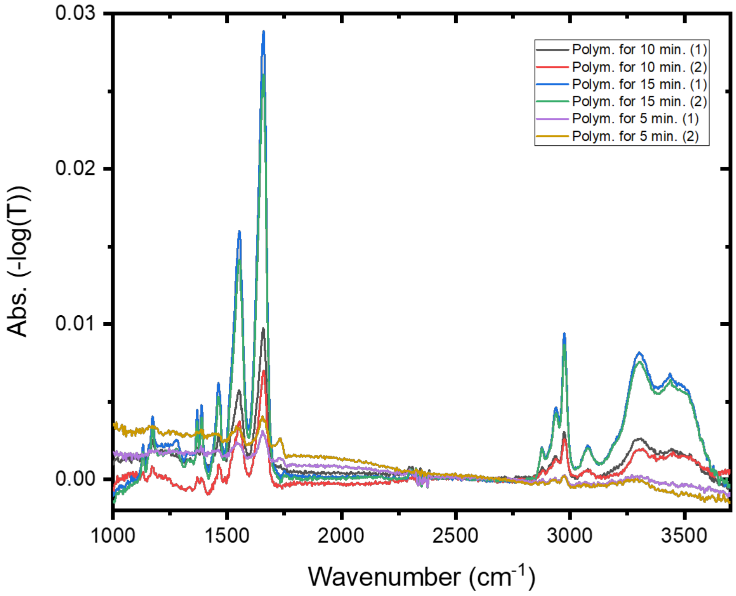

Figure 4.2: FTIR-RAS spectra of PNIPAM polymer brush (50/50*v*% MQ/MeOH solvent mixture) functionalized SPR sample surfaces, where numbers 1 and 2 in the legend indicate two samples from the same polymerization batch. Polymerization times vary from 5 - 15 minutes. All spectra were offset to have 0 absorbance at 2700 cm^{-1}.

4.2 PNIPAM polymer brush thermo-responsive behavior

After determining DTBU SAM layer and PNIPAM polymer brush formation, it was necessary to see if the conformational change above and below LCST is reversible in order to utilize the functionalized surface for latter gating experiments. Therefore, as can be seen in figure 4.3, it was determined that switching from room temperature to above LCST temperature of PNIPAM (in this case 35 °C) makes the brushes switch from an extended state into a globule form reversibly without inducing any chemical change. This could be monitored by the change in the refractive index, which is directly related to the SPR angle.

After a few months of polymerizing PNIPAM polymer brushes, which are grafted-from the DTBU assembly, it was noticed in the FTIR spectra (fig. 4.4), that the PNIPAM molecular footprint is not evident anymore. Occasionally, no polymer was detected with FTIR, suggesting that the initiator SAM did not form. Without investigating further, we attributed this to a known possibility of disulfide oxidation [131] over time and/or bromide moiety [132], which is a main factor leading for the initiation of a radical polymerization, leaving the carbon chain of DTBU. To avoid reoccurring problems with the DTBU SAM layer, a new chemical was purchased every 2 months and no more failed reaction initiations were noticed.

Furthermore, PNIPAM polymer brush layer, polymerized in the

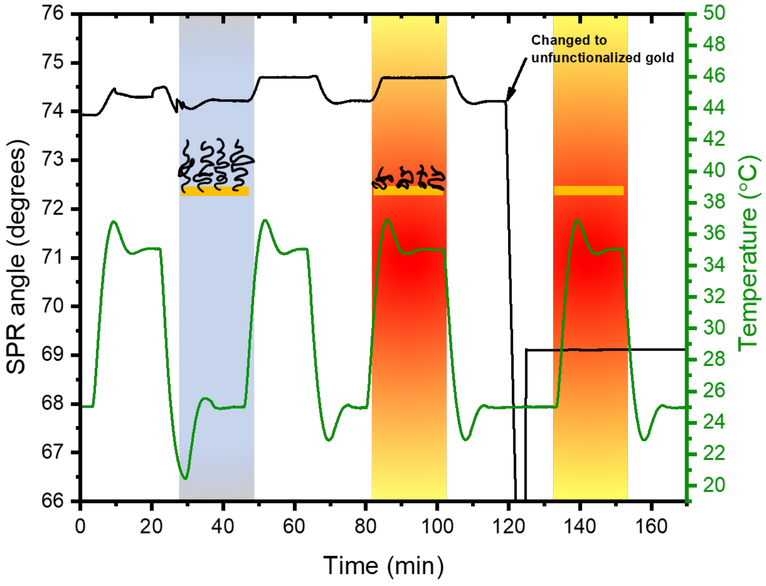

Figure 4.3: SPR angular sensogram, indicating reversible 50/50*v*% MQ water/MeOH PNIPAM polymer brush (reaction time - 10 minutes) conformational change from "swollen" (at room temperature; indicated by the blue colour) to "collapsed" brushes by increasing the temperature to 35 °C (red colour).

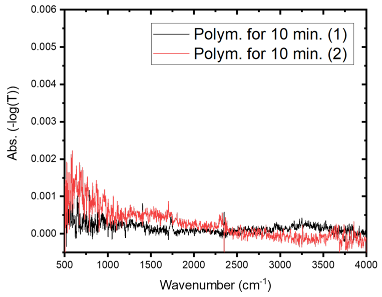

Figure 4.4: FTIR spectra, indicating one batch (50/50*v*% MQ water/MeOH; 10 minutes) of a few PNIPAM polymer brush functionalized SPR sample surfaces, that did not contain PNIPAM polymer brushes. The baseline shift is attributed to the re-use of the SPR sample surface for sample 2. Spectra are offset at 2500 cm^{-1}.

50/50 (*v*/*v*%) MQ/MeOH solvent mixture and for 15 minutes, was probed with a model protein BSA under physiological pH in both - extended and collapsed state (fig. 4.5), in order to see if the protein is not interacting with the brush layer itself and can be indeed monitored in the gating/entrapment process. Indeed, upon injecting BSA in the swollen (0 - 50 min) and the collapsed brush regime (50 - 100 min) it can be seen that the SPR angles are returning to the values before the injections, meaning that the protein either is adsorbing reversibly or the shift in SPR angle comes from the bulk refractive index change.

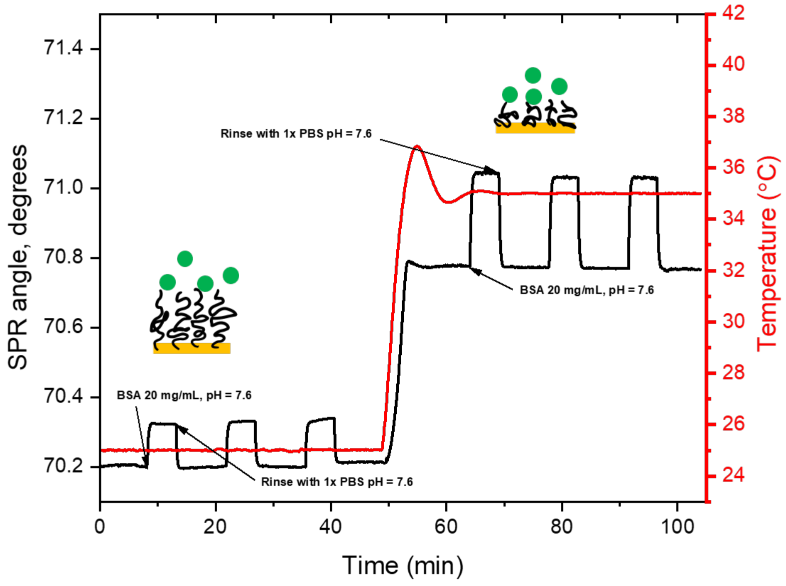

Figure 4.5: SPR angular sensogram, showing SPR angle response from the BSA solution, but no adsorption on 50/50*v*% MQ water/MeOH PNIPAM polymer brush film, polymerized for 15 minutes both at the extended/swollen and collapsed states at physiological pH.

4.3 BSA adsorption/desorption on silica and transportation through PEG polymer brush functionalized nanowells

To begin with, it was necessary to determine whether it is possible to electrostatically adsorb BSA in the nanowell interior without additionally getting it irreversibly bound to the gold surface, which would make it denaturate [133, 134]. Also, to measure if the electrostatically adsorbed BSA on silica could be be removed from the nanowells by increasing the pH of the bulk solution (e.g. change the surface charge of the protein, so it is the same as the surface charge of the silica and thus repelled). All of this may be done by taking advantage of the protein's isoelectric point (IEP), which is in the range of pH = 4.5 to 5.4 [135–137] and fused silica's negative surface charge when pH is above 2 [135, 138]. The pH, that was employed in the experiments to electrostatically adsorb BSA was 5.5, due to the fact, that, as reported in the literature [135, 137], there is a residence time of the protein at the fused silica surface even if the surface net charge is slightly negative and also in order to avoid possible aggregation at low pH [135, 137, 139]. It was also thought, that the protein will desorb easier later on, when pH is increased compared to trying to desorb it below physiological pH. It is important to mention, that if the pH is below 11, the protein should avoid aggregation and retain its native structure [140].

BSA adsorption on bare silica QCM-D sensor can be seen in fig. 4.6 (an experiment conducted by Zeynep Adali; unpublished results), where it adsorbs on the SiO_2 bare surface at pH = 5.5 and fully desorbs at pH = 8.5 (1x PBS) as seen from the frequency shift returning back to the baseline at $\sim$ 130 minutes.

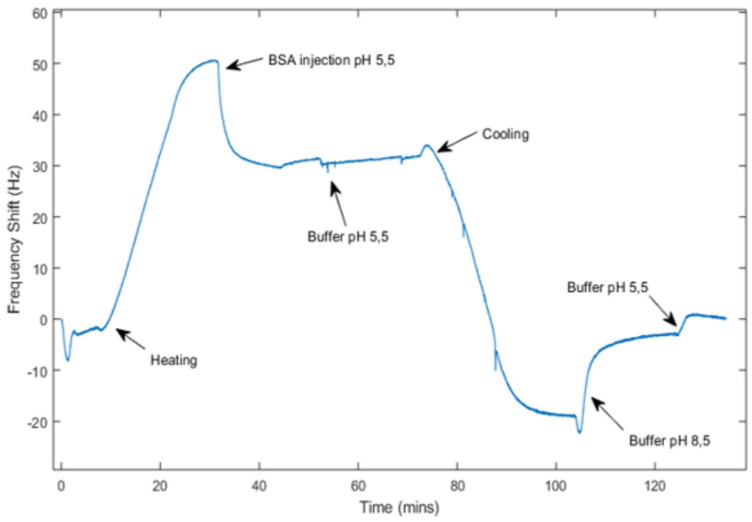

Figure 4.6: QCM-D experiment of BSA adsorption on silica surface at pH = 5.5 and desorption at pH = 8.5.

The same is observed with FITC-BSA, where the protein adsorbs at pH = 5.5 and is completely desorbed at pH = 8.5 as seen in figure 4.7.

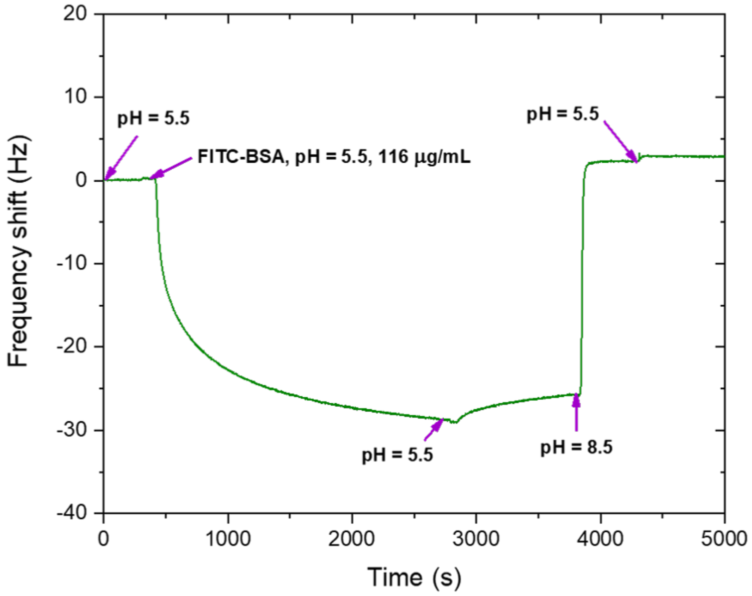

Figure 4.7: QCM-D experiment of FITC-BSA adsorption on silica surface at pH = 5.5 and desorption at pH = 8.5.

Moreover, a passivation layer of 2 kDa mPEG-SH on the gold surface was chosen, which is supposed to have short enough brushes of ∼ 6-10 nm in the swollen state [141], let BSA diffuse into nanowells and also not allow it to adsorb on the gold surface. In fact, this can be seen in figure 4.8. The pH during protein binding was kept at 5.5 with 1x PBS buffer, however, in order to desorb them and reach a pH = 8.0 or higher, 1x borate buffer saline (BBS) was utilized. According to the shift of "Peak", which is 0.647 nm (not to be confused with non-specific adsorption on the gold surface, because reversible desorption is observed), and "Dip" plasmonic shift (at least twice as big as the "Peak" shift, (1.381 nm)) BSA adsorbed inside the nanowells similarly how Emilsson et al., observed [142]. The proteins were subsequently desorbed by making their net charge negative at ∼ 8900 seconds.

As a complementary test to BSA protein gating, another model protein neutravidin (NA; same 50 μg/mL concentration in the experiments) was chosen in order to see if the adsorption tendencies are similar. The IEP of NA is ∼6.3 [143], but the running buffer pH was kept the same as in the case with BSA for electrostatic adsorption and desorption of NA inside the nanowells due to the fact that the adsorption of NA takes approximately the same amount of time as will be seen in the latter experiments. The control experiment with 2 kDa mPEG-SH passivation layer and NA can be seen in figure 4.9. The adsorbed amount of NA in terms of "Peak" and "Dip" plasmonic shifts are ∼0.4 nm and ∼2 nm over ∼4600 seconds, accordingly. After the increase of pH to 8.0, the remaining plasmonic shifts from the adsorbed NA were 0.164 nm for "Peak" and 1.34 nm for "Dip". It seems that NA takes much

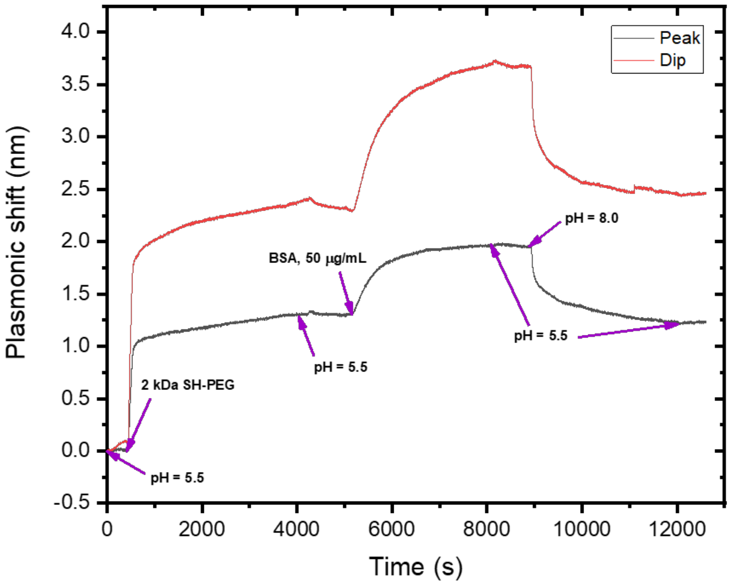

Figure 4.8: A Plasmonic shift real-time experiment showing BSA protein adsorption inside the nanowells, which is reversible with pH, and on the 2 kDa mPEG-SH functionalized surface by changing pH from 5.5 to 8.0.

longer to adsorb and desorb from the inside of nanowells and, in this case, full desorption was not achieved. The reason for slow adsorption/desorption could be that NA has a higher IEP, the net charge is less negative at pH = 8.0 and more positive at pH = 5.5 than in the case with BSA, leading to weaker electrostatic repulsion. Alternatively, the polymer brush passivation layer had lower than sufficient grafting density to prevent non-specific NA binding to gold, possibly also leading to its denaturation.

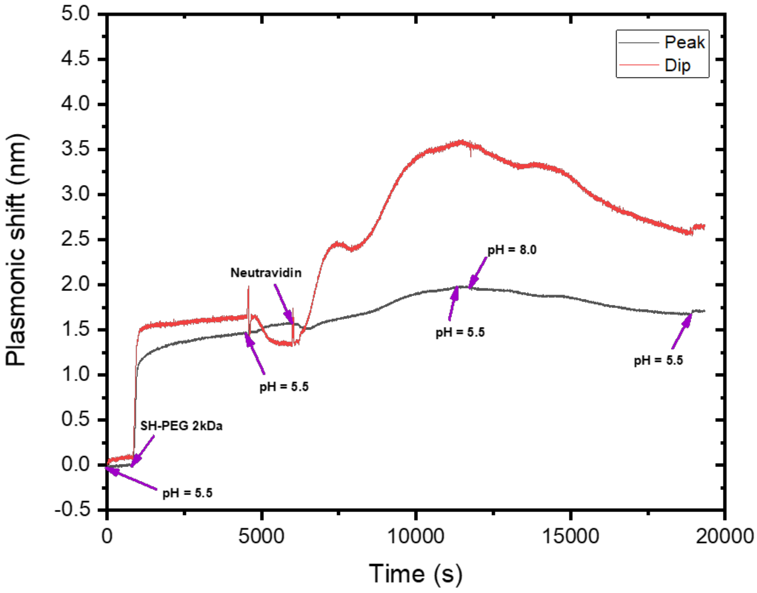

Figure 4.9: NA protein adsorption/desorption from the inside of the nanowells and on their 2 kDa mPEG-SH functionalized surface by changing pH from 5.5 to 8.0.

In the next section, protein gating real-time plasmonic shift/extinction experiments with PNIPAM polymer brush functionalized nanowells will be discussed and overviewed.

4.4 Real-time plasmonic shift DTBU initiated PNIPAM polymer brush nanostructure gating experiments for BSA and NA transportation

In order to see if PNIPAM polymer brushes are efficient entropic barriers for proteins, one has to think about two main factors - optimal polymer brush extended/collapsed height and their grafting density. Optimal extended/collapsed PNIPAM polymer brush height will allow to tailor the gating mechanism for protein translocation. For example, if the nanowell diameter is on the range of 80-90 nm (fig. 1.1) and the extended polymer brush height is enough to close this diameter, but keep it open in the collapsed state (fig. 4.10), so the proteins can go through, then one has achieved the optimal height for the gating system. In addition, having high enough grafting density is necessary, because proteins tend to fall into different adsorption modes, as discussed earlier in the section 2.2.5. This could lead to possible protein adsorption and denaturation on the gold surface. Nevertheless, if the polymer brushes are hydrated enough, due to osmotic pressure build-up within the brush layer, proteins will be repelled from adsorbing on the gold or on the brushes [94].

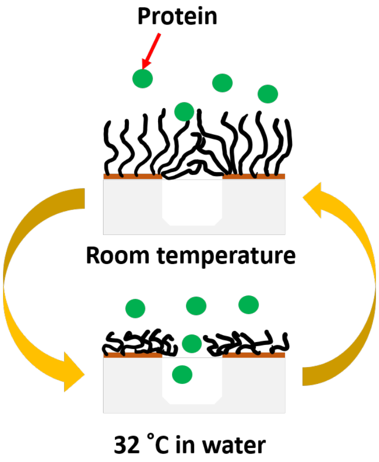

Figure 4.10: PNIPAM polymer brush functionalized nanostructure gating mechanism for proteins.

Due to the fact that in this case PNIPAM polymer brushes are grown by employing a grafting-from technique, there is no direct way of determining the molecular weight or grafting density of the film without being able to cleave polymer brushes from the substrate and achieving a sufficiently high amount (~0.1-0.15 w/v% of injected 100 μL according to Waters guide [144]) detectable with, e.g. gas permeation chromatography. For example, if one would take an educated guess and assume polymer brushes with 20 kDa molecular weight (polymer brush extended height in the range of 40-50 nm [141]), having a high grafting density of ~1 chain/nm^2 and a sample surface of 18x24 mm, then the cleaved of amount of polymer brushes would be ~14.4 μg (or ~0.2 μg with the grafting density presented by Emilsson et al. [141]). Due to these limitations, only dry, swollen and collapsed polymer brush heights were determined by employing the non-interactive probe technique mentioned earlier in section 2.1.3. Nevertheless, it is important to mention, that an approximate polymer brush extended/collapsed thickness may be determined from analytical calculations (illustrative representation can be seen in fig. 4.11) taking into account the surface plasmon sensitivity S_0, plasmonic field decay length δ, film thickness d, changes in bulk and film refractive indexes Δn, and plasmonic shift $\Delta\lambda$ [117]:

$$\Delta\lambda = S_0 \Delta n (1 - \exp(-d/\delta)) \tag{4.1}$$

This equation may be further extended in order to determine the collapsed (H_{col}) and swollen/extended (H_{ext}) height of the polymer brush:

$$(\lambda_{col} - \lambda_{ext})/S_0 = n_{col} - n_{ext} + \Delta n_{ext} e^{(-H_{ext}/\delta)} - \Delta n_{col} e^{(-H_{col}/\delta)} \tag{4.2}$$

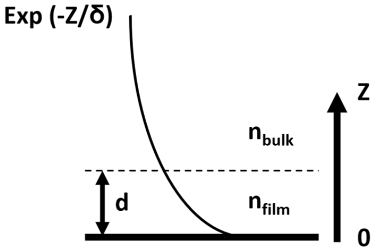

Figure 4.11: An illustration representing how plasmonic field decay length δ decreases when going perpendicularly away from the film towards the bulk solution.

Where Δn_{ext} and Δn_{col} are differences between bulk refractive index and the polymer brush film in extended or collapsed conformation, respectively. Also, in this case, H_{col}, H_{ext} and the refractive indexes of the film are unknown components. The sensitivity factor was reported to be ~147 nm per RI unit [14] (how much plasmon resonance shifts per liquid bulk refractive index unit) and the decay length ~50 nm [117] for 80 - 90 nm nanowells.

Even though molecular masses of the PNIPAM polymer brush layers were not characterized, the protein permeation through the nanowells was measured by real-time plasmonic shift and fluorescence measurements in order to directly evaluate if the brush layer is dense and thick enough.

The general PNIPAM polymer brush functionalized nanowell gating experimentation scheme can be seen in fig. 4.12. This procedure was followed in most of the following experiments unless stated otherwise:

1. PNIPAM polymer brush functionalized nanowells are exposed to below physiological pH (pH = 5.5).
2. Protein solution in the same pH as in step 1. is injected. If the polymer brush swollen height is thick enough to close the pores, the proteins will be blocked from entering the nanowells.
3. Protein solution is rinsed away with the running buffer (pH = 5.5).
4. PNIPAM polymer brushes are collapsed by exposing them to a temperature above their LCST.
5. Proteins are injected again in order to electrostatically bind them inside the nanowells due to the fact, that the pores should be open if the collapsed brushes become small enough to leave an entrance.

6. Rinsing with the running buffer (e.g. pH = 5.5).
7. Return to a temperature, which is below PNIPAM polymer brush LCST.
8. Increase the pH of the running buffer to at least pH = 8.0 in order to see if the proteins are trapped or are leaving the nanowells (i.e. desorbing from silica inside the nanowells as seen in fig. 4.8) according to the change of their net charge becoming the same as the surface charge of silica.
9. Collapse the polymer brushes again by increasing the temperature to above their LCST in order to release trapped proteins, if any.

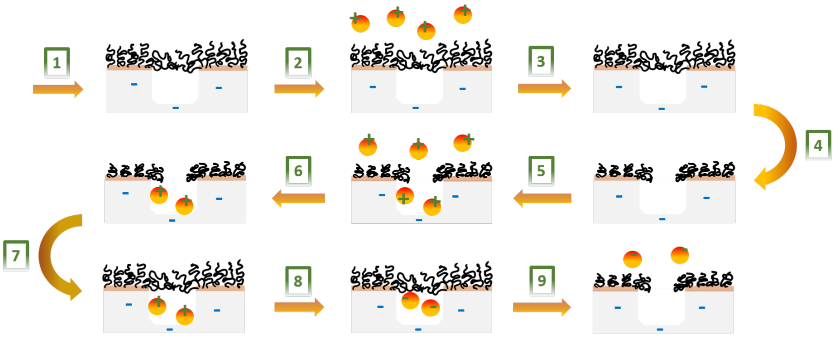

Figure 4.12: A planned protein trapping and release protocol through PNIPAM polymer brush functionalized nanostructures.

One of the first BSA gating experiments was done with 50v%MQ PNIPAM polymer brushes, polymerized for 10 minutes, and can be seen in fig. 4.13. One can notice, that the "Peak" and "Dip" plasmonic shifts are ~2-3 times smaller compared to the control experiment (fig. 4.8), meaning that either only a small fraction of PNIPAM functionalized nanowells let the BSA translocate through or, in contrast to adsorption at physiological pH (4.5), some proteins have bound to the collapsed brush at pH = 5.5. Instead of utilizing 1x pH = 8.0 BBS to desorb BSA from the nanowell interior, close to physiological pH was used, but evidently the selected 1x pH = 7.4 PBS was not high enough in order to desorb the electrostatically bound protein. This can be observed from the plasmonic shift after the increase of pH at ~16500 seconds (or step 8 in the gating procedure listed above), which did not cause a return to the baseline level. An alternative explanation is that the polymer brushes may be assumed to be too thick even in the collapsed state, because the expected plasmonic shift from BSA translocation is ~0.5-0.7 for "Peak" and ~1.3-2.6 for "Dip" as reported by Emilsson et al. [142] and seen in other plasmonic shifts during BSA adsorption indicated in Appendix D.

After a few successful 50v%MQPNIPAM polymer brush syntheses, it was noticed by visual observation, that the brush layers have patches, i.e. the thickness was not uniform on the sample surface. A few reasons for this could be - a poorly formed DTBU initiator

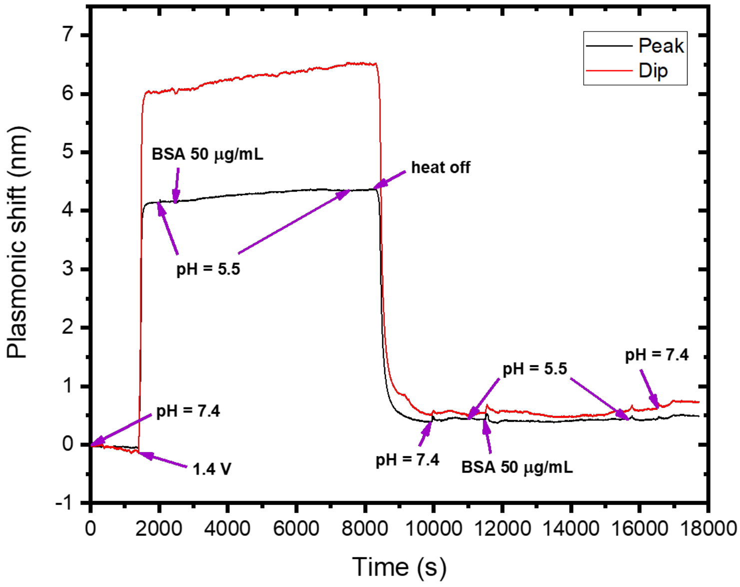

Figure 4.13: One of the first attempts to trap and release BSA protein (concentration is kept the same in all experiments unless stated otherwise) upon varying its net charge by changing the pH from 5.5 to 7.4 (1x PBS) with 50*v*%MQ water MQPNIPAM polymer brush functionalized nanowells (reaction time: 10 min.).

layer (parts of the surface do not have polymer brushes) or because the polymerization reaction is happening rapidly, some chains are growing faster than others (e.g. by sterically blocking other chain growth) or because of poorly formed initiator layer due to insufficient surface cleanliness, therefore blocking other chain growth sites. Therefore, it was chosen to reduce the *v*% of MQ water, which is a better solvent for PNIPAM than MeOH, and vary the polymerization time in order to attain more homogeneous polymer brushes and also reduce the thickness of the film.

Some of the PNIPAM funcitonalized nanowell gating experiments and reduced water content during polymerization may be seen in figures 4.14 and 4.15 (take note that all of the plasmonic shift experiment numerical values may be found in the (Appendix D)). Two complimentary BSA and NA gating experiments performed with DTBU initiated 45/55 (*v*%/*v*%) MQ water/MeoH solvent mixture and polymerized for 1 hour 40 minutes (fig. 4.14 and 4.15, respectively) resulted in "Peak" and "Dip" plasmonic shifts, which differ almost by double when comparing these two experiments, upon collapsing the brushes.

These two coated nanostructures in both gating experiments, contain PNIPAM polymer brushes produced with the same reaction conditions in order to monitor reproducibility, however, shows a lack of it. In the first case (fig. 4.14) the "Peak" and "Dip" polymer brush collapse shifts increased to 2.907 and 3.99 nm, accordingly. This could mean that either polymer brush layer is thicker, producing a higher "sensed" refractive index by the plasmonic field, or due to differing grafting density, have less water in their vicinity

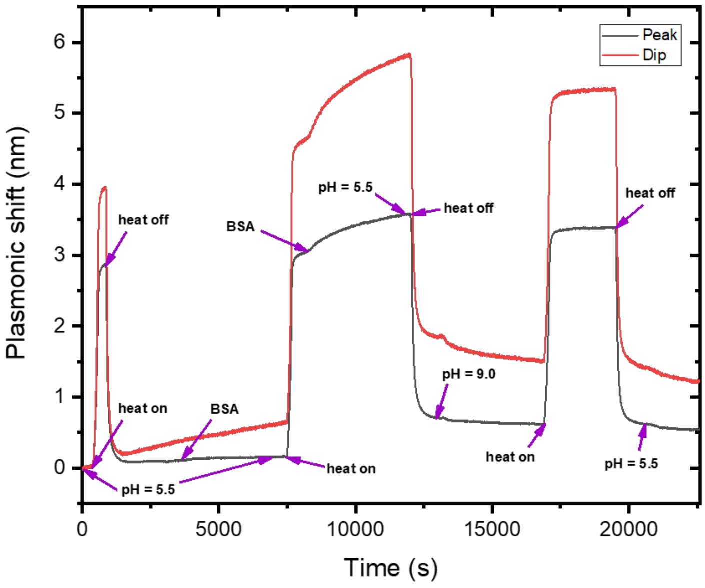

Figure 4.14: Real-time plasmonic shift BSA transport gating experiment with 45*v*%MQPNIPAM polymer brush (reaction time: 1hr. 40 min.) nanowells.

compared to experiment shown in fig. 4.15. Even though, the "Dip" shift baseline is drifting over time, it is possible to deduct from "Peak" plasmonic shift, that almost negligible amount (~ 0.042 nm over 3200 seconds) of BSA went through the swollen state PNIPAM polymer brush pores. The "Peak" and "Dip" shifts upon injecting BSA over collapsed state polymer brush nanowells are as expected when a full protein monolayer is adsorbed inside the nanowells [142], resulting in 0.505 nm and 1.152 nm. This indicates that these polymer brushes may be thick enough to block proteins from leaving when they have a negative net charge, which indeed may be seen in the experiment. However, a peculiarity upon collapsing the polymer brushes again, is observed - the plasmonic shift expected from the protein desorption is decreasing very slowly, possibly indicating protein non-specific binding to the gold surface. This might happen if not enough densely packed PNIPAM chains are allowing protein to penetrate through (as Xue et al. and Sangwook et al. have seen before [145–147]), reach the gold and adsorb, which, in turn, denatures them and leaves irreversibly bound to the surface. In addition, plasmonic shifts of "Peak" and "Dip" with values 0.341 nm and 0.517 nm are retained, respectively, which indicate the remaining adsorbed BSA. They are calculated by subtracting the change in plasmonic shift (assumed to be desorbing BSA) upon turning the protein's net charge negative (at ~13000 seconds) until the very last data point (at ~22500 seconds) of the figure from the plasmonic shift gained from adsorbing BSA at the collapsed state.

In addition, when NA transport is gated with the coated nano-

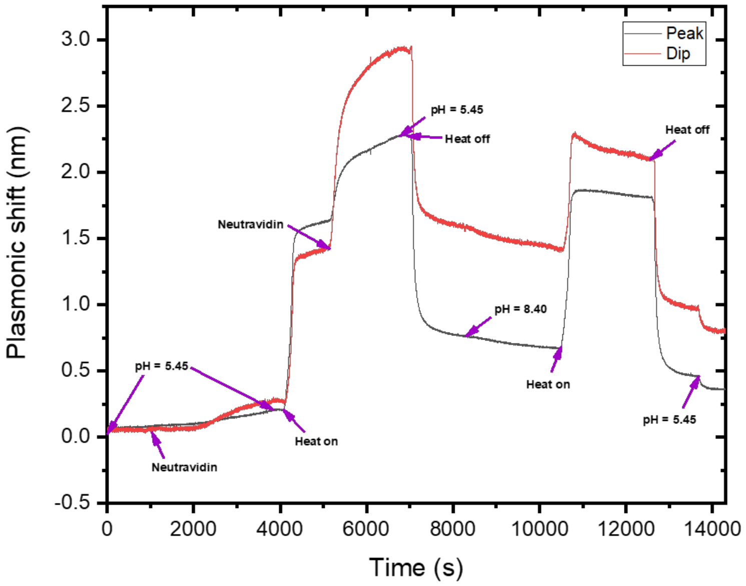

Figure 4.15: Real-time plasmonic shift NA transport gating experiment with 45v%MQPNIPAM polymer brush (reaction time: 1hr. 40 min.) nanostructures.

structures (fig. 4.15), too short PNIPAM polymer brush layer may be seen, because some (0.121 nm for "Peak" and 0.222 nm for "Dip) of the NA protein is translocating through the pores, covered by swollen state brushes, at ~3500 seconds with a relatively long induction time. Even more protein is adsorbed once the temperature is increased above polymer brush LCST (0.648 nm for "Peak" and 1.51 nm for "Dip"). The higher "Peak" plasmonic shift upon adsorption compared to the control experiment (fig. 4.9) could result from the fact, that some protein has bound to the gold surface due to, e.g. lower grafting density of the polymer brush. After NA net charge has been changed to negative, the protein was desorbing very slowly and after switching to lower pH at ~14000 seconds around 0.213 nm for "Peak" and 0.828 nm for "Dip" were left. The evident NA adsorption on the gold surface is also noticed from the higher "Peak" plasmonic shift left after increasing the pH (0.213 nm) compared to the control experiment (0.164 nm) over a shorter period of desorption time. The "Dip" plasmonic shift resulted in 0.828 nm, which is smaller than in the control experiment and can possibly be explained by the fact, that the depth of the nanowells is smaller, leading to a smaller surface area for proteins to adsorb on. In addition, because the isoelectric point of NA is higher than BSA, we cannot confirm yet that NA is completely desorbing at pH = 8.4, therefore an additional control experiment is required to confirm that.

A slight caution should be advised when comparing plasmonic shift values between different experiments, because the shifts could differ from nanowell sample surface to another due to previously mentioned effects in the section 2.3.1. In addition, as it will be shown later on, the plasmonic shifts in "Peak" and "Dip" from changing between 1x PBS pH = 5.5 to 1x BBS pH = 8.0 are 0.081 nm and 0.08 nm, respectively.

In the next section, plasmonic shift discrepancies appearing in PNIPAM polymer brush conformational change behavior between two initiators - DTBU and the thiol equivalent (TBU; an alternative initiator, which is more soluble in ethanol than DTBU and could possibly increase the grafting density of the brushes) will be overviewed.

4.5 Discrepancies in plasmonic shifts upon thermo-responsive switching between DTBU and TBU SAM initiated PNIPAM polymer brushes

It was noticed that after utilizing DTBU SAMs to initiate polymerization, PNIPAM polymer brush conformational switching resulted in irreversible changes in both "Peak" and "Dip" plasmonic shifts (increased values after collapsing the brushes and re-swelling; will be termed "overshifts"). Such and example can be seen in fig. 4.16. These changes suggest that PNIPAM brushes are not swollen to the same extent as before collapsing the brush. A possible explanation for these "overshifts" could be that some of the DTBU initiator molecules are oxidized [148], the bromide moiety leaving prematurely [132], which possibly produces less packed polymer brushes, or assembly of disulfide multilayers [131], which result from poor solubility of disulfides before the reaction. Nevertheless, the unexpected "overshifts" after each polymer brush collapse seem to slowly decrease and eventually result in plasmonic shift returning to the baseline as seen in fig. 4.16 after the 3rd conformational switch.

It is also important to mention, that in order to go above PNIPAM LCST temperature, resistive heating was applied in most cases locally on the gold surface, but the actual temperature induced is not determined. Therefore, caution should always be taken with the applied voltage on the functionalized sample of interest, because as reported previously [131], thiols and disulfides might re-arrange on the gold surface as it is still not understood as how they are bonded to it. Alternatively, in cases, where insplorion setup was used with smaller PNIPAM functionalized sample chips, the temperature control unit was utilized to induce polymer brush conformational change above their LCST, but the "overshifts" were still evident.

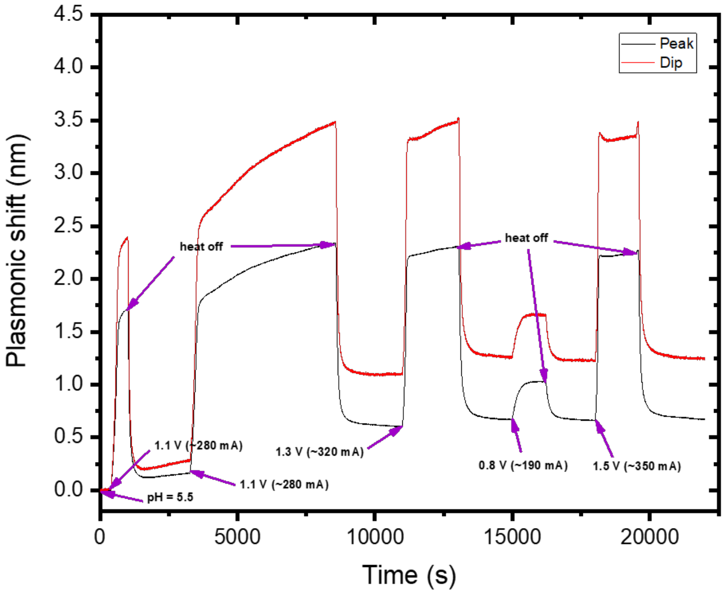

Figure 4.16: DTBU initiated 45*v*%MQPNIPAM2hrs15min polymer brush plasmonic shift thermo-responsive collapse tests, where unexpected "overshifts" appear after the first and second switching and disappear once collapsed the third time.

In order to try and avoid these "overshifts", possibly related to DTBU initiator and also to increase the solubility of the initiator, a thiol equivavalent HS-C_{11}-OC(O)-IzoButyrate-Br (depicted as TBU) was chosen to form SAMs on gold sample surfaces and initiate the future PNIPAM polymer brush polymerization reactions.

As it is observed in the figure 4.17, the previously mentioned "overshifts", as in some cases with DTBU initiated PNIPAM polymer brushes, have been eliminated due to this chemical change. After collapsing and re-hydrating the brushes, the plasmonic shift becomes the same as before increasing the temperature above polymer brush LCST. Therefore, the discrepancies have been attributed to the better solubility of TBU initiator, possibly avoiding the formation of multilayers [131], resulting from precipitation of DTBU, which could possibly induce some structural re-arrangement of sulfur-sulfur/sulfur-gold bonds upon heating locally the surface and exposing the gold surface to contamination. [149, 150].

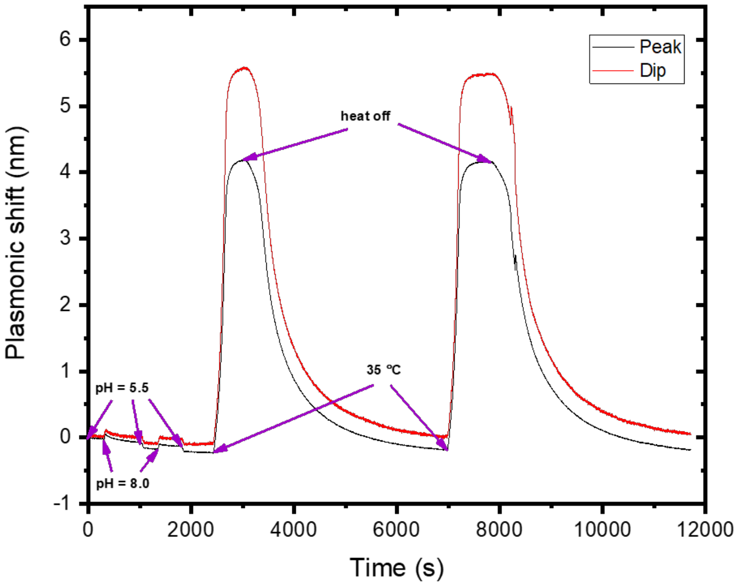

Figure 4.17: Control experiment of plasmonic shift between changing running buffer from 1x PBS (pH = 5.5) to 1x BBS (pH = 8.0) and 45*v*%MQPNIPAM35min polymer brush reversible plasmonic shift response to temperature change from RT to above PNIPAM LCST (reaction time 35 minutes; thiol initiated).

4.6 Real-time plasmonic shift TBU initiated PNIPAM polymer brush nanostructure gating for BSA transport

By trying to optimize solvent composition and polymerization time for TBU initiated PNIPAM polymer brushes in order to efficiently gate protein transportation, the reaction time was chosen to be 30 minutes and the MQ water amount 39*v*% (fig. 4.18; other attempts may be seen in Appendix D).

This protein transport gating experiment should be taken as an example of controlled trapping and release of BSA proteins on demand. Even though, a very small "Dip" plasmonic shift may be seen upon BSA injection in the swollen PNIPAM polymer brush regime, it can be regarded as negligible as it is most likely just a baseline drift. BSA adsorption happened as expected (as discussed in BSA and NA control experiments) in the collapsed state ("Peak" and "Dip" shifts resulted in 0.567 nm and 1.03 nm). Upon increase of pH to 7.9 (1x PBS), a lot of the proteins left the nanowells or the gold surface (according to decreased "Dip" and "Peak" plasmonic shifts), suggesting that the brushes could be too short in some nanowells, letting BSA out. However, at ~17500 seconds the plasmonic shift stabilized, leaving "Peak" and "Dip" plasmonic shifts 0.196 nm and 0.393 nm, respectively. This indicates, that a fraction of nanowells were coated with sufficiently dense and thick PNIPAM polymer brushes. After increasing the temperature above PNIPAM LCST again, the remaining proteins left the nanowells

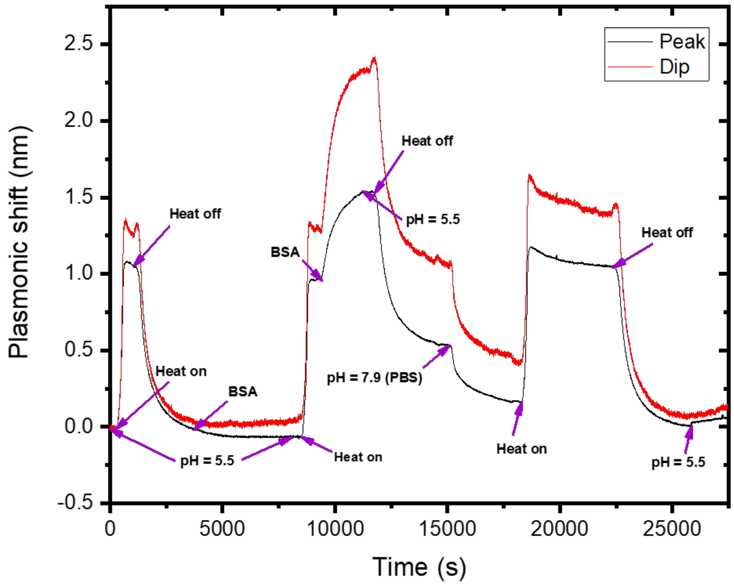

Figure 4.18: Real-time plasmonic shift BSA transport gating experiment with TBU initiated 39v%MQPNIPAM polymer brush (reaction time: 30 min.) nanostructures.

and the plasmonic shifts basically returned to the initial baseline values. The possible explanation for only partial BSA desorption upon changing the protein's net charge to negative, could be due to the fact that nanowell diameter is in a range of 80-90 nm, so it could be that some nanowells will be covered by brushes in the swollen state, while others not (as seen in figure 4.19) or the plasmonic shift decreased due to proteins desorbing from the silica, but still remaining inside the nanowells (the signal does not return to the baseline). Alternatively, some PNIPAM polymer chains continued to grow while others not due to possible radical-radical termination events [151].

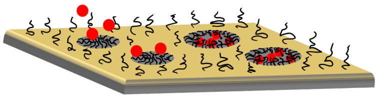

Figure 4.19: A representation of some nanowells having slightly bigger diameter than others (in the range of 10 nm). If the polymer brushes are not long enough to cover all of the nanowells, some proteins could translocate into the interior. The scaling of the polymer brushes, nanowells and proteins are not correct in order to better illustrate the example.

In order to possibly achieve thicker PNIPAM polymer brushes on the nanowell surface, the volume fraction of MQ water was increased by 1v% and the resulting plasmonic shifts from polymer chain collapse may be seen in figure 4.20. As observed, the resulting plasmonic shifts upon heating the sample surface are even smaller than in the previous experiment (fig. 4.18, which was taken as an indication, that the polymer brushes are either less thick, than in the case with 39v%PNIPAM30min polymer brushes or have lower grafting density, so the gating of BSA transport was not investigated further. In addition, the plasmonic shifts upon repeated collapse of 40v%PNIPAM30mins PNIPAM polymer brushes differ by ~0.1 nm and this is possibly due to the fact that the applied voltage during the second polymer brush collapse was 0.1 V lower than for the first and resulted in not a fully collapsed brush.

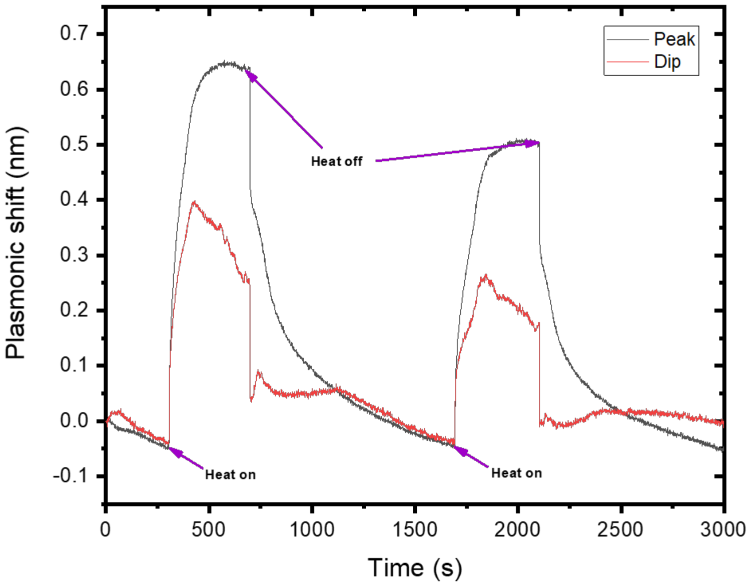

Figure 4.20: Resulting plasmonic shifts upon increasing the temperature above PNIPAM LCST with 40*v*%MQPNIPAM polymer brushes (reaction time 30 minutes; thiol initiated).

4.7 Plasmonic shift reproducibility investigation upon collapsing PNIPAM polymer brushes

Due to the fact that by slightly increasing the MQ water amount in the reaction, which should promote chain growth, PNIPAM polymer brush "Peak" and "Dip" plasmonic shifts have become smaller than in the case of 39*v*%PNIPAM30mins, an investigation for polymer brush plasmonic shift reproducibility (in terms of thickness and/or grafting density) was needed.

First of all, two nanowell sample surfaces grafted with the same batch of 40*v*%PNIPAM30mins polymer brushes have been produced and can be seen in figures 4.21 and 4.22.

As can be seen from the "Peak" and "Dip" plasmonic shifts in both experiments, even in the same batch polymerized PNIPAM polymer brushes may possibly result in different thicknesses and/or grafting densities. The difference between the two are on a factor of ~2 and ~2.5 in terms of "Peak" and "Dip" plasmonic shifts, respectively. Similar inconsistencies have been noticed for 45*v*%MQPNIPAM30min polymer brushes, which have been attempted to be reproduced at least 1 time and may be seen in figures 4.23, 4.24.

The first example (fig. 4.23) resulted in much lower (a factor of ~3.7 and ~8.1 for "Peak" and "Dip", accordingly) "Peak" and

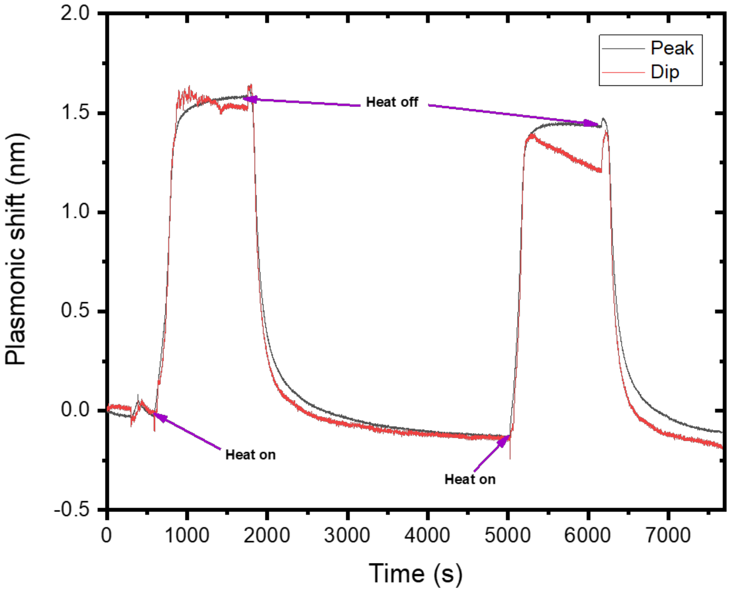

Figure 4.21: Resulting plasmonic shifts upon increasing the temperature above PNIPAM LCST with 40*v*%MQPNIPAM polymer brushes (reaction time 30 minutes; thiol initiated; 1st sample of the same batch).

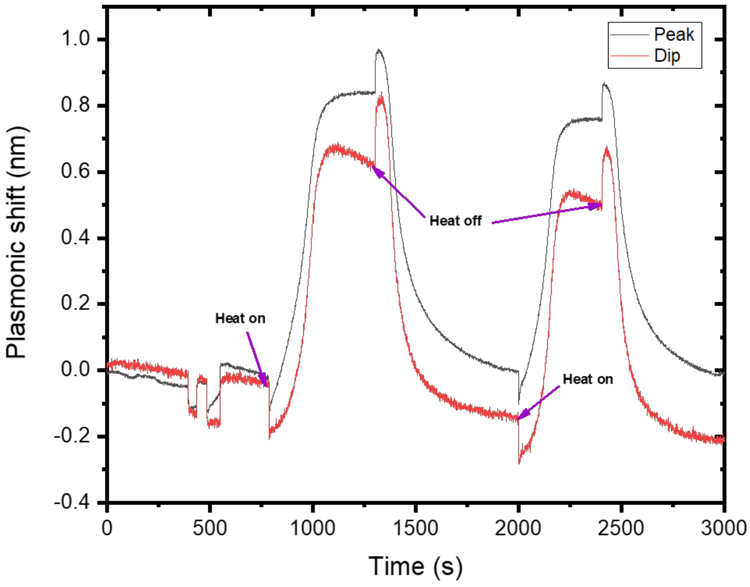

Figure 4.22: Resulting plasmonic shifts upon increasing the temperature above PNIPAM LCST with 40*v*%MQPNIPAM polymer brushes (reaction time 30 minutes; thiol initiated; 2nd sample of the same batch).

"Dip" plasmonic shifts compared to 2nd and 3d time attempts to reproduce functionalized nanowells.

It can be reasoned by the fact, that the solvent mixture with the monomer and the ascorbic acid was not degassed for 30 minutes, but for 25 minutes instead. This could have resulted in slightly higher oxygen content, which resulted in some chain termination events, in comparison to the other reaction (fig. 4.24), thus making the PNIPAM polymer brushes less thick or the grafting density in this case was lower due to some initiator SAM defects on the

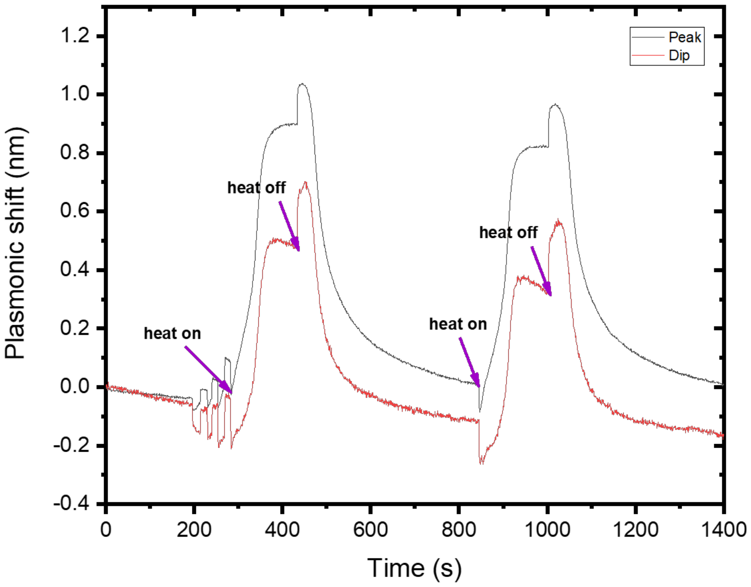

Figure 4.23: "Peak" and "Dip" plasmonic shifts upon increasing the temperature above PNIPAM LCST with 45*v*%MQPNIPAM polymer brushes (reaction time 30 minutes; thiol initiated).

surface. Also, it was noticed, in this case, that the transfer of the solvent mixture in the polymerization vessel took ~2 minutes slower, which could produce a less homogeneous layer, in terms of polymer brush thickness, and result in smaller "Peak" and "Dip" plasmonic shifts, because the chain growth was initiated earlier for a part of the surface while for the rest was not. The three small "Peak" and "Dip" plasmonic shift "spikes" seen between 200 seconds and the first indicated heating mark were resistive heating attempts with too small voltages.

The attempt to reproduce 45*v*%PNIPAM polymer brush collapse experiment seen in figure 4.23 resulted in much higher "Peak" and "Dip" plasmonic shifts (fig. 4.24.).

It is important to mention, that the two attempted plasmonic shift reproducibility experiments with 45*v*%MQPNIPAM30mins are from different polymerization batches. Also, the transfer of the solvent mixture to the polymerization container from the degassing flask for the 2nd attempt took ~3 minutes whereas for the 1st attempt (fig. 4.23) it took ~5 minutes. The slower liquid transferring speeds are possibly related to tube clogging and/or the pump having contaminants on the membrane, thus producing varying suction.

Some inspiration was taken from previously reported optimized PNIPAM polymer brush growth conditions in order to achieve more reproducible PNIPAM polymer brush functionalized layers in terms of homogeneity and height [110]. Thus, MQ water/MeOH solvent mixture during the polymerization procedure was changed

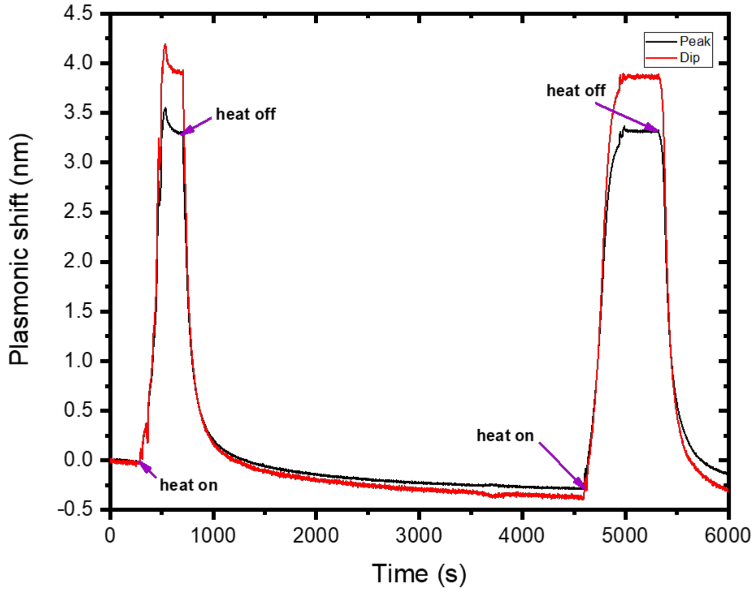

Figure 4.24: "Peak" and "Dip" plasmonic shifts upon increasing the temperature above PNIPAM LCST with 45*v*%MQPNIPAM polymer brushes (reaction time 30 minutes; thiol initiated; 2nd attempt to reproduce the plasmonic shifts).

to contain 16*mol*% (or 70.3*v*%MQ water) MeOH. BSA protein transport gating fluorescence (with fluorescently tagged FITC-BSA) and complementary real-time plasmonic shift experiments were attempted with these functionalized nanowells and will be presented, and discussed in the next section.

4.8 Real-time fluorescence and plasmonic shift experiments on BSA transportation gating with PNIPAM polymer brush functionalized nanostructures

As complementary proof to plasmonic shift BSA gating experiments, a flow cell for optical microscopy has been designed, as mentioned beforehand. One FITC-BSA protein transport gating experiment will be discussed in this chapter. Sample surface for such fluorescence microscopy experiment is half bare gold (with no structures) - half nanowells (fig. 3.6; 80 - 90 nm in diameter), functionalized with PNIPAM brushes.

The nanowells (on the right) and bare gold (on the left) can be seen in figure 4.25. The dark field observation of the structures was utilized before running the gating experiment in order to establish focus and wanted position. Also, by comparing these two sides and subtracting the fluorescence intensity it is possible to determine when the fluorescently tagged FITC-BSA proteins are trapped or released from the vicinity of the nanowells as will be seen later on.

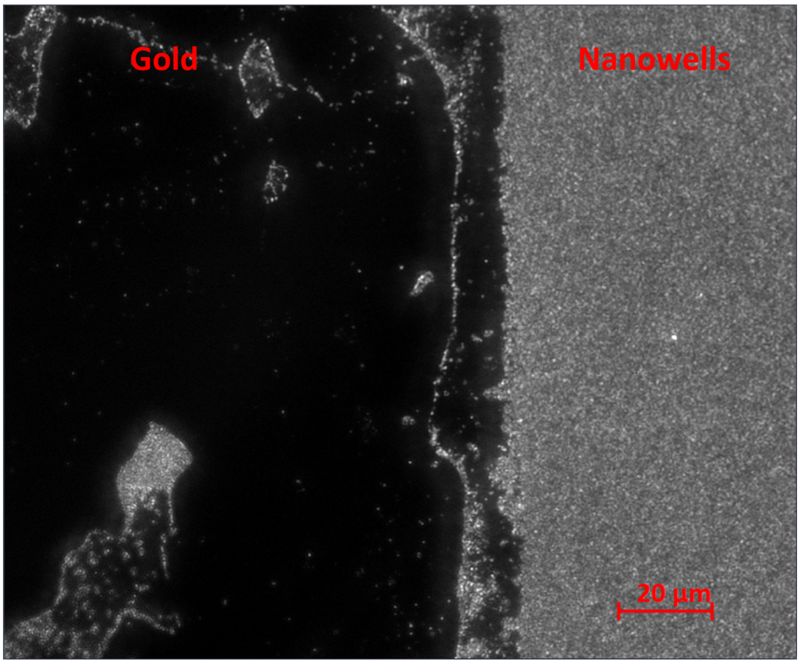

Figure 4.25: Dark-field image of bare half gold (on the left) - half nanowell(on the right) sample surface (50 x magnification, 4.2 ms exposure time and 630 nm LED illumination; air).

The fluorescently labelled FITC-BSA gating procedure with PNIPAM functionalized nanowells in fluorescence microscopy experiment continue as in the previously described gating scheme in fig. 4.12.

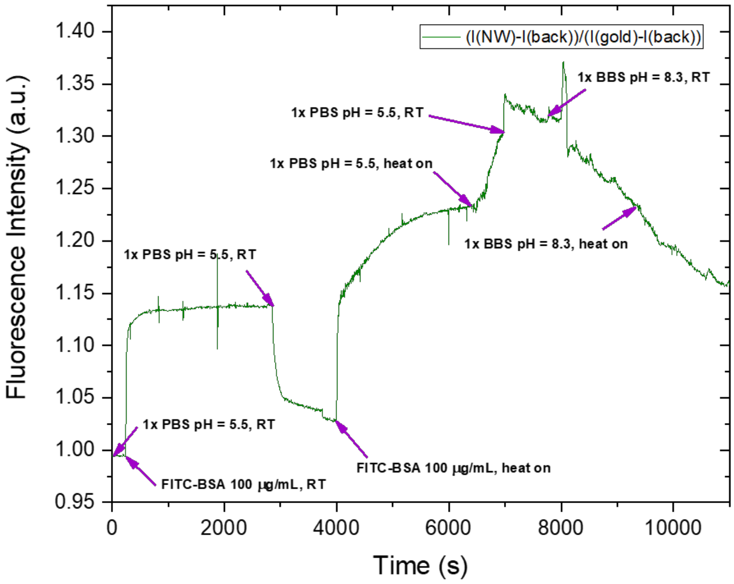

Figure 4.26: FITC-BSA protein transport gating fluorescence experiment with 16*mol*%MeOHPNIPAM polymer brush (reaction time: 10 minutes) gold-nanowell surface (images taken every 15 seconds).

By employing 16*mol*%MeOHPNIPAM (polymerized for 10 minutes) polymer brush functionalized nanowells, FITC-BSA protein transport gating experiment with optical microscopy was conducted and may be seen in figure 4.26. This particular polymerization time has been chosen, because according to the swollen and collapsed heights shown in 4.28 for 10 minute polymerization time, polymer brushes should be able to block the nanowells in the swollen state (swollen height is ~49 nm) and let FITC-BSA through in the pore open regime (collapsed height is ~19 nm at above PNIPAM LCST), because nanowell diameter is between 80 - 90 nm.

As seen from fig. 4.26 after the injection of FITC-BSA over swollen brushes at pH = 5.5 and rinsing with running buffer, the fluorescence intensity did not return to the baseline value (~1 a.u.). This indicates that some proteins either translocated through the polymer brushes and adsorbed in the nanowell interior or adsorbed on the surface due to some surface defect (e.g. some pores have too short polymer brushes or these particular polymer brushes has worse grafting density), or both. Also, the fluorescence intensity from the nanowell side compared to the gold side of the sample surface is higher upon FITC-BSA injection at ~300 seconds, probably because of the previously mentioned (in section 3.2.6) higher light transmission through the nanowells compared to bare gold. In order to achieve full FITC-BSA adsorption inside the nanowells, the polymer brushes were collapsed above their LCST and proteins were injected with a consequent rinse step. Furthermore, the higher fluorescence intensity upon injection of FITC-BSA on collapsed PNIPAM polymer brush functionalized gold-nanowell surface compared to the period when the proteins were injected over swollen brushes, results from proteins adsorbing in the interior of the nanowells, on the collapsed PNIPAM brushes, or both. Nevertheless, desorption of FITC-BSA at pH = 8.3 in both - collapsed and swollen state polymer brush nanostructures - was attempted. The fluorescence signal starts decreasing as soon as the net charge of FITC-BSA becomes negative, which means that the protein is desorbing and the reason for this could be too short PNIPAM brushes not blocking the nanowells when they are supposed to. Additionally, compared to the QCM-D control experiment (fig. 4.7), the desorption of FITC-BSA is much slower, which could be due to the fact of slower liquid exchange in the flow cell (FITC-BSA molecules are circulating in the flow cell chamber), but also possibly indicating non-specific binding to the gold surface or PNIPAM polymer brushes in the collapsed state.

Protein transport gating procedure with $16 mol\%$MeOHPNIPAM (reaction time: 10 minutes) polymer brush functionalized nanowells from the same polymerization batch as sample seen in fig. 4.26 was repeated in the real-time plasmonic shift setup and can be observed in the figure 4.27, BSA proteins are adsorbing irreversibly on the surface even when PNIPAM polymer brushes are in the swollen state and supposed to be in the extended conformation. Also, much higher than expected plasmonic shifts in "Peak" and

"Dip" upon injection of BSA suggest that the protein is binding to the gold surface. The subsequent increase to pH = 8.32 resulted in BSA desorption from the interior of the nanowells, but not from the gold surface due to the expected plasmonic signal change when the protein adsorbs inside the nanowells (as seen in figure 4.8). The remaining plasmonic shift, which did not return to the baseline at ~16000 seconds, indicating non-specific irreversible binding of BSA to the gold surface. In addition, this experiment indicates that both samples from the same polymerization batch possible have insufficiently packed PNIPAM polymer brushes (lower grafting density than expected) in the swollen state not only in order to block protein transport in the interior of the nanowells, but also adsorption on the gold surface.

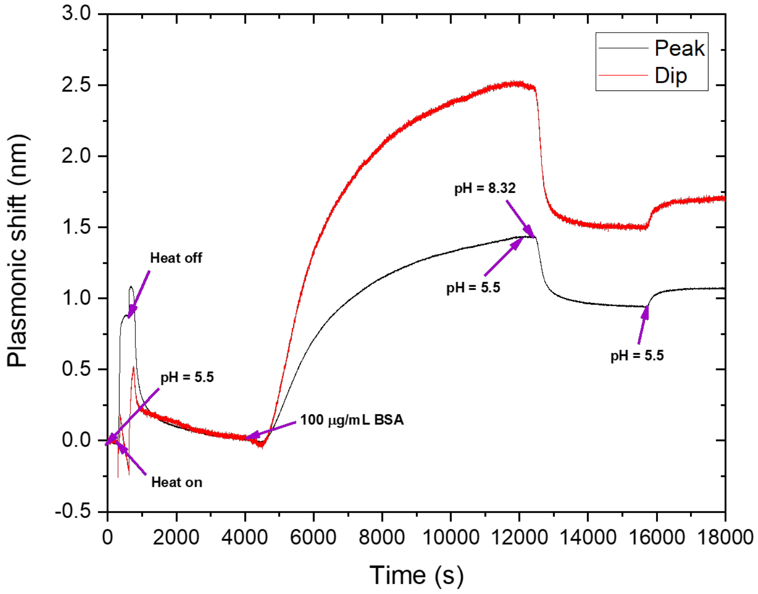

Figure 4.27: Real-time plasmonic shift gating experiment attempt of BSA protein transport with 16*mol*%MeOHPNIPAM polymer brush (polymerized for 10 minutes) functionalized nanowells.

Other polymerization time same solvent composition PNIPAM polymer brush dry, collapsed and swollen heights were determined with the non-interactive probe method in SPR and Fresnel modelling, and are presented in fig. 4.28. Dry, collapsed and swollen PNIPAM brush heights produced with this solvent mixture cannot be differentiated between 5 and 10 minute, and 15 and 25 minute reaction times, respectively. The reasoning for this could be varying grafting densities in all of the cases and possible polymer chain termination at 15 minute reaction time, which could be induced either by oxygen species present during the reaction or non-homogeneous chain growth.

All in all, the conclusion from the fluorescence and plasmonic shift gating experiments is that PNIPAM polymer brush thickness and possibly grafting density remain to be further optimized. Polymer

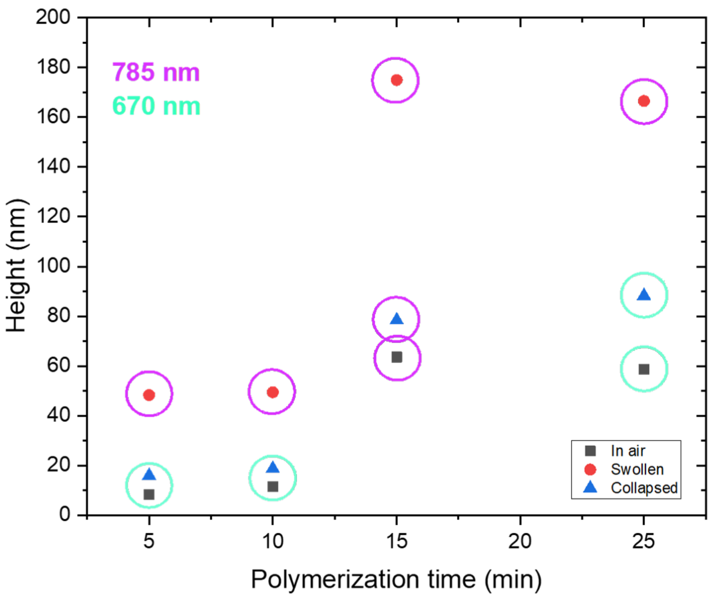

Figure 4.28: 16*mol*%MeOHPNIPAM polymer brush (polymerized at different time) dry, collapsed and swollen heights and determined with non-interactive probe method and Fresnel modelling.

brush thickness homogeneity could be improved by keeping one type of solvent composition, but changing other parameters such as reaction and degassing time, and injecting dissolved ascorbic acid straight into the reaction vessel with other polymerization reagents and nanowell surfaces in order to keep a more uniform polymer brush layer by avoiding liquid transferring. The grafting density, directly linked to the initiator SAM, could be improved by exposing the surface with the initiator SAM to ambient environment less, so that the possibly prematurely leaving bromide moiety could remain intact on the initiator molecules and trigger polymer chain growth during the reaction. Alternatively, one could avoid re-using the same sample surface, which could impede homogeneous SAM formation due to surface defects upon continuous handling with e.g. a tweezer.

4.9 Investigation of BSA adsorption on bare silica and PNIPAM polymer brushes

BSA adsorption at different pH on the TBU initiated PNIPAM polymer brush functionalized sensors may be seen in figures 4.29, 4.32, 4.30, 4.34 and 4.36.

In the SPR experiment (fig. 4.29), where BSA was adsorbed on PNIPAM collapsed brushes, almost irreversible binding (some BSA is rinsed away with the running buffer) may be observed.

When the polymer brushes are re-swollen and the pH is increased to pH = 8.0 (1x PBS), BSA desorption seems almost indistinguishable from the baseline drift. This irreversible adsorption or very slow

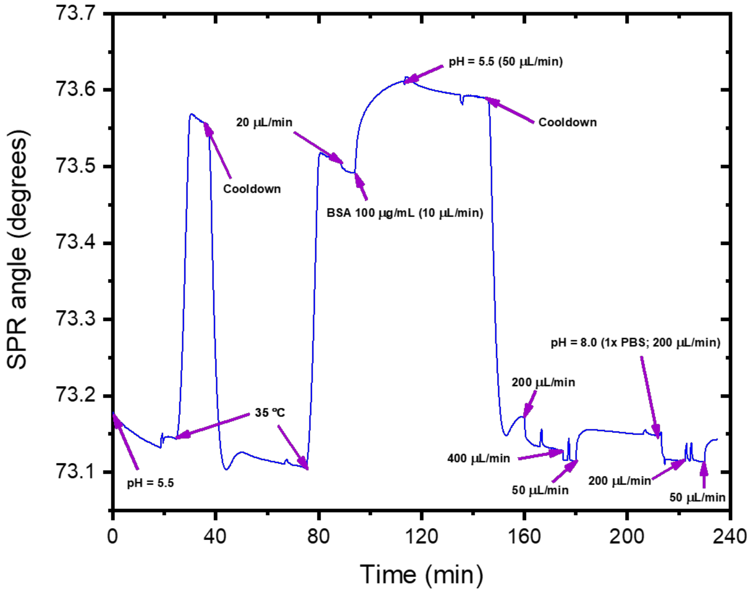

Figure 4.29: BSA adsorption on the collapsed thiol-initiated 45*v*%MQPNIPAM30mins polymer brushes at pH = 5.5 and attempted desorption at pH = 8.0 (1x PBS).

desorption has been noticed in the some of the plasmonic shift gating experiments, hence it cannot be ignored and attributed only to, e.g. exposed bare gold layer and more investigation is needed.

Inspired by the BSA adsorption on the collapsed PNIPAM brushes at pH = 5.5, three additional QCM-D experiments have been conducted, where BSA was adsorbed on collapsed PNIPAM brushes at different pH values ranging around its IEP. When BSA was injected over collapsed PNIPAM brushes at pH = 4.5 (fig. 4.30; zoom in image of the region of interest is seen in fig. 4.31), a clear negative frequency shift of ~9.2 Hz can be seen, indicating adsorbed proteins even after the rinse step. Also, when the brushes were re-swollen and the pH was increased to 8.0, only a small fraction of protein has desorbed (positive frequency shift of 1.38 Hz) over a period of 2000 seconds. This indicates not only a strong interaction with the collapsed PNIPAM polymer brush, but a possible BSA structure reorganization. It could be possible due to the fact that the hydrogen bonding between PNIPAM brush amide moiety and protein hydrogen donors, carboxylic acid moieties, are more prevalent at lower pH. Because of this, exposition of the hydrophobic subdomains of BSA could appear, which interact with the isopropyl moieties of PNIPAM chains.

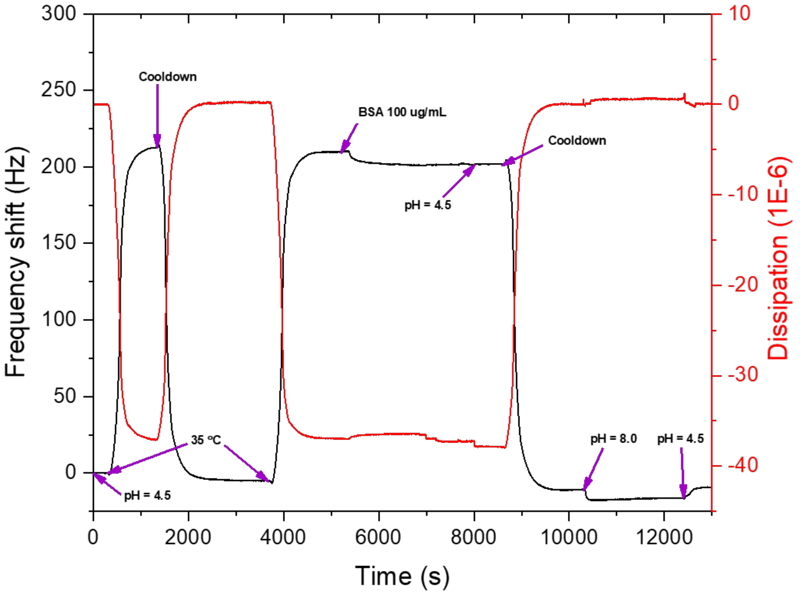

Figure 4.30: BSA adsorption on the collapsed thiol-initiated 45v%MQPNIPAM20mins polymer brushes at pH = 4.5 and desorption at pH = 8.0 (1x PBS).

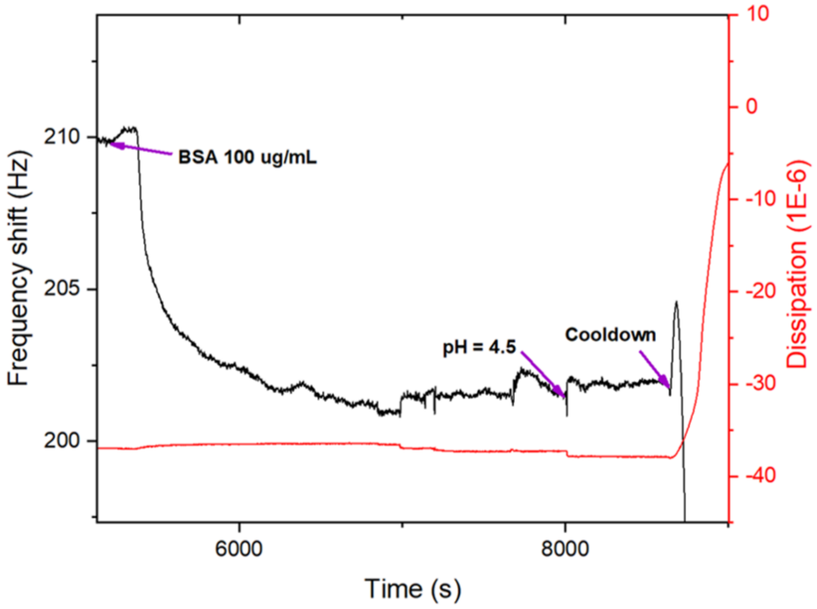

Figure 4.31: A zoomed in image of BSA adsorption on 45v%MQPNIPAM, polymerized for 20 minutes, collapsed brushes at pH = 4.5.

In contrast to BSA adsorption at pH = 4.5, adsorption at pH = 5.5 on the collapsed brushes (fig. 4.32; zoomed in image of relevant region is seen in fig. 4.33) resulted in almost all BSA being desorbed after increasing the pH to 7.6 (a negative 1.4 Hz frequency shift left after pH increase to 7.6). This is peculiar, because in the same experiment BSA was also injected over the collapsed brush at pH = 7.6 and no significant adsorption on the brushes is observed (e.g. assuming that a monolayer for BSA results in frequency shift of ~20-30 Hz as seen in figures 4.6 and 4.7 and as reported by Heider et al. for neutravidin [152]).

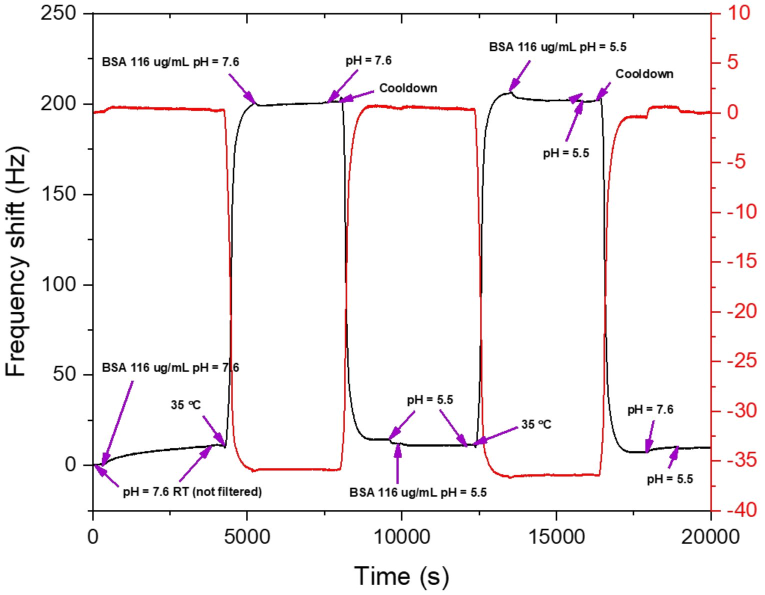

Figure 4.32: BSA adsorption on the collapsed thiol-initiated 45*v*%MQPNIPAM20mins polymer brushes at pH = 5.5 and desorption at pH = 7.6 (1x PBS).

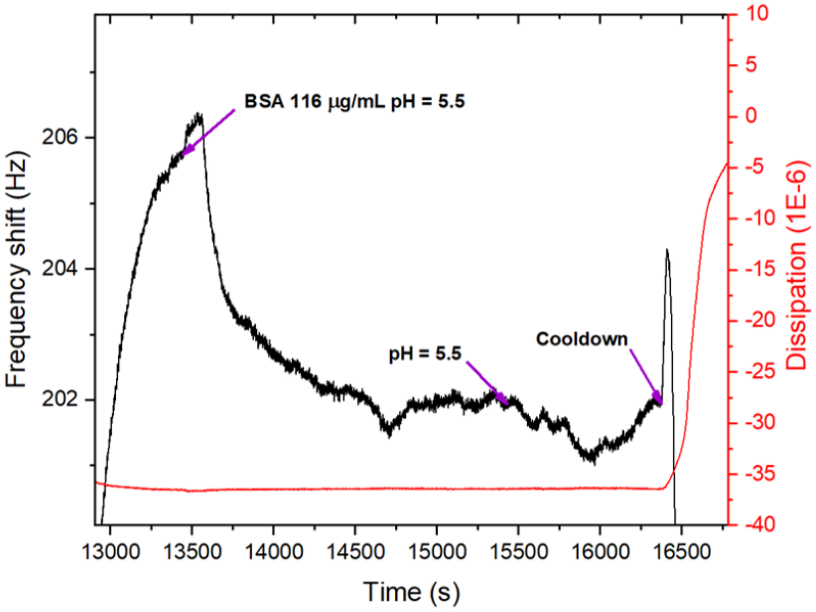

Figure 4.33: A zoomed in image of BSA adsorption on 45*v*%MQPNIPAM, polymerized for 20 minutes, collapsed brushes at pH = 5.5.

The discrepancies between the BSA adsorption QCM-D experiments suggest that there must be an optimal pH, at which BSA can be adsorbed inside the nanowells and still be removed from the collapsed PNIPAM brushes and silica upon turning the protein net charge negative.

In BSA adsorption at pH = 6.0 case (fig. 4.34), full desorption of the protein can be noticed at the moment, where the polymer brush layer is not above LCST temperature (fig. 4.35) anymore (~8700 seconds; return to the baseline after brush collapse). This is not observed in the QCM-D experiment, where BSA was adsorbing on collapsed PNIPAM polymer brushes at pH = 4.5.

Therefore, it can be concluded, that there really should be an optimized pH, where BSA adsorbs on the collapsed PNIPAM polymer brush functionalized surface and reversible desorbs upon re-swelling them again.

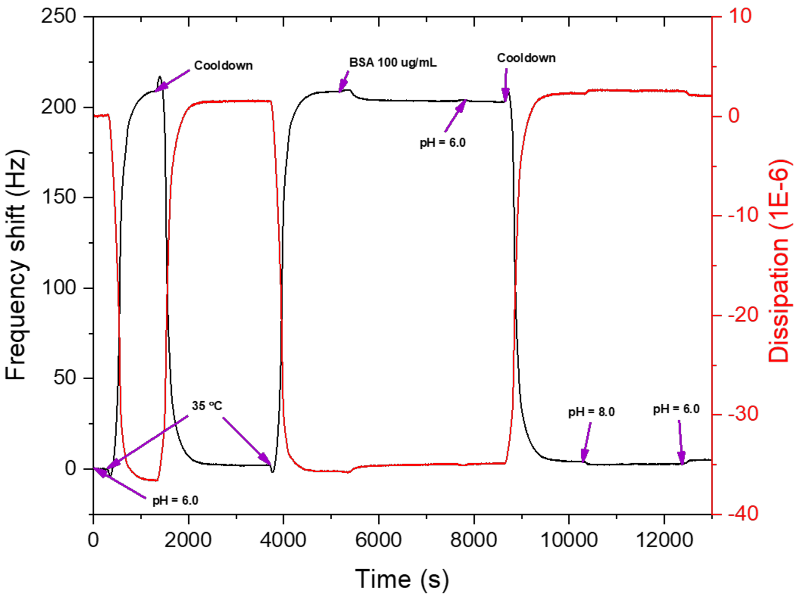

Figure 4.34: BSA adsorption on the collapsed thiol-initiated 45*v*%MQPNIPAM20mins polymer brushes at pH = 6.0 and desorption at pH = 8.0 (1x PBS).

Furthermore, as an extra test to all previous protein adsorption experiments at different pH values on PNIPAM polymer brush functionalized QCM-D sensors, BSA was adsorbed on 16$mol\%$ MeOHPNIPAM, polymerized for 15 minutes, brushes at pH = 5.5 again (fig. 4.36), but as seen at the cooling step, starting at ~15000 seconds, the slowly decreasing frequency shift can either be the protein desorption or the slow re-hydration of PNIPAM polymer brushes.

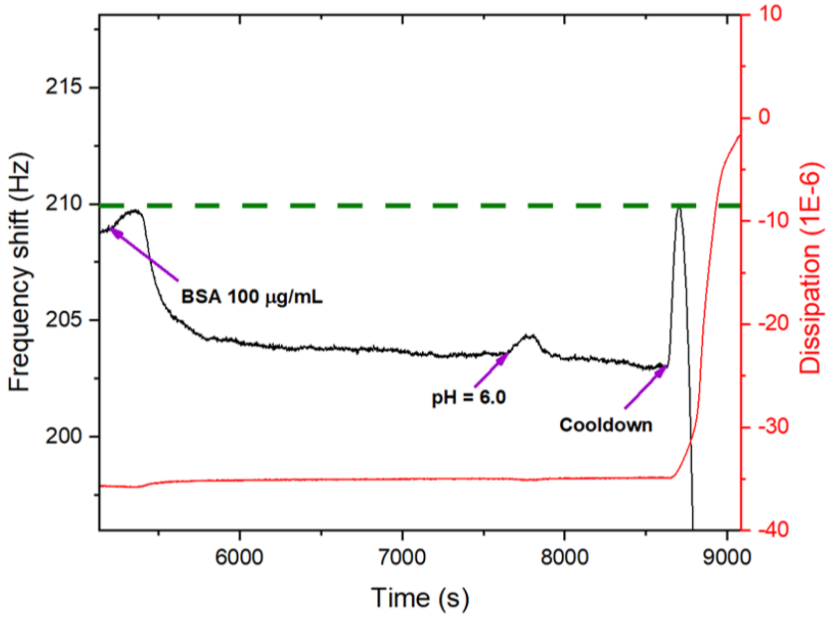

Figure 4.35: A zoomed in image of BSA adsorption on 45*v*%MQPNIPAM, polymerized for 20 minutes, collapsed brushes at pH = 6.0.

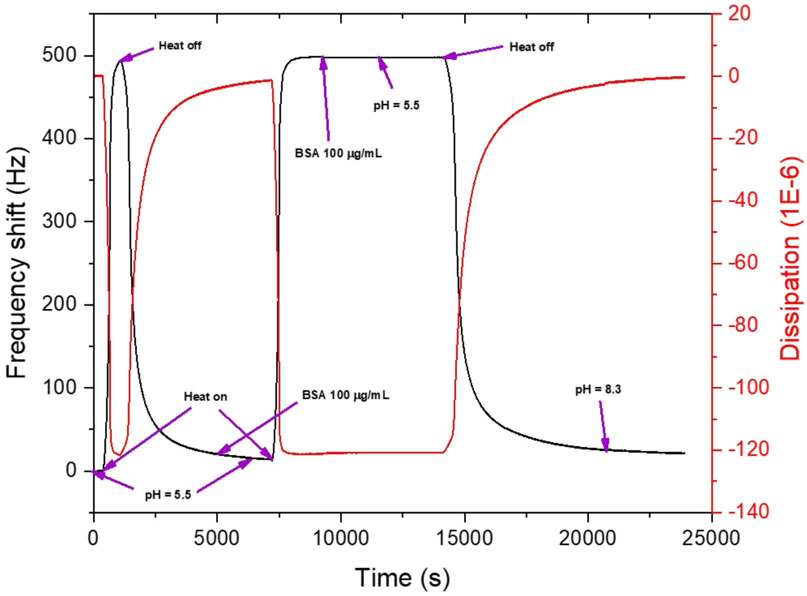

Figure 4.36: BSA adsorption on thiol-initiated 16*mol*%MeOHPNIPAM15min functionalized gold coated QCM-D crystal at pH = 5.5 and desorption at pH = 8.3 (1x BBS).

However the negative frequency shift (~1-2 Hz; as seen in fig. 4.37) upon injecting BSA over the collapsed brushes and rinsing with the running buffer is insignificant compared to the frequency shift resulting from the collapsed brushes. In this case, it is hard to say if BSA is slowly desorbing upon rinsing the collapsed brushes at pH = 5.5 or possibly a drift in baseline over the course of ~1 hour is observed.

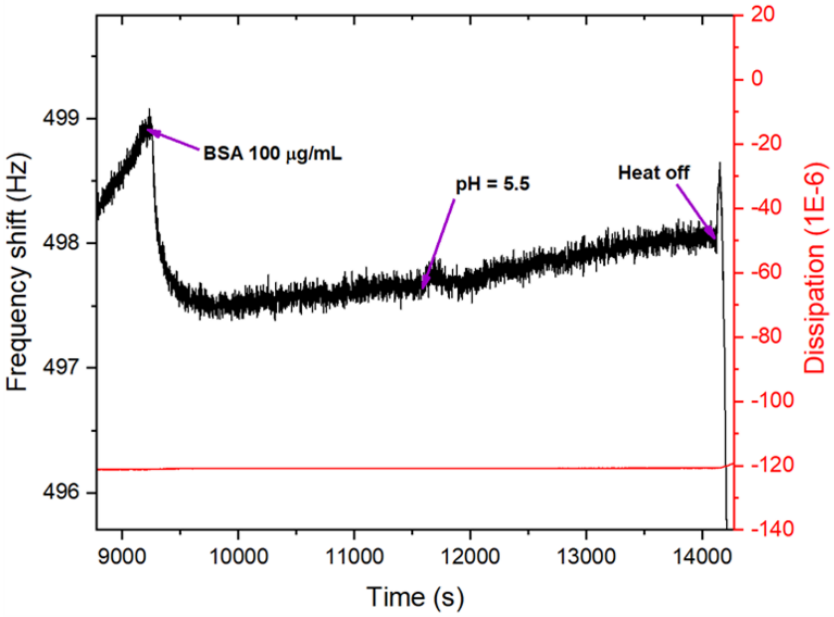

Figure 4.37: A zoomed in image of BSA adsorption on 16*mol*%MeOHPNIPAM, polymerized for 15 minutes, collapsed brushes at pH = 5.5.

Knowing that BSA does not adsorb on collapsed PNIPAM brushes at pH = 7.6 (fig. 4.5), but possibly adsorbs irreversibly at pH = 5.5 (figures 4.32 and 4.36), an optimum pH might be established for BSA adsorption so that the proteins would adsorb on SiO_2 inside the nanowells, but not on the collapsed brushes. An additional experiment showing BSA adsorption on SiO_2 at pH = 6.0 is presented in figure 4.38. Slower than at pH = 5.5 (fig. 4.6) adsorption and desorption (compared to FITC-BSA desorption in fig. 4.7) are observed.

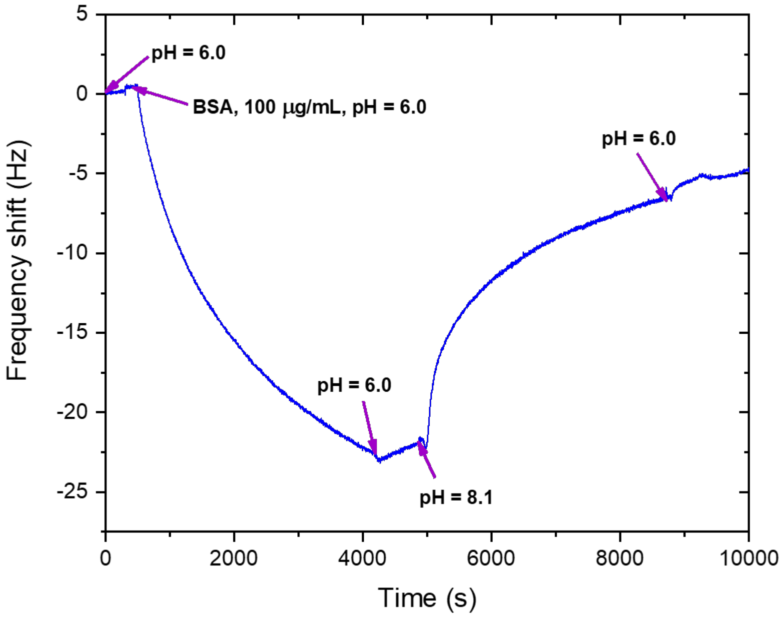

Figure 4.38: QCM-D control experiment of BSA adsorption on SiO_2 surface at pH = 6.0 and desorption at pH = 8.0.

It could be postulated, that an optimum pH between pH = 6.0 and pH = 7.6 could be found for BSA adsorption on PNIPAM polymer brush functionalized nanowells, where unwanted BSA adsorption on the polymer brushes could be minimized or avoided and still be applied for reversible adsorption on silica.

Conclusions and future work 5

Different PNIPAM polymer brush polymerization times and solvent compositions during the reaction have been tested. The brushes were manufactured in solvent mixtures of MQ water and MeOH, where the content of water ranged between ~35-70*v*% and are shown in some cases to be densely enough packed to block protein transport according to plasmonic shift measurements when BSA is injected over the swollen state polymer brush functionalized nanostructures. This makes them more feasible to apply for protein adsorption only inside the nanowells avoiding the gold surface, because the proteins are repelled by the polymer brushes with high surface grafting density [58, 94]. A successful attempt (as seen from the real-time plasmonic shift measurement in fig. 4.18) to produce PNIPAM polymer brush functionalized nanowells as gating systems for BSA protein transport has been achieved by choosing the 39*v*% of MQ water in the reaction mixture (the rest being MeOH) and polymerization time to be 30 minutes.

The previously reported [110] utilization of 16*mol*% to 31*mol*% (almost the double water content) in the solvent mixture during the polymerization (reaction time: 10 minutes) resulted in polymer brushes, which either have too small grafting density or are too short in the swollen state according to real-time plasmonic shift and fluorescence experiments. This lead to a conclusion, that these particular brushes were not suitable for protein transport gating experiments.

As seen from the PNIPAM polymer brush collapse tests in figures 4.16 and 4.17, TBU initiated polymer brushes seem to have better conformational switching behavior, in terms of reversible plasmonic shift after the collapse of the brushes, compared to the brushes initiated with DTBU.

In the future, more reproducible polymerization procedure in terms of polymer brush height, is going to be worked on, because as seen in figures 4.21 and 4.22, the produced polymer brushes even in the same batch may differ in the grafting density or thickness according to discrepancies in plasmonic shifts upon collapsing the brushes. This is going to be achieved by repeating polymerizations with 39*v*% of MQ water (rest MeOH) or changing the polymerization time for this particular solvent mixture. Also, determination of polymer brush dry, collapsed and extended heights with SPR will be crucial in this respect. A complementary experiment to the real-time plasmonic shift measurement on BSA transport gating will be conducted with 39*v*%MQPNIPAM polymer brushes (reaction time: 30 minutes). Additionally, an optimum pH for BSA transport through PNIPAM polymer brushes has to be investigated further in order to minimize or avoid undesired adsorption on collapsed polymer brushes. These experiments can be done for NA as well. Moreover, other protein variants as well as human blood serum and even DNA transport through the functionalized nanowells could be tested in order to see possible blockage by PNIPAM polymer brushes. Once the polymerization procedure is reproducible and desired height polymer brushes are achieved, confocal microscopy could be used as a tool in order to study protein trapping, release and possibly interactions with other molecules inside individual nanowells. Moreover, flow experiments through PNIPAM functionalized nanopores could be conducted, where protein molecules are pushed through the dense polymer brush layer with shear flow, e.g. to determine possible flow rates, which would be another milestone for the future single-molecule platform application.

Acknowledgements

With great respect I acknowledge the project sponsors - The Erling-Persson Family Foundation, who have funded this project.

Special acknowledgement is given to my main supervisor Andreas Dahlin, who has guided me well through the project and the PhD studies so far, my co-supervisor Anette Larsson and the reviewer of this thesis - Tiina Nypelö.

I would also like to thank all of my colleagues at Applied Surface Chemistry division, special thank you to Felix Hemmingsson and Sandra Benter, previous and current group members - John Andersson, Zeynep Adali, Oliver Olsson, Gustav Ferrand-Drake Del Castillo, Rebekah Hailes, Jolie Blake, Gustav Emilsson, Asaad Umair, Bita Malekian, Sophia Thiele, Marika Gugole, Kunli Xiong, Tim Robson and others, who have helped me either to edit this thesis, by having scientific discussions or introducing me to the instruments. Also, my family and friends for the moral support.

Justas Svirelis, Göteborg, February 2021

APPENDIX

Appendix A

Table A.1: Chemicals and materials used for this project

Material	Description
Sigma Aldrich	
2-propanol	$\geq$ 99%
Acetone	$\geq$ 99%†
Albumin–fluorescein isothiocyanate conjugate	≥7 mol FITCmol albumin
Bovine serum albumin	$\geq$ 96%
Borate buffer saline	tablets; pH 8.2
Copper (II) Bromide	99%
Bis[2-(2-bromoisobutyryloxy)- -undecyl] disulfide	97%; Stored degassed
Hydrogen chloride	37%
L-Ascorbic acid	99%
Methanol	99.8% anhydrous
N-isopropylacrylamide	$\geq$ 99%; Stored degassed
N, N, N′, N″, N″- -Pentamethyldiethylenetriamine	99%
Phosphate buffer saline	tablets; pH 7.2
Polyethylene glycol	35 kDa
Sulfuric acid	95.0% - 97.0%
Sodium dodecyl sulfate	$\geq$ 99%
Sodium hydroxide	$\geq$ 97%
Thermo Fischer Scientific	
Ammonium hydroxide solution	28-30%
Neutravidin	
NML Syringe Filter	Nonsterile, hydrophilic, 0.2 μm
Solveco	
Ethanol	95% and 99.7%
Circuitworks	
Conductive epoxy glue	Used for gluing insulated copper wires to samples
Merck	
Molecular sieves	0.3 nm
H_2O_2	30%

Continued on the next page

Table A.1: Chemicals and materials used for this project (cont.).

Material	Description
Prochimia	
HS-C11- OC(O)- IzoButyrate-Br	Stored degassed and frozen
RS components	
Polyether ether ketone	Used as the main block material for the flow cell
VWR	
Fused silica	Utilized as a material for flow cell windows
Picodent Twinsil	
Addition-curing duplicating silicone	Used for gluing flow cell windows
Dow Corning	
High vacuum grease	Used when vacuum drying the molecular sieves
Laysan Bio	
Thiolated polyethylene glycol	2 kDa
In-house	
Milli-Q water	ASTM Research grade Type I ultrafiltered water from a Millipore system (18.6 MΩs)

Appendix B

Fourier-transform infrared reflection absorption spectroscopy (FTIR-RAS) data. Parts of the spectra, which do not have a stable baseline are attributed to the defects of the re-used sample surface.

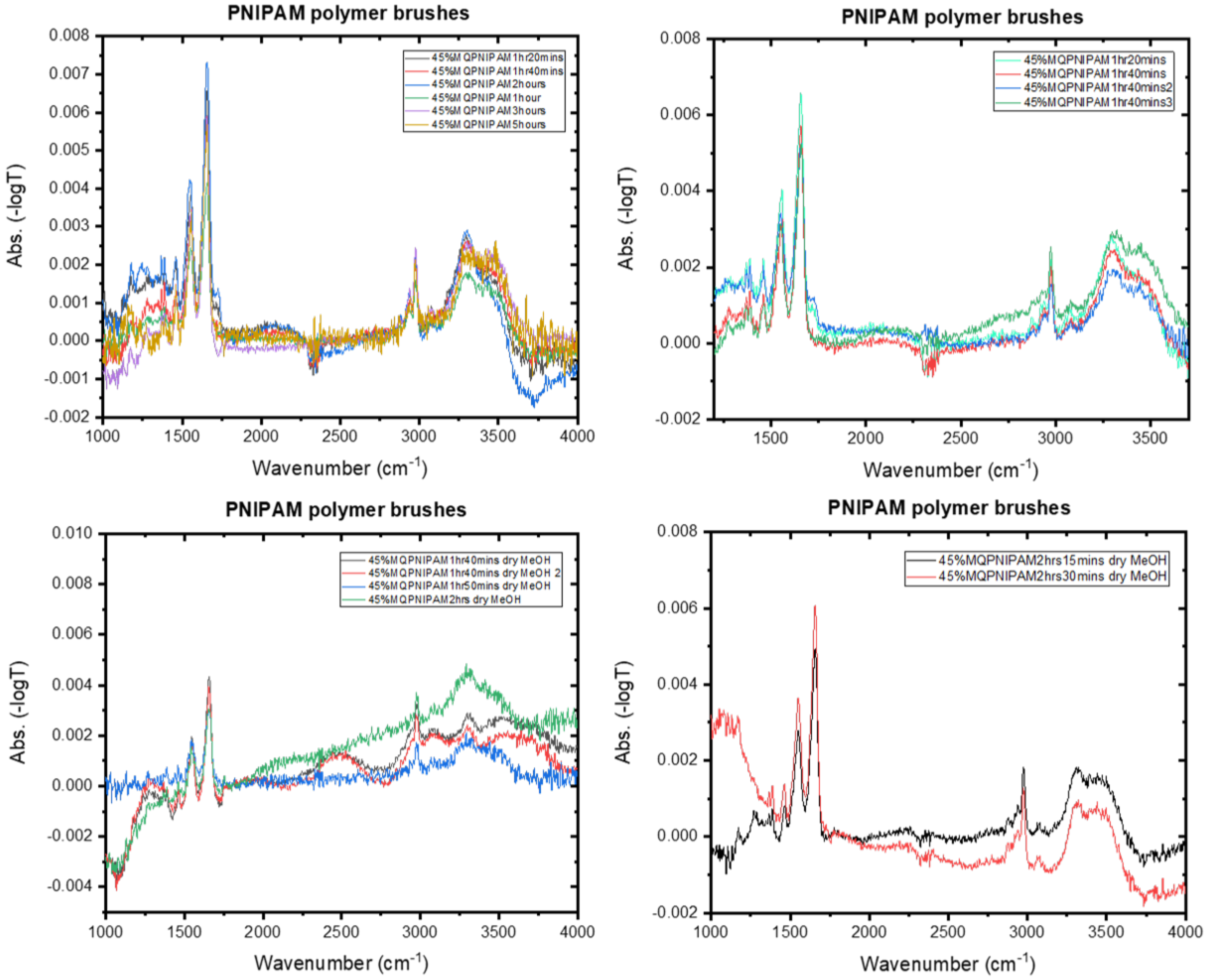

Figure B.1: FTIR ATR-RAS spectra of PNIPAM polymerizations containing 45v% MQ water in the solvent mixture. Also, subfigures having "dry MeOH" denoted in the legends describe reactions having dried MeOH with 3 Å molecular sieves in the solvent mixture. The two subfigures at the top contain spectra, which are offsetted at 2500 cm^{-1} and the spectra in the bottom subfigures at 1600 cm^{-1}.

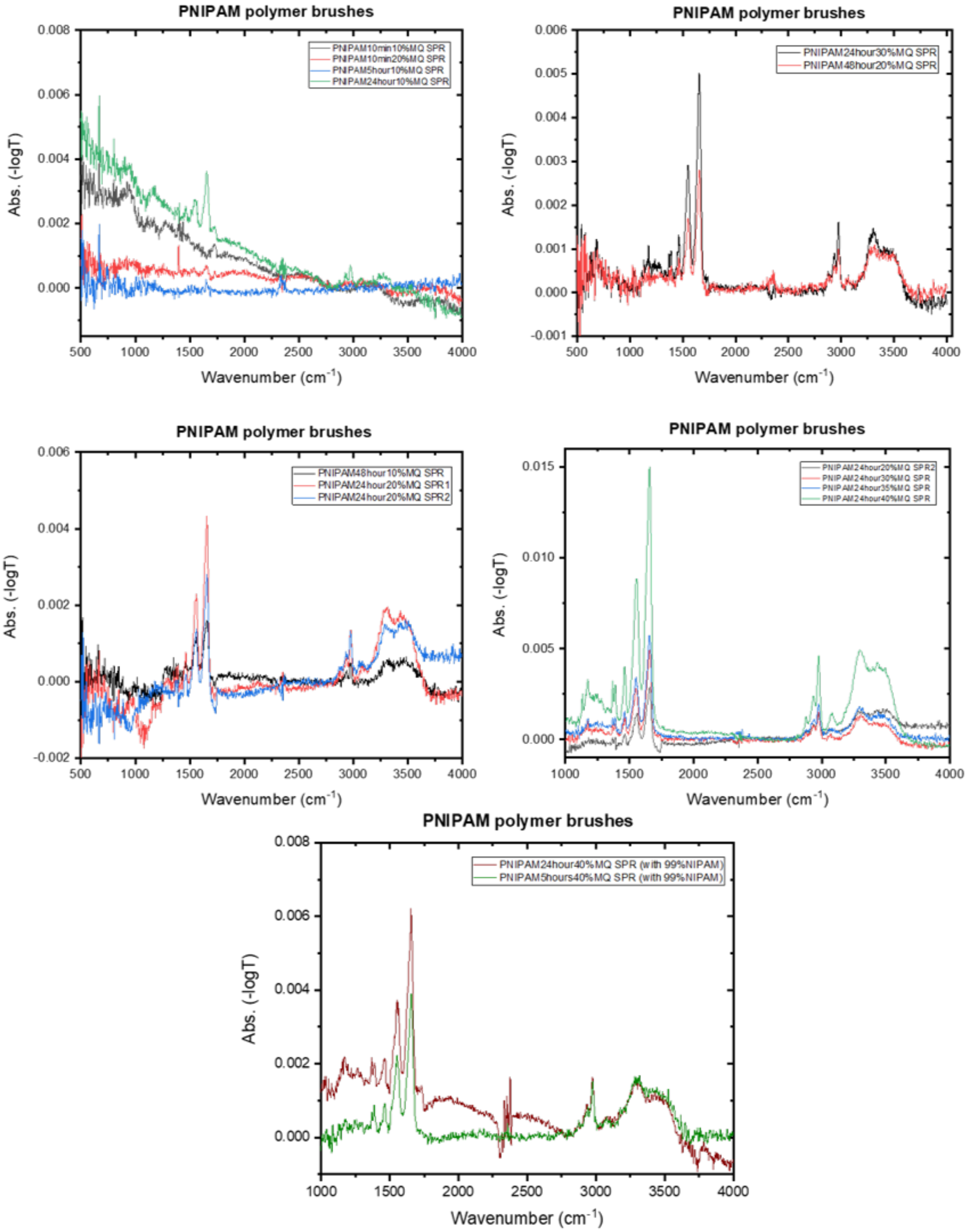

Figure B.2: FTIR ATR-RAS spectra of PNIPAM polymerizations longer than 1 hour at different MQ water *v*%. All spectra have been offset at 2700 cm^{-1}. In all polymerizations 97% NIPAM was utilized unless stated otherwise.

Appendix C

The first blueprint of the designed flow cell for optical microscopy in-situ experiments:

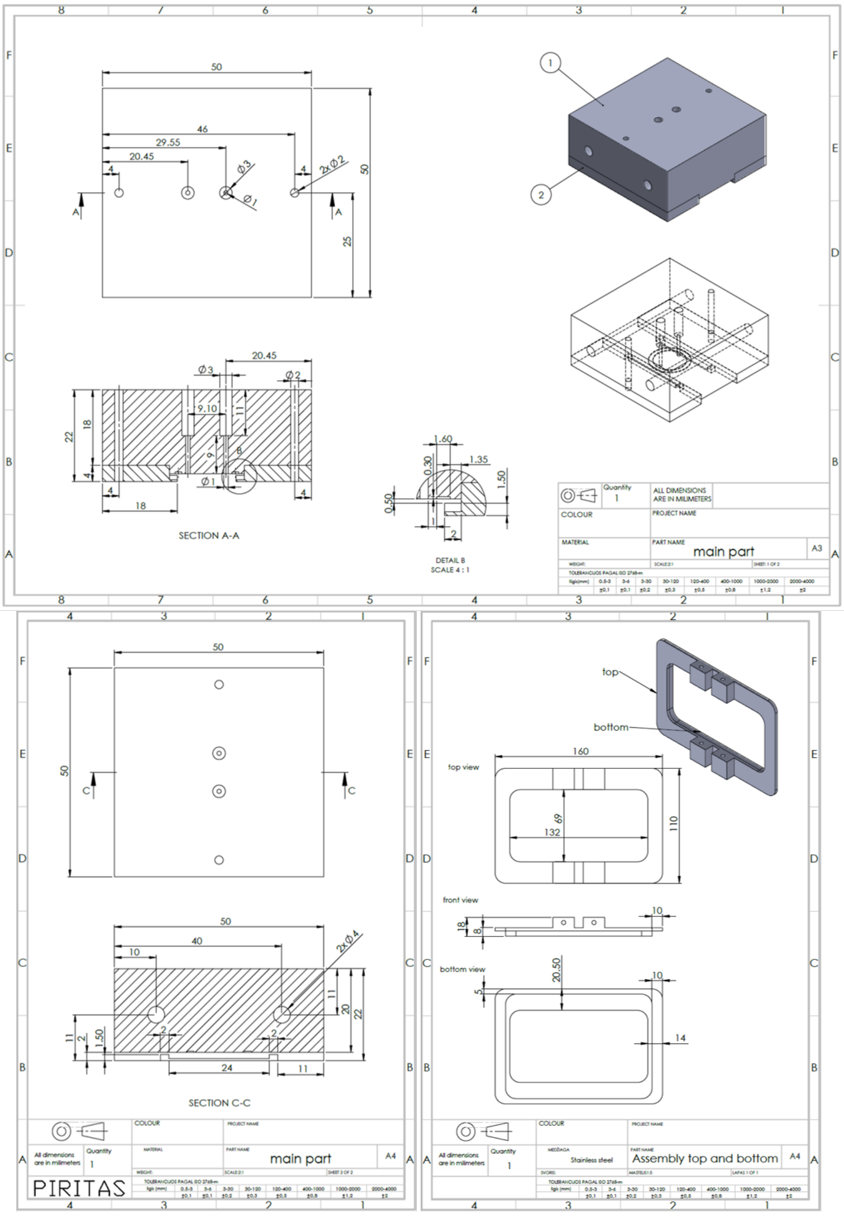

Figure C.1: First model of the flow cell designed for fluorescence microscopy and plasmonic shift experiments.

The first flow cell had to be re-designed because gave too high background noise from the light, which was reflected from the top wall of the flow cell perpendicular to the incident beam. Therefore, a second (up to date) blueprint of the flow cell for optical microscopy in-situ experiments was designed:

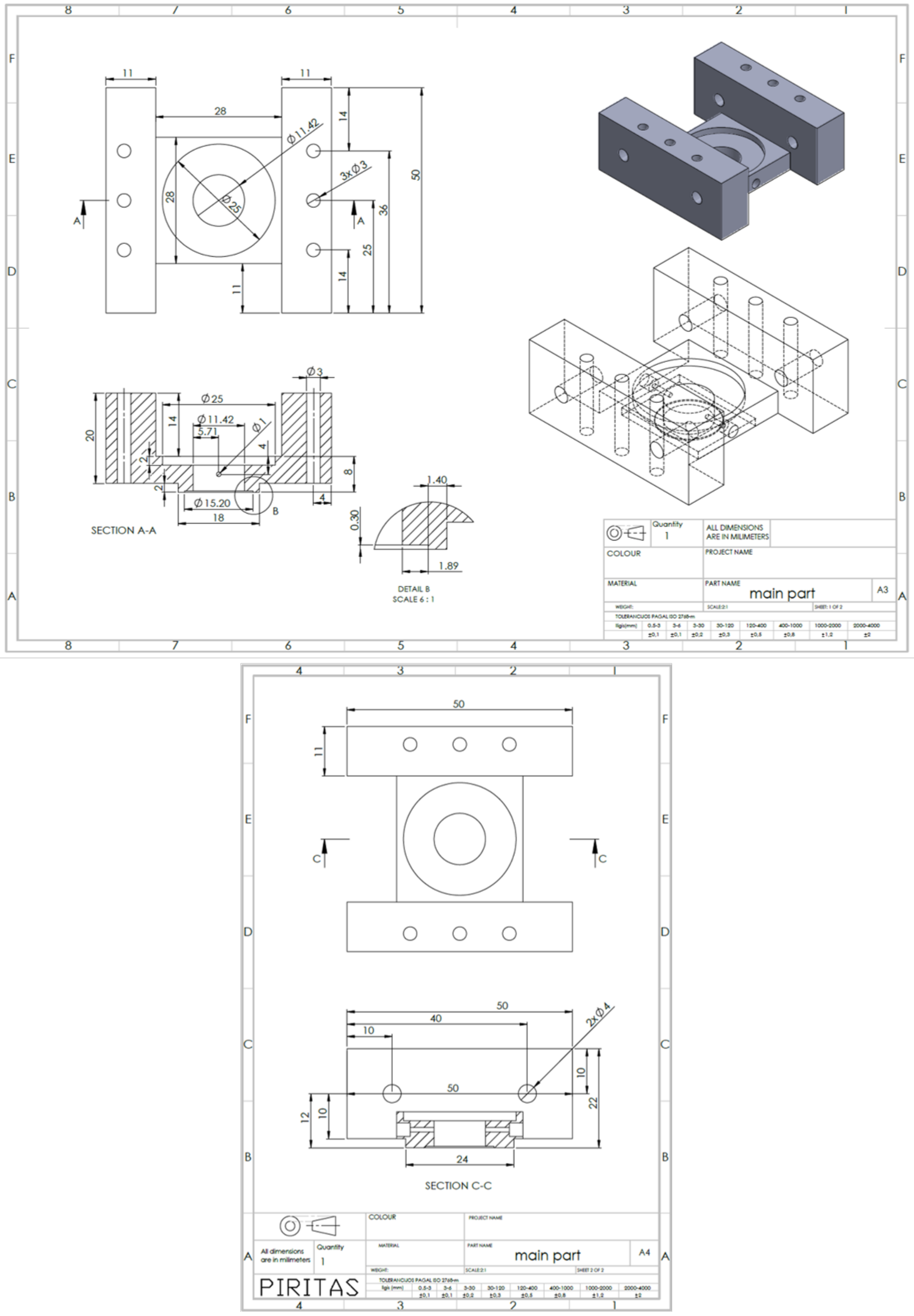

Figure C.2: Up-to date model of the flow cell designed for fluorescence microscopy and plasmonic shift experiments.

Appendix D

All determined plasmonic "peak" and "dip" shift numerical values can be seen in figures D.1 and D.2, respectively, for DTBU and TBU (thiol) initiated PNIPAM polymer brush polymerizations. Take note that in the system column, Micro1, Micro2 and Macro are separate optical setups in the lab. In the Micro2 system the light spot transmitting through the sample surface is smaller than in Micro1, Macro and Insplorion systems, thus plasmonic shifts are of relatively larger noise level.

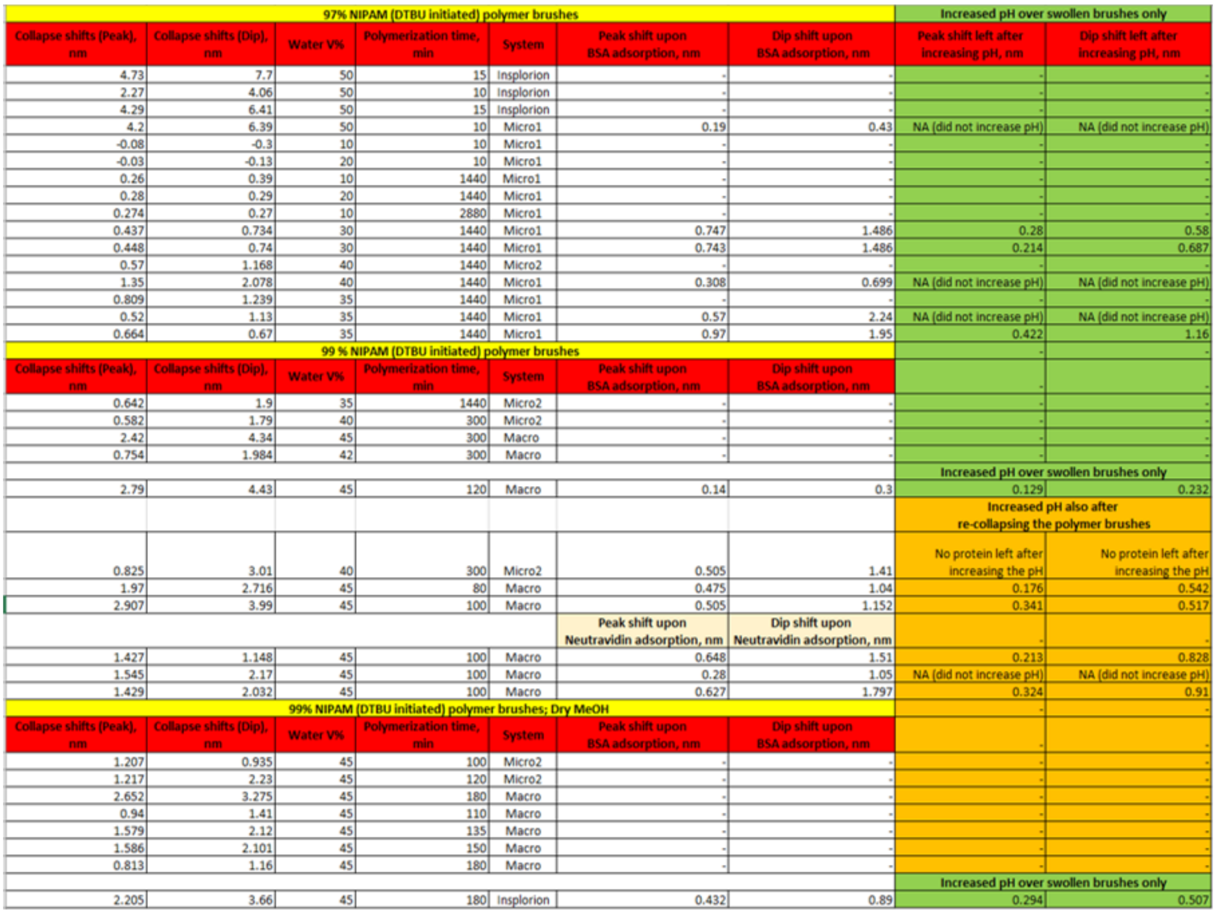

97% NIPAM (DTBU initiated) polymer brushes							Increased pH over swollen brushes only	
Collapse shifts (Peak), nm	Collapse shifts (Dip), nm	Water V%	Polymerization time, min	System	Peak shift upon BSA adsorption, nm	Dip shift upon BSA adsorption, nm	Peak shift left after increasing pH, nm	Dip shift left after increasing pH, nm
4.73	7.7	50	15	Insplorion	-	-	-	-
2.27	4.06	50	10	Insplorion	-	-	-	-
4.29	6.41	50	15	Insplorion	-	-	-	-
4.2	6.39	50	10	Micro1	0.19	0.43	NA (did not increase pH)	NA (did not increase pH)
-0.08	-0.3	10	10	Micro1	-	-	-	-
-0.03	-0.13	20	10	Micro1	-	-	-	-
0.26	0.39	10	1440	Micro1	-	-	-	-
0.28	0.29	20	1440	Micro1	-	-	-	-
0.274	0.27	10	2880	Micro1	-	-	-	-
0.437	0.734	30	1440	Micro1	0.747	1.486	0.28	0.58
0.448	0.74	30	1440	Micro1	0.743	1.486	0.214	0.687
0.57	1.168	40	1440	Micro2	-	-	-	-
1.35	2.078	40	1440	Micro1	0.308	0.699	NA (did not increase pH)	NA (did not increase pH)
0.809	1.239	35	1440	Micro1	-	-	-	-
0.52	1.13	35	1440	Micro1	0.57	2.24	NA (did not increase pH)	NA (did not increase pH)
0.664	0.67	35	1440	Micro1	0.97	1.95	0.422	1.16
99 % NIPAM (DTBU initiated) polymer brushes							-	-
Collapse shifts (Peak), nm	Collapse shifts (Dip), nm	Water V%	Polymerization time, min	System	Peak shift upon BSA adsorption, nm	Dip shift upon BSA adsorption, nm	-	-
0.642	1.9	35	1440	Micro2	-	-	-	-
0.582	1.79	40	300	Micro2	-	-	-	-
2.42	4.34	45	300	Macro	-	-	-	-
0.754	1.984	42	300	Macro	-	-	-	-
							Increased pH over swollen brushes only	
2.79	4.43	45	120	Macro	0.14	0.3	0.129	0.232
							Increased pH also after re-collapsing the polymer brushes	
							No protein left after increasing the pH	No protein left after increasing the pH
0.825	3.01	40	300	Micro2	0.505	1.41		
1.97	2.716	45	80	Macro	0.475	1.04	0.176	0.542
2.907	3.99	45	100	Macro	0.505	1.152	0.341	0.517
					Peak shift upon Neutravidin adsorption, nm	Dip shift upon Neutravidin adsorption, nm	-	-
1.427	1.148	45	100	Macro	0.648	1.51	0.213	0.828
1.545	2.17	45	100	Macro	0.28	1.05	NA (did not increase pH)	NA (did not increase pH)
1.429	2.032	45	100	Macro	0.627	1.797	0.324	0.91
99% NIPAM (DTBU initiated) polymer brushes; Dry MeOH							-	-
Collapse shifts (Peak), nm	Collapse shifts (Dip), nm	Water V%	Polymerization time, min	System	Peak shift upon BSA adsorption, nm	Dip shift upon BSA adsorption, nm	-	-
1.207	0.935	45	100	Micro2	-	-	-	-
1.217	2.23	45	120	Micro2	-	-	-	-
2.652	3.275	45	180	Macro	-	-	-	-
0.94	1.41	45	110	Macro	-	-	-	-
1.579	2.12	45	135	Macro	-	-	-	-
1.586	2.101	45	150	Macro	-	-	-	-
0.813	1.16	45	180	Macro	-	-	-	-
							Increased pH over swollen brushes only	
2.205	3.66	45	180	Insplorion	0.432	0.89	0.294	0.507

Figure D.1: All measured plasmonic shift experiments with DTBU initiated PNIPAM polymer brushes.

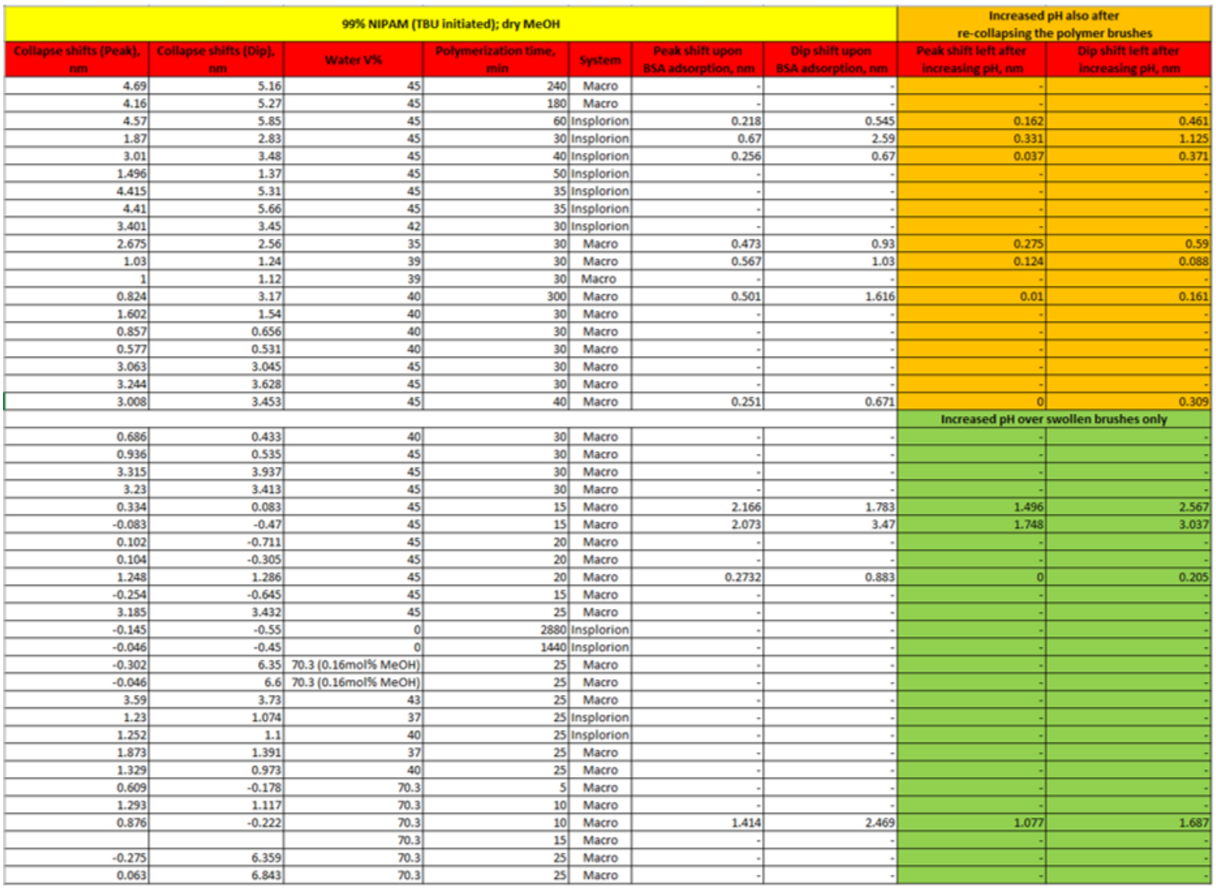

99% NIPAM (TBU initiated); dry MeOH							Increased pH also after re-collapsing the polymer brushes	
Collapse shifts (Peak), nm	Collapse shifts (Dip), nm	Water V%	Polymerization time, min	System	Peak shift upon BSA adsorption, nm	Dip shift upon BSA adsorption, nm	Peak shift left after increasing pH, nm	Dip shift left after increasing pH, nm
4.69	5.16	45	240	Macro	-	-	-	-
4.16	5.27	45	180	Macro	-	-	-	-
4.57	5.85	45	60	Insplorion	0.218	0.545	0.162	0.461
1.87	2.83	45	30	Insplorion	0.67	2.59	0.331	1.125
3.01	3.48	45	40	Insplorion	0.256	0.67	0.037	0.371
1.496	1.37	45	50	Insplorion	-	-	-	-
4.415	5.31	45	35	Insplorion	-	-	-	-
4.41	5.66	45	35	Insplorion	-	-	-	-
3.401	3.45	42	30	Insplorion	-	-	-	-
2.675	2.56	35	30	Macro	0.473	0.93	0.275	0.59
1.03	1.24	39	30	Macro	0.567	1.03	0.124	0.088
1	1.12	39	30	Macro	-	-	-	-
0.824	3.17	40	300	Macro	0.501	1.616	0.01	0.161
1.602	1.54	40	30	Macro	-	-	-	-
0.857	0.656	40	30	Macro	-	-	-	-
0.577	0.531	40	30	Macro	-	-	-	-
3.063	3.045	45	30	Macro	-	-	-	-
3.244	3.628	45	30	Macro	-	-	-	-
3.008	3.453	45	40	Macro	0.251	0.671	0	0.309
							Increased pH over swollen brushes only	
0.686	0.433	40	30	Macro	-	-	-	-
0.936	0.535	45	30	Macro	-	-	-	-
3.315	3.937	45	30	Macro	-	-	-	-
3.23	3.413	45	30	Macro	-	-	-	-
0.334	0.083	45	15	Macro	2.166	1.783	1.496	2.567
-0.083	-0.47	45	15	Macro	2.073	3.47	1.748	3.037
0.102	-0.711	45	20	Macro	-	-	-	-
0.104	-0.305	45	20	Macro	-	-	-	-
1.248	1.286	45	20	Macro	0.2732	0.883	0	0.205
-0.254	-0.645	45	15	Macro	-	-	-	-
3.185	3.432	45	25	Macro	-	-	-	-
-0.145	-0.55	0	2880	Insplorion	-	-	-	-
-0.046	-0.45	0	1440	Insplorion	-	-	-	-
-0.302	6.35	70.3 (0.16mol% MeOH)	25	Macro	-	-	-	-
-0.046	6.6	70.3 (0.16mol% MeOH)	25	Macro	-	-	-	-
3.59	3.73	43	25	Macro	-	-	-	-
1.23	1.074	37	25	Insplorion	-	-	-	-
1.252	1.1	40	25	Insplorion	-	-	-	-
1.873	1.391	37	25	Macro	-	-	-	-
1.329	0.973	40	25	Macro	-	-	-	-
0.609	-0.178	70.3	5	Macro	-	-	-	-
1.293	1.117	70.3	10	Macro	-	-	-	-
0.876	-0.222	70.3	10	Macro	1.414	2.469	1.077	1.687
		70.3	15	Macro	-	-	-	-
-0.275	6.359	70.3	25	Macro	-	-	-	-
0.063	6.843	70.3	25	Macro	-	-	-	-

Figure D.2: All measured plasmonic shift experiments with TBU initiated PNIPAM polymer brushes.

Bibliography

[1] P. Radivojac, L. M. Iakoucheva, C. J. Oldfield, Z. Obradovic, V. N. Uversky and A. K. Dunker. 'Intrinsic disorder and functional proteomics'. In: *Biophysical journal* 92.5 (2007), pp. 1439–1456.

[2] A. K. Dunker, C. J. Brown, J. D. Lawson, L. M. Iakoucheva and Z. Obradović. 'Intrinsic disorder and protein function'. In: *Biochemistry* 41.21 (2002), pp. 6573–6582.

[3] M. Brucale, B. Schuler and B. Samorì. 'Single-Molecule Studies of Intrinsically Disordered Proteins'. In: *Chemical Reviews* 114.6 (2014), pp. 3281–3317. DOI: `10.1021/cr400297g`.

[4] Q. Chen, R. Groote, H.r Schönherr and G. J. Vancso. 'Probing single enzyme kinetics in real-time'. In: *Chem. Soc. Rev.* 38 (9 2009), pp. 2671–2683. DOI: `10.1039/B903638E`.

[5] A. Küchler, M. Yoshimoto, S. Luginbühl, F. Mavelli and W. Peter. 'Enzymatic reactions in confined environments'. In: *Nature Nanotechnology* 11 (May 2016), pp. 409–420. DOI: `10.1038/nnano.2016.54`.

[6] N. G. Walter, Cheng-Yen Huang, J. A. Manzo and A. M. Sobhy. 'Do-it-yourself guide: how to use the modern single-molecule toolkit'. In: *Nature Methods* 5 (May 2008), pp. 475–489. DOI: `https://doi.org/10.1038/nmeth.1215`.

[7] O. Acuner, E. Saliha, Engin Hatice B., A. Gursoy and O. Keskin. 'Transient protein–protein interactions'. In: *Protein Engineering, Design and Selection* 24.9 (June 2011), pp. 635–648. DOI: `10.1093/protein/gzr025`.

[8] N. Cremades, S.I.A. Cohen, E. Deas, A. Abramov, A. Chen, A. Orte, M. Sandal, R. Clarke, P. Dunne, F. Aprile, C. Bertoncini, N. Wood, T. Knowles, C. Dobson and D. Klenerman. 'Direct Observation of the Interconversion of Normal and Toxic Forms of α -Synuclein'. In: *Cell* 149 (May 2012), pp. 1048–59. DOI: `10.1016/j.cell.2012.03.037`.

[9] P. Chene. 'The role of tetramerization in p53 function'. In: *Oncogene* 20 (June 2001), pp. 2611–7. DOI: `10.1038/sj.onc.1204373`.

[10] W. Meiye and S. K. Anup. 'Single-cell protein analysis'. In: *Current Opinion in Biotechnology* 23.1 (2012). Analytical biotechnology, pp. 83–88. DOI: `https://doi.org/10.1016/j.copbio.2011.11.023`.

[11] J. Nilsson, M. Evander, B. Hammarström and T. Laurell. 'Review of cell and particle trapping in microfluidic systems'. In: *Analytica Chimica Acta* 649.2 (2009), pp. 141–157. DOI: `https://doi.org/10.1016/j.aca.2009.07.017`.

[12] M. Krishnan, N. Mojarad, P. Kukura and V. Sandoghdar. 'Geometry-induced electrostatic trapping of nanometric objects in a fluid'. In: *Nature* 467 (2010), pp. 692–695. DOI: `https://doi.org/10.1038/nature09404`.

[13] B. Chatin, M. Mével, J. Devallière, L. Dallet, T. Haudebourg, P. Peuziat, T. Colombani, M. Berchel, O. Lambert, A. Edelman and B. Pitard. 'Liposome-based Formulation for Intracellular Delivery of Functional Proteins'. In: *Molecular Therapy - Nucleic Acids* 4 (2015), e244. DOI: `https://doi.org/10.1038/mtna.2015.17`.

[14] B. Malekian, K. Xiong, G. Emilsson, J. Andersson, C. Fager, E. Olsson, E.M. Larsson-Langhammer and A.B Dahlin. 'Fabrication and Characterization of Plasmonic Nanopores with Cavities in the Solid Support'. In: *Sensors* 17 (2017), p. 1444. doi: `https://doi.org/10.3390/s17061444`.

[15] G. Emilsson, K. Xiong, Y. Sakiyama, B. Malekian, V. Ahlberg Gagnér, R. L. Schoch, Roderick Y. H. Lim and A. B. Dahlin. 'Polymer brushes in solid-state nanopores form an impenetrable entropic barrier for proteins'. In: *Nanoscale* 10 (10 2018), pp. 4663–4669. doi: `10.1039/C7NR09432A`.

[16] K. Jain, R. Vedarajan, M. Watanabe, M. Ishikiriyama and N. Matsumi. 'Tunable LCST behavior of poly(N-isopropylacrylamide/ionic liquid) copolymers'. In: *Polym. Chem.* 6 (38 2015), pp. 6819–6825. doi: `10.1039/C5PY00998G`.

[17] P. Anzenbacher and M. Palacios. 'Polymer nanofibre junctions of attolitre volume serve as zeptomole-scale chemical reactors.' In: *Nature Chem* 1 (Mar. 2009), pp. 80–86. doi: `https://doi.org/10.1038/nchem.125`.

[18] R. Barbey, L. Lavanant, D. Paripovic, N. Schüwer, C. Sugnaux, S. Tugulu and Harm-Anton Klok. 'Polymer Brushes via Surface-Initiated Controlled Radical Polymerization: Synthesis, Characterization, Properties, and Applications'. In: *Chem. Rev.* 109 (Oct. 2009), pp. 5437–5527. doi: `10.1021/cr900045a`.

[19] G. Emilsson, R. L. Schoch, P. Oertle, K. Xiong, R.Y.H. Lim and A. B. Dahlin. 'Surface plasmon resonance methodology for monitoring polymerization kinetics and morphology changes of brushes—evaluated with poly(N-isopropylacrylamide)'. In: *Applied Surface Science* 396 (2017), pp. 384–392. doi: `10.1016/j.apsusc.2016.10.165`.

[20] R.W. Wood. 'On a remarkable case of uneven distribution of light in a diffraction grating spectrum'. In: *The London, Edinburgh, and Dublin Philosophical Magazine and Journal of Science* 4.21 (1902), pp. 396–402. doi: `10.1080/14786440209462857`.

[21] E. Kretschmann and H. Raether. 'Notizen: Radiative Decay of Non Radiative Surface Plasmons Excited by Light'. In: *Zeitschrift für Naturforschung A* 23.12 (1968), pp. 2135–2136. doi: `https://doi.org/10.1515/zna-1968-1247`.

[22] A. Otto. 'Excitation of nonradiative surface plasma waves in silver by the method of frustrated total reflection'. In: *Z. Physik* 216 (1968), pp. 398–410. doi: `https://doi.org/10.1007/BF01391532`.

[23] A.D. Boardman. *Electromagnetic Surface Modes*. John Wiley & Sons, 1982.

[24] H. Raether. *Surface plasmons on smooth and Rough Surfaces and on Gratings*. Vol. 111. Springer Tracts in Modern Physics. Springer, 1981.

[25] R. H. Ritchie. 'Plasma Losses by Fast Electrons in Thin Films'. In: *Phys. Rev.* 106 (5 June 1957), pp. 874–881. doi: `10.1103/PhysRev.106.874`.

[26] C. J. Powell and J. B. Swan. 'Effect of Oxidation on the Characteristic Loss Spectra of Aluminum and Magnesium'. In: *Phys. Rev.* 118 (3 May 1960), pp. 640–643. doi: `10.1103/PhysRev.118.640`.

[27] S.A. Maier. *Plasmonics. Fundamentals and Applications*. Springer, 2007.

[28] J. Homola. 'Surface Plasmon Resonance Sensors for Detection of Chemical and Biological Species'. In: *Chemical reviews* 108 (Mar. 2008), pp. 462–93. doi: `10.1021/cr068107d`.

[29] A.B. Dahlin. *Plasmonic Biosensors: An Integrated View of Refractometric Detection*. IOS press BV, 2012.

[30] L. S. Jung, C. T. Campbell, T. M. Chinowsky, M. N. Mar and S. S. Yee. 'Quantitative Interpretation of the Response of Surface Plasmon Resonance Sensors to Adsorbed Films'. In: *Langmuir* 14.19 (1998), pp. 5636–5648. doi: `10.1021/la971228b`.

[31] L. S. Jung, Charles T. Campbell, Timothy M. Chinowsky, Mimi N. Mar and Sinclair S. Yee. 'Quantitative Interpretation of the Response of Surface Plasmon Resonance Sensors to Adsorbed Films'. In: *Langmuir* 14.19 (1998), pp. 5636–5648. doi: `10.1021/la971228b`.

[32] R. L. Schoch and R. Y. H. Lim. 'Non-Interacting Molecules as Innate Structural Probes in Surface Plasmon Resonance'. In: *Langmuir* 29.12 (2013). PMID: 23437874, pp. 4068–4076. doi: `10.1021/la3049289`.

[33] J. Junesch, T. Sannomiya and A. B. Dahlin. 'Optical Properties of Nanohole Arrays in Metal–Dielectric Double Films Prepared by Mask-on-Metal Colloidal Lithography'. In: *ACS Nano* 6.11 (2012). PMID: 23098107, pp. 10405–10415. doi: `10.1021/nn304662e`.

[34] T. Sannomiya, O. Scholder, K. Jefimovs, C. Hafner and A. B. Dahlin. 'Investigation of plasmon resonances in metal films with nanohole arrays for biosensing applications'. In: *Small* 7.12 (2011), pp. 1653–1663. doi: `10.1002/smll.201002228`.

[35] A. B. Dahlin, N. J. Wittenberg, F. Höök and S. H. Oh. 'Promises and challenges of nanoplasmonic devices for refractometric biosensing'. In: *Nanophotonics* 2.2 (2013), pp. 83–101. doi: `10.1515/nanoph-2012-0026`.

[36] A. B. Dahlin, M. Mapar, K. Xiong, F. Mazzotta, F. Höök and T. Sannomiya. 'Plasmonic Nanopores in Metal-Insulator-Metal Films'. In: *Advanced Optical Materials* 2.6 (2014), pp. 556–564. doi: `10.1002/adom.201300510`.

[37] A. B. Dahlin. 'Sensing applications based on plasmonic nanopores: The hole story'. In: *Analyst* 140 (14 2015), pp. 4748–4759. doi: `10.1039/C4AN02258K`.

[38] H. Staudinger. 'Über Polymerisation'. In: *Berichte der deutschen chemischen Gesellschaft (A and B Series)* 53.6 (1920), pp. 1073–1085.

[39] E.D. Keoke and K.M. Porterfield. *Encyclopedia of American Indian Contributions to the World: 15,000 Years of Inventions and Innovations*. Facts on File library of American history. Facts On File, Incorporated, 2009.

[40] J. Tully. *The Devil's Milk: A Social History of Rubber*. New York University Press, 2011.

[41] M. Rubinstein and R.H. Colby. *Polymer Physics*. Oxford University Press, 2003.

[42] R. A. L. Jones. *Soft Condensed Matter*. Oxford University Press, June 2002.

[43] S. T. Milner. 'Polymer Brushes Published by : American Association for the Advancement of Science Stable URL : http://www.jstor.org/stable/2874899'. In: 251.4996 (1991), pp. 905–914.

[44] A. Halperin, M. Tirrell and T. P. Lodge. 'Macromolecules: Synthesis, Order and Advanced Properties'. In: *Macromolecules: Synthesis, Order and Advanced Properties* 100 (1992). doi: `10.1007/bfb0051632`.

[45] B. Zhao and W. J. Brittain. 'Polymer brushes: Surface-immobilized macromolecules'. In: *Progress in Polymer Science (Oxford)* 25.5 (2000), pp. 677–710. doi: `10.1016/S0079-6700(00)00012-5`.

[46] E.L Mackor and J.H van der Waals. 'The statistics of the adsorption of rod-shaped molecules in connection with the stability of certain colloidal dispersions'. In: *Journal of Colloid Science* 7.5 (1952), pp. 535–550. DOI: `https://doi.org/10.1016/0095-8522(52)90035-4`.

[47] T. B. McPherson, S. J. Lee and K. Park. 'Analysis of the Prevention of Protein Adsorption by Steric Repulsion Theory'. In: (1995), pp. 395–404. DOI: `10.1021/bk-1995-0602.ch028`.

[48] E. Raphaël and P. G. De Gennes. 'Rubber-rubber adhesion with connector molecules'. In: *Journal of Physical Chemistry* 96.10 (1992), pp. 4002–4007. DOI: `10.1021/j100189a018`.

[49] S. Alexander. 'Polymer adsorption on small spheres . A scaling approach'. In: *J. Phys.* 38.8 (1977), pp. 977–981. DOI: `10.1051/jphys:01977003808097700.jpa-00208665`.

[50] P.G. De Gennes. 'Scaling theory of polymer adsorption measured in porous structures or on polymers'. In: *J. Phys.* 37.12 (1976), pp. 1445–1452.

[51] R. Cantor. 'Nonionic diblock copolymers as surfactants between immiscible solvents'. In: *Macromolecules* 14.5 (1981), pp. 1186–1193. DOI: `10.1021/ma50006a010`.

[52] A. Halperin. 'Collapse of grafted chains in poor solvents'. In: *J. Phys.* 49.3 (1988), pp. 547–550.

[53] S. Minko. 'Responsive Polymer Brushes'. In: *Journal of Macromolecular Science, Part C: Polymer Reviews* 46.4 (2006), pp. 397–420. DOI: `10.1080/15583720600945402`.

[54] S. T. Milner, T. A. Witten and M. E. Cates. 'A parabolic density profile for grafted polymers'. In: *Europhys. letters* 5.5 (1988), pp. 413–418. DOI: `10.1209/0295-5075/5/5/006`.

[55] G. Conzatti, S. Cavalie, C. Combes, J. Torrisani, N. Carrere and A. Tourrette. 'PNIPAM grafted surfaces through ATRP and RAFT polymerization: Chemistry and bioadhesion'. In: *Colloids and Surfaces B: Biointerfaces* 151 (2017), pp. 143–155. DOI: `10.1016/j.colsurfb.2016.12.007`.

[56] G. Xie, A. Khabibullin, J. Pietrasik, J. Yan and K. Matyjaszewski. 'Polymer Brushes by Atom Transfer Radical Polymerization'. In: *Polymer and Biopolymer Brushes: For Materials Science and Biotechnology* i.1 (2017), pp. 29–95. DOI: `10.1002/9781119455042.ch2`.

[57] Justin O. Zoppe, Nariye Cavusoglu Ataman, Piotr Mocny, Jian Wang, John Moraes and Harm Anton Klok. 'Surface-Initiated Controlled Radical Polymerization: State-of-the-Art, Opportunities, and Challenges in Surface and Interface Engineering with Polymer Brushes'. In: *Chemical Reviews* 117.3 (2017), pp. 1105–1318. DOI: `10.1021/acs.chemrev.6b00314`.

[58] C. Xue, B. C. Choi, S. Choi, P. V. Braun and D. E. Leckband. 'Protein adsorption modes determine reversible cell attachment on poly(N-isopropyl acrylamide) brushes'. In: *Advanced Functional Materials* 22.11 (2012), pp. 2394–2401. DOI: `10.1002/adfm.201103056`.

[59] B. Lego, W. G. Skene and S. Giasson. 'Swelling study of responsive polyelectrolyte brushes grafted from mica substrates: Effect of pH, salt, and grafting density'. In: *Macromolecules* 43.9 (2010), pp. 4384–4393. DOI: `10.1021/ma902588j`.

[60] Y. Zou, J. N. Kizhakkedathu and D. E. Brooks. 'Surface modification of polyvinyl chloride sheets via growth of hydrophilic polymer brushes'. In: *Macromolecules* 42.9 (2009), pp. 3258–3268. DOI: `10.1021/ma8025699`.

[61] K. Binder, P.-G de Gennes, E.P. Giannelis, G.S. Grest, H. Hervet, R. Krishnamoorti, L. Leger, E. Manias, E. Raphael and S.-Q. Wang. *Polymers in confined environments*. Vol. 138. Springer, 1999.

[62] C. M. Hui, J. Pietrasik, M. Schmitt, C. Mahoney, J. Choi, M. R. Bockstaller and K. Matyjaszewski. 'Surface-initiated polymerization as an enabling tool for multifunctional (Nano-)engineered hybrid materials'. In: *Chemistry of Materials* 26.1 (2014), pp. 745–762. DOI: `10.1021/cm4023634`.

[63] F. J. Xu, K. G. Neoh and E. T. Kang. 'Bioactive surfaces and biomaterials via atom transfer radical polymerization'. In: *Progress in Polymer Science (Oxford)* 34.8 (2009), pp. 719–761. DOI: `10.1016/j.progpolymsci.2009.04.005`.

[64] C. J. Fristrup, K. Jankova and S. Hvilsted. 'Surface-initiated atom transfer radical polymerization - A technique to develop biofunctional coatings'. In: *Soft Matter* 5.23 (2009), pp. 4623–4634. DOI: `10.1039/b821815c`.

[65] S. Banerjee, T. K. Paira and T. K. Mandal. 'Surface confined atom transfer radical polymerization: Access to custom library of polymer-based hybrid materials for speciality applications'. In: *Polymer Chemistry* 5.14 (2014), pp. 4153–4167. DOI: `10.1039/c4py00007b`.

[66] M. Kato, M. Kamigaito, M. Sawamoto and T. Higashimura. 'Polymerization of Methyl Methacrylate with the Carbon Tetrachloride/Dichlorotris-(triphenylphosphine)ruthenium(II)/Methylaluminum Bis(2,6-di-tert-butylphenoxide) Initiating System: Possibility of Living Radical Polymerization'. In: *Macromolecules* 28.5 (1995), pp. 1721–1723. DOI: `10.1021/ma00109a056`.

[67] J. S. Wang and K. Matyjaszewski. 'Controlled/"Living" Radical Polymerization. Atom Transfer Radical Polymerization in the Presence of Transition-Metal Complexes'. In: *Journal of the American Chemical Society* 117.20 (1995), pp. 5614–5615. DOI: `10.1021/ja00125a035`.

[68] A. J. D. Magenau, N. C. Strandwitz, A. Gennaro and K. Matyjaszewski. 'Electrochemically Mediated Atom Transfer Radical Polymerization'. In: *Science* 332.6025 (2011), pp. 81–84. DOI: `10.1126/science.1202357`.

[69] Y. Kwak and K. Matyjaszewski. 'Photoirradiated atom transfer radical polymerization with an alkyl dithiocarbamate at ambient temperature'. In: *Macromolecules* 43.12 (2010), pp. 5180–5183. DOI: `10.1021/ma100850a`.

[70] Ke Min, Haifeng Gao and Krzysztof Matyjaszewski. 'Use of ascorbic acid as reducing agent for synthesis of well-defined polymers by ARGET ATRP'. In: *Macromolecules* 40.6 (2007), pp. 1789–1791. DOI: `10.1021/ma0702041`.

[71] G. Kickelbick, U. Reinöhl, T. S. Ertel, H. Bertagnolli and K. Matyjaszewski. *The Copper Catalyst in Atom Transfer Radical Polymerizations: Structural Observations*. ACS Symposium Series. 768, 2000. Chap. 15, pp. 211–222.

[72] K. Matyjaszewski. 'Atom Transfer Radical Polymerization (ATRP): Current Status and Future Perspectives'. In: *Macromolecules* 45.10 (2012), pp. 4015–4039. DOI: `10.1021/ma3001719`.

[73] K. Matyjaszewski, H. Dong, W. Jakubowski, J. Pietrasik and A. Kusumo. 'Grafting from Surfaces for "Everyone": ARGET ATRP in the Presence of Air'. In: *Langmuir* 23.8 (2007). PMID: 17371060, pp. 4528–4531. DOI: `10.1021/la063402e`.

[74] M. Horn and K. Matyjaszewski. 'Solvent Effects on the Activation Rate Constant in Atom Transfer Radical Polymerization'. In: *Macromolecules* 46.9 (2013), pp. 3350–3357. DOI: `10.1021/ma400565k`.

[75] F. Seeliger and K. Matyjaszewski. 'Temperature Effect on Activation Rate Constants in ATRP: New Mechanistic Insights into the Activation Process'. In: *Macromolecules* 42.16 (2009), pp. 6050–6055. DOI: `10.1021/ma9010507`.

[76] J. Morick, M. Buback and K. Matyjaszewski. 'Effect of Pressure on Activation–Deactivation Equilibrium Constants for ATRP of Methyl Methacrylate'. In: *Macromolecular Chemistry and Physics* 213.21 (2012), pp. 2287–2292. DOI: `10.1002/macp.201200411`.

[77] A. S. Hoffman. '"Intelligent" Polymers in Medicine and Biotechnology'. In: *Artificial Organs* 19.5 (1995), pp. 458–467. DOI: `10.1111/j.1525-1594.1995.tb02359.x`.

[78] P. Theato. 'Synthesis of well-defined polymeric activated esters'. In: *Journal of Polymer Science Part A: Polymer Chemistry* 46.20 (2008), pp. 6677–6687. DOI: `10.1002/pola.22994`.

[79] S. Dai, P. Ravi and Kam C. Tam. 'pH-Responsive polymers: synthesis, properties and applications'. In: *Soft Matter* 4 (3 2008), pp. 435–449. DOI: `10.1039/B714741D`.

[80] M. Heskins and J. E. Guillet. 'Solution Properties of Poly(N-isopropylacrylamide)'. In: *Journal of Macromolecular Science: Part A - Chemistry* 2.8 (1968), pp. 1441–1455. DOI: `10.1080/10601326808051910`.

[81] D. Davis, A. Hamilton, Yang. J., L.D. Cremar, D. Van Gough, S.L. Potisek, M.T. Ong, T.J. Martinez, S.R. White, J.S. Moore and N.R. Sottos. 'Force-induced activation of covalent bonds in mechanoresponsive polymeric materials'. In: *Nature* 459 (2009), pp. 68–72. DOI: `https://doi.org/10.1038/nature07970`.

[82] T. Tanaka, I. Nishio, S. Sun and S. UENO-NISHIO. 'Collapse of Gels in an Electric Field'. In: *Science* 218.4571 (1982), pp. 467–469. DOI: `10.1126/science.218.4571.467`.

[83] J. Thévenot, H. Oliveira, O. Sandre and S. Lecommandoux. 'Magnetic responsive polymer composite materials'. In: *Chem. Soc. Rev.* 42 (17 2013), pp. 7099–7116. DOI: `10.1039/C3CS60058K`.

[84] J. Hu and S. Liu. 'Responsive Polymers for Detection and Sensing Applications: Current Status and Future Developments'. In: *Macromolecules* 43.20 (2010), pp. 8315–8330. DOI: `10.1021/ma1005815`.

[85] A.K. Bajpai, K. S. Shukla, S. Bhanu and S. Kankane. 'Responsive polymers in controlled drug delivery'. In: *Progress in Polymer Science* 33.11 (2008), pp. 1088–1118. DOI: `https://doi.org/10.1016/j.progpolymsci.2008.07.005`.

[86] Marek W. U. 'Stratification, stimuli-responsiveness, self-healing, and signaling in polymer networks'. In: *Progress in Polymer Science* 34.8 (2009), pp. 679–687. DOI: `https://doi.org/10.1016/j.progpolymsci.2009.03.004`.

[87] D. V. Andreeva, D. Fix, H. Möhwald and D. G. Shchukin. 'Self-Healing Anticorrosion Coatings Based on pH-Sensitive Polyelectrolyte/Inhibitor Sandwichlike Nanostructures'. In: *Advanced Materials* 20.14 (2008), pp. 2789–2794. DOI: `10.1002/adma.200800705`.

[88] C. Alexander and K. M. Shakesheff. 'Responsive polymers at the biology/materials science interface'. In: *Advanced Materials* 18.24 (2006), pp. 3321–3328. DOI: `10.1002/adma.200502640`.

[89] E.H. Specht, Neuman A., Neher H.T. (to Rohm and Haas Co). *US2773063A*. Dec. 1956. URL: `https://patents.google.com/patent/US2773063A/en`.

[90] C. De Las Heras Alarcón, T. Farhan, V. L. Osborne, W. T.S. Huck and C. Alexander. 'Bioadhesion at micro-patterned stimuli-responsive polymer brushes'. In: *Journal of Materials Chemistry* 15.21 (2005), pp. 2089–2094. DOI: `10.1039/b419142k`.

[91] J. J.I. Ramos and S. E. Moya. 'Water content of hydrated polymer brushes measured by an in situ combination of a quartz crystal microbalance with dissipation monitoring and spectroscopic ellipsometry'. In: *Macromolecular Rapid Communications* 32.24 (2011), pp. 1972–1978. DOI: `10.1002/marc.201100455`.

[92] L. Linhui, Z. Yang, L. Bo and G. Changyou. 'Fabrication of thermoresponsive polymer gradients for study of cell adhesion and detachment'. In: *Langmuir* 24.23 (2008), pp. 13632–13639. DOI: `10.1021/la802556e`.

[93] K. Nagase, M. Yamato, H. Kanazawa and T. Okano. 'Poly(N-isopropylacrylamide)-based thermoresponsive surfaces provide new types of biomedical applications'. In: *Biomaterials* 153 (2018), pp. 27–48. DOI: `10.1016/j.biomaterials.2017.10.026`.

[94] W. Dai, C. Zheng, B. Zhao, K. Chen, P. Jia, J. Yang and J. Zhao. 'A negative correlation between water content and protein adsorption on polymer brushes'. In: *Journal of Materials Chemistry B* 7.13 (2019), pp. 2162–2168. DOI: `10.1039/c8tb03061h`.

[95] A. Halperin and M. Kröger. 'Theoretical considerations on mechanisms of harvesting cells cultured on thermoresponsive polymer brushes'. In: *Biomaterials* 33.20 (2012), pp. 4975–4987. DOI: `10.1016/j.biomaterials.2012.03.060`.

[96] A. Halperin, G. Fragneto, A. Schollier and M. Sferrazza. 'Primary versus Ternary Adsorption of Proteins onto PEG Brushes'. In: *Langmuir* 23.21 (2007). PMID: 17803323, pp. 10603–10617. DOI: `10.1021/la701007j`.

[97] A. Halperin and M. Kröger. 'Ternary Protein Adsorption onto Brushes: Strong versus Weak'. In: *Langmuir* 25.19 (2009). PMID: 19673469, pp. 11621–11634. DOI: `10.1021/la9008569`.

[98] F. Fang and I. Szleifer. 'Kinetics and Thermodynamics of Protein Adsorption: A Generalized Molecular Theoretical Approach'. In: *Biophysical Journal* 80.6 (2001), pp. 2568–2589. DOI: `https://doi.org/10.1016/S0006-3495(01)76228-5`.

[99] J. Fang and C. M. Knobler. 'Phase-Separated Two-Component Self-Assembled Organosilane Monolayers and Their Use in Selective Adsorption of a Protein'. In: *Langmuir* 12.5 (1996), pp. 1368–1374. DOI: `10.1021/la950751s`.

[100] N. Willem. 'Adsorption of proteins from solution at the solid-liquid interface'. In: *Advances in Colloid and Interface Science* 25 (1986), pp. 267–340. DOI: `https://doi.org/10.1016/0001-8686(86)80012-4`.

[101] Y. Yu, M. Cirelli, B. D. Kieviet, E. S. Kooij, G. J. Vancso and S. de Beer. 'Tunable friction by employment of co-non-solvency of PNIPAM brushes'. In: *Polymer* 102 (2016), pp. 372–378. DOI: `10.1016/j.polymer.2016.08.029`.

[102] N. Xue, X. P. Qiu, V. Aseyev and F. M. Winnik. 'Nonequilibrium Liquid-Liquid Phase Separation of Poly(N-isopropylacrylamide) in Water/Methanol Mixtures'. In: *Macromolecules* 50.11 (2017), pp. 4446–4453. DOI: `10.1021/acs.macromol.7b00407`.

[103] H. G. Schild, M. Muthukumar and D. A. Tirrell. 'Cononsolvency in Mixed Aqueous Solutions of Poly(N- isopropylacrylamide)'. In: *Macromolecules* 24.4 (1991), pp. 948–952. DOI: `10.1021/ma00004a022`.

[104] T. Fukai, N. Shinyashiki, S. Yagihara, R. Kita and F. Tanaka. 'Phase Behavior of Co-Nonsolvent Systems: Poly(N-isopropylacrylamide) in Mixed Solvents of Water and Methanol'. In: *Langmuir* 34.9 (2018), pp. 3003–3009. DOI: `10.1021/acs.langmuir.7b03815`.

[105] I. Bischofberger, D. C.E. Calzolari and V. Trappe. 'Co-nonsolvency of PNiPAM at the transition between solvation mechanisms'. In: *Soft Matter* 10.41 (2014), pp. 8288–8295. DOI: `10.1039/c4sm01345j`.

[106] F. Tanaka, T. Koga and F. M. Winnik. 'Temperature-Responsive Polymers in Mixed Solvents: Competitive Hydrogen Bonds Cause Cononsolvency'. In: *Phys. Rev. Lett.* 101 (2 July 2008), p. 028302. DOI: `10.1103/PhysRevLett.101.028302`.

[107] F. Tanaka, T. Koga, H. Kojima and F. M. Winnik. 'Temperature- and Tension-Induced Coil-Globule Transition of Poly(N-isopropylacrylamide) Chains in Water and Mixed Solvent of Water/Methanol'. In: *Macromolecules* 42.4 (2009), pp. 1321–1330. DOI: `10.1021/ma801982e`.

[108] F. Tanaka, T. Koga, I. Kaneda and F. M. Winnik. 'Hydration, phase separation and nonlinear rheology of temperature-sensitive water-soluble polymers'. In: *Journal of Physics: Condensed Matter* 23.28 (June 2011), p. 284105. DOI: `10.1088/0953-8984/23/28/284105`.

[109] J. Walter, J. Sehrt, J. Vrabec and H. Hasse. 'Molecular Dynamics and Experimental Study of Conformation Change of Poly(N-isopropylacrylamide) Hydrogels in Mixtures of Water and Methanol'. In: *The Journal of Physical Chemistry B* 116.17 (2012). PMID: 22432852, pp. 5251–5259. DOI: `10.1021/jp212357n`.

[110] A. Pomorska, K. Wolski, A. Puciul-Malinowska and S. Zapotoczny. 'Tailored conditions for controlled and fast growth of surface-grafted PNIPAM brushes'. In: *Polymer* 97 (2016), pp. 380–386. DOI: `10.1016/j.polymer.2016.05.048`.

[111] G. Zhang and C. Wu. 'Reentrant coil-to-globule-to-coil transition of a single linear homopolymer chain in a water/methanol mixture'. In: *Physical Review Letters* 86.5 (2001), pp. 822–825. DOI: `10.1103/PhysRevLett.86.822`.

[112] G. Zhang and C. Wu. 'The water/methanol complexation induced reentrant coil-to-globule-to-coil transition of individual homopolymer chains in extremely dilute solution'. In: *Journal of the American Chemical Society* 123.7 (2001), pp. 1376–1380. DOI: `10.1021/ja003889s`.

[113] K. Kyriakos, M. Philipp, L. Silvi, W. Lohstroh, W. Petry, P. Müller-Buschbaum and C. M. Papadakis. 'Solvent Dynamics in Solutions of PNIPAM in Water/Methanol Mixtures-A Quasi-Elastic Neutron Scattering Study'. In: *Journal of Physical Chemistry B* 120.20 (2016), pp. 4679–4688. DOI: `10.1021/acs.jpcb.6b01200`.

[114] Y. Yu, R. A. Lopez de la Cruz, B. D. Kieviet, H. Gojzewski, A. Pons, G. Julius Vancso and S. de Beer. 'Pick up, move and release of nanoparticles utilizing co-non-solvency of PNIPAM brushes'. In: *Nanoscale* 9 (4 2017), pp. 1670–1675. DOI: `10.1039/C6NR09245D`.

[115] S. Nian and L. Pu. 'Racemic Fluorescence Probe for Enantiomeric Excess Determination: Application of Cononsolvency of a Polymer in Sensing'. In: *The Journal of Organic Chemistry* 84.2 (2019), pp. 909–913. DOI: `10.1021/acs.joc.8b02793`.

[116] Kunli Xiong, Gustav Emilsson and Andreas B. Dahlin. 'Biosensing using plasmonic nanohole arrays with small, homogenous and tunable aperture diameters'. In: *Analyst* 141 (12 2016), pp. 3803–3810. DOI: `10.1039/C6AN00046K`.

[117] F. Mazzotta, T. W. Johnson, A. B Dahlin, J. Shaver, S. Oh and F. Höök. 'Influence of the evanescent field decay length on the sensitivity of plasmonic nanodisks and nanoholes'. In: *Acs Photonics* 2.2 (2015), pp. 256–262.

[118] J. Junesch, G. Emilsson, K. Xiong, S. Kumar, T. Sannomiya, H. Pace, J. Vörös, S. Oh, M. Bally and A. B. Dahlin. 'Location-specific nanoplasmonic sensing of biomolecular binding to lipid membranes with negative curvature'. In: *Nanoscale* 7 (37 2015), pp. 15080–15085. DOI: `10.1039/C5NR04208A`.

[119] M. D. Ward and D. A. Buttry. 'In Situ Interfacial Mass Detection with Piezoelectric Transducers'. In: *Science* 249.4972 (1990), pp. 1000–1007. DOI: `10.1126/science.249.4972.1000`.

[120] I. Reviakine, D. Johannsmann and R. P. Richter. 'Hearing what you cannot see and visualizing what you hear: Interpreting quartz crystal microbalance data from solvated interfaces'. In: *Analytical Chemistry* 83.23 (2011), pp. 8838–8848. DOI: `10.1021/ac201778h`.

[121] M. C. Dixon. 'Quartz crystal microbalance with dissipation monitoring: Enabling real-time characterization of biological materials and their interactions'. In: *Journal of Biomolecular Techniques* 19.3 (2008), pp. 151–158.

[122] D. Johannsmann, I. Reviakine and Ralf P. Richter. 'Dissipation in films of adsorbed nanospheres studied by quartz crystal microbalance (QCM)'. In: *Analytical Chemistry* 81.19 (2009), pp. 8167–8176. DOI: `10.1021/ac901381z`.

[123] Michael Rodahl and Bengt Kasemo. 'On the measurement of thin liquid overlayers with the quartz-crystal microbalance'. In: *Sensors and Actuators A: Physical* 54.1-3 (1996), pp. 448–456.

[124] J. Iruthayaraj, G. Olanya and Per M. Claesson. 'Viscoelastic properties of adsorbed bottle-brush polymer layers studied by quartz crystal microbalance -dissipation measurements'. In: *Journal of Physical Chemistry C* 112.38 (2008), pp. 15028–15036. DOI: `10.1021/jp804395f`.

[125] G. Liu, H. Cheng, L. Yan and G. Zhang. 'Study of the kinetics of the pancake-to-brush transition of poly(N-isopropylacrylamide) chains'. In: *Journal of Physical Chemistry B* 109.47 (2005), pp. 22603–22607. DOI: `10.1021/jp0538417`.

[126] D. Johannsmann. 'Viscoelastic analysis of organic thin films on quartz resonators'. In: *Macromolecular Chemistry and Physics* 200.3 (1999), pp. 501–516. DOI: `10.1002/(sici)1521-3935(19990301)200:3<501::aid-macp501>3.3.co;2-n`.

[127] Marina V Voinova, M Rodahl, M Jonson and B Kasemo. 'Viscoelastic acoustic response of layered polymer films at fluid-solid interfaces: continuum mechanics approach'. In: *Physica Scripta* 59.5 (1999), p. 391.

[128] *fluorophores*. `http://www.fluorophores.tugraz.at/substance/252`. Accessed: 2021-01-01.

[129] *Carl Zeiss Microscopy*. `https://www.micro-shop.zeiss.com/en/us/shop/filterAssistant/filtersets/489090-9100-000?pid=null&oid=object-0000-137&rFa=423058-8221-000&ff=1`. Accessed: 2020-12-07.

[130] D. A. Beattie, J. Addai-Mensah, A. Beaussart, G. V. Franks and Kai-Ying Yeap. 'In situ particle film ATR FTIR spectroscopy of poly (N-isopropyl acrylamide)(PNIPAM) adsorption onto talc'. In: *Physical Chemistry Chemical Physics* 16.45 (2014), pp. 25143–25151.

[131] J. C. Love, L. A. Estroff, J. K. Kriebel, R. G. Nuzzo and G. M. Whitesides. 'Self-assembled monolayers of thiolates on metals as a form of nanotechnology'. In: *Chemical reviews* 105.4 (2005), pp. 1103–1170.

[132] S. Gronert, A. E. Fagin, K. Okamoto, S. Mogali and L. M. Pratt. 'Leaving group effects in gas-phase substitutions and eliminations'. In: *Journal of the American Chemical Society* 126.40 (2004), pp. 12977–12983.

[133] S. Terrettaz, Wolf-Peter Ulrich, H. Vogel, Q. Hong, L. G. Dover and J. H. Lakey. 'Stable self-assembly of a protein engineering scaffold on gold surfaces'. In: *Protein Science* 11.8 (2002), pp. 1917–1925.

[134] E. Ostuni, L. Yan and G. M. Whitesides. 'The interaction of proteins and cells with self-assembled monolayers of alkanethiolates on gold and silver'. In: *Colloids and Surfaces B: Biointerfaces* 15.1 (1999), pp. 3–30.

[135] A. C. McUmber, T. W. Randolph and D. K. Schwartz. 'Electrostatic interactions influence protein adsorption (but not desorption) at the silica–aqueous interface'. In: *The journal of physical chemistry letters* 6.13 (2015), pp. 2583–2587.

[136] S. H. Brewer, W. R. Glomm, M. C. Johnson, M. K. Knag and S. Franzen. 'Probing BSA binding to citrate-coated gold nanoparticles and surfaces'. In: *Langmuir* 21.20 (2005), pp. 9303–9307.

[137] Q. Shi, Y. Zhou and Y. Sun. 'Influence of pH and ionic strength on the steric mass-action model parameters around the isoelectric point of protein'. In: *Biotechnology progress* 21.2 (2005), pp. 516–523.

[138] S. Fukuzaki, H. Urano and K. Nagata. 'Adsorption of bovine serum albumin onto metal oxide surfaces'. In: *Journal of fermentation and bioengineering* 81.2 (1996), pp. 163–167.

[139] L.R.S Barbosa, M. G. Ortore, F. Spinozzi, P. Mariani, S. Bernstorff and R. Itri. 'The importance of protein-protein interactions on the pH-induced conformational changes of bovine serum albumin: a small-angle X-ray scattering study'. In: *Biophysical journal* 98.1 (2010), pp. 147–157.

[140] A. Koichiro, S. Kenji, N. Shunji, K. Mitsuo and H. Koichi. 'Heat denaturation of bovine serum albumin in alkaline pH region'. In: *Biochimica et Biophysica Acta (BBA) - Protein Structure* 328.2 (1973), pp. 323–333. DOI: `https://doi.org/10.1016/0005-2795(73)90265-1`.

[141] G. Emilsson, R. L. Schoch, L. Feuz, F. Höök, R. Y. H. Lim and A. B. Dahlin. 'Strongly stretched protein resistant poly (ethylene glycol) brushes prepared by grafting-to'. In: *ACS applied materials & interfaces* 7.14 (2015), pp. 7505–7515.

[142] G. Emilsson, K. Xiong, Y. Sakiyama, B. Malekian, V. A. Gagnér, R. L. Schoch, R. Y. H. Lim and A. B. Dahlin. 'Polymer brushes in solid-state nanopores form an impenetrable entropic barrier for proteins'. In: *Nanoscale* 10.10 (2018), pp. 4663–4669.

[143] *NeutrAvidin Biotin-Binding Protein*. Web page. Accessed: 2020-10-29. URL: `https://assets.fishersci.com/TFS-Assets/LSG/manuals/MAN0011245_NeutrAvidin_Biotin_BindProtein_UG.pdf`.

[144] *Introduction to GPC*. Web page. Accessed: 2020-10-27. URL: `http://www.tainstruments.com/wp-content/uploads/GPC_GAP_APC_Workshop.pdf`.

[145] C. Xue, N. Yonet-Tanyeri, N. Brouette, M. Sferrazza, P. V. Braun and D. E. Leckband. 'Protein adsorption on poly (N-isopropylacrylamide) brushes: dependence on grafting density and chain collapse'. In: *Langmuir* 27.14 (2011), pp. 8810–8818.

[146] S. Choi, B. Choi, C. Xue and D. Leckband. 'Protein adsorption mechanisms determine the efficiency of thermally controlled cell adhesion on poly (N-isopropyl acrylamide) brushes'. In: *Biomacromolecules* 14.1 (2013), pp. 92–100.

[147] D. L. Huber, R. P. Manginell, M. A. Samara, B. Kim and B. C. Bunker. 'Programmed adsorption and release of proteins in a microfluidic device'. In: *Science* 301.5631 (2003), pp. 352–354.

[148] P. Kohli, K.K. Taylor, J.J. Harris and G.J. Blanchard. 'Assembly of covalently-coupled disulfide multilayers on gold'. In: *Journal of the American Chemical Society* 120.46 (1998), pp. 11962–11968.

[149] N. Nishida, M. Hara, H. Sasabe and W. Knoll. 'Formation and exchange processes of alkanethiol self-assembled monolayer on Au (111) studied by thermal desorption spectroscopy and scanning tunneling microscopy'. In: *Japanese journal of applied physics* 36.4R (1997), p. 2379.

[150] Y.S. Shon and T. R. Lee. 'Desorption and exchange of self-assembled monolayers (SAMs) on gold generated from chelating alkanedithiols'. In: *The Journal of Physical Chemistry B* 104.34 (2000), pp. 8192–8200.

[151] Y. Kwak, A.J.D. Magenau and K. Matyjaszewski. 'ARGET ATRP of methyl acrylate with inexpensive ligands and ppm concentrations of catalyst'. In: *Macromolecules* 44.4 (2011), pp. 811–819.

[152] S. Heider, E. Reimhult and C. Metzner. ‘Real-time analysis of protein and protein mixture interaction with lipid bilayers’. In: *Biochimica et Biophysica Acta (BBA) - Biomembranes* 1860.2 (2018), pp. 319–328. DOI: `https://doi.org/10.1016/j.bbamem.2017.10.024`.